University of Alberta

Patterning of Nanostructures by Block Copolymer Self-Assembly

by

Xiaojiang Zhang

A thesis submitted to the Faculty of Graduate Studies and Research
in partial fulfillment of the requirements for the degree of

Doctor of Philosophy

Department of Chemistry

© Xiaojiang Zhang
Spring 2012
Edmonton, Alberta

Permission is hereby granted to the University of Alberta Libraries to reproduce single copies of this thesis and to lend or sell such copies for private, scholarly or scientific research purposes only. Where the thesis is converted to, or otherwise made available in digital form, the University of Alberta will advise potential users of the thesis of these terms.

The author reserves all other publication and other rights in association with the copyright in the thesis and, except as herein before provided, neither the thesis nor any substantial portion thereof may be printed or otherwise reproduced in any material form whatsoever without the author's prior written permission.

Abstract

Fabrication of nanofeatures with precisely defined size and ordering is essential for a broad range of technologically important applications, including integrated circuit production. Self-organizing block copolymers are capable of patterning substrates with nanoscale precision. This thesis describes patterning of nanostructures by block copolymer self-assembly.

Rapid block copolymer self-assembly was realized with an innovative microwave-based method that used a scientific microwave reactor to anneal block copolymer films inside a sealed container in the presence of an appropriate solvent. Simple transformation of the as-annealed poly(styrene)-*block*-poly(2-vinylpyridine) (PS-*b*-P2VP) block copolymer films into metallic nanostructures led to better visualization of the self-assembled pattern in SEM. A study was made of a number of different parameters affecting the polymer assembly speed and the pattern defect density, such as solvent, annealing time, annealing temperature, and substrate resistivity. The approach was also applied to the commonly used poly(styrene)-*block*-poly(methyl methacrylate) block copolymers. Highly ordered linear patterns were obtained both on un-prepatterned substrates and e-beam lithography defined substrates in less than 3 minutes.

On adapting the microwave annealing technique to a conventional household microwave oven, highly ordered linear structures of self-assembled BCPs were obtained in 60 seconds. Using binary PS-*b*-P2VP block copolymer blends, linear feature spacing was readily controlled with nanometer scale precision. To show the high level of control over feature spacing, 12 to 19 metallic nanolines were

fabricated between 500-nm-wide topographic wall-like silica features on a silicon surfaces with an annealing time of less than 2 minutes. In addition, PS-*b*-P2VP/PS-*b*-P4VP binary blends were used to produce hybrid dot and line nanostructures. Although this study is still in an early stage, the concept of using self-assembled PS-*b*-P2VP/PS-*b*-P4VP mixture to template hybrid metallic nanostructures was successfully demonstrated.

PS-*b*-P4VP block copolymer films were employed as templates to pattern silicon surfaces with pseudo-hexagonal arrays of nanoscale etched pits, using a simple etching in HF(aq). The etched pit interiors were terminated by $Si\text{-}H_x$ while the top unetched silicon surface remains capped by the native silicon oxide. The potential utility of this interface was demonstrated by selective patterning of a nanostructured metal oxide and metal features within these pits on the silicon top face.

Acknowledgements

Looking back over the five years of my Ph.D. studies at the University of Alberta, I am deeply grateful to the wonderful people around me. It would not have been possible for me to complete my research and this thesis without the assistance and support of them.

First and foremost, I wish to express my heartfelt appreciation to my supervisor, Professor Jillian Buriak, for her continuous guidance, encouragement and invaluable suggestions in my Ph.D. pursuit. She has taught me how to be a good researcher, enlightened me through her wide knowledge of science, helped me during the tough times, and encouraged me with her enthusiasm for the research. I am deeply thankful for all her contributions of time, inspiration, and funding that made my Ph.D. experience substantial and productive.

I sincerely wish to acknowledge the many excellent collaborators here individually who have assisted in so many ways during my research: Nathanael Wu, Jeffrey Murphy, Dr. Kenneth Harris, Dr. Yinghong Qiao, Dr. Nicole Beckers, and Dr. Lina Xu. In particular, I would like to express my deepest gratitude to Dr. Harris, who has been a true mentor to me. For the rapid block copolymer self-assembly using microwaves, the studies discussed in this thesis would not have been possible without the collaboration: Nathanael, who is an expert engineer and my best friend, contributed the lithographically patterned substrates; Jeffrey, who has impressive computer skills, analyzed the data; in my later work on feature spacing control using binary block copolymer blends, Jeffrey also performed several control experiments; Ken helped me and guided all the way through this

research. In regards to the nanopatterning of titania on etched silicon substrates, Yinghong shared with me helpful tips that she picked up during her research on silicon etching. For the screening of bimetallic heterogeneous nanoparticle catalysts for arene hydrogenation, which is not mentioned in this dissertation, Nicole made significant contributions to the experiments. I also would like to thank Shihong Xu and Dr. Dimitre Karpuzov from Alberta Centre for Surface Engineering and Science (ACSES) for their help with surface analysis techniques and Daniel Salamon from the National Institute for Nanotechnology (NINT) for his help with the scanning electron microscope.

I owe a huge debt of gratitude to my colleagues in the Buriak group and many other kind friends. They made both my personal and professional time at the University of Alberta rich and enjoyable. Here I wish to acknowledge the friendship and support from the past and current group members that I have had the pleasure and honor to work with: Dr. Usama Al-Atar, Dr. Masato Aizawa, Jeremy Bau, Dr. Nicole Beckers, Jennifer Bruce, Dr. Steven Chai, Dr. Qun Chen, Dr. Brian Daly, Torsten Dörschel, Dr. Anastasia Elias, Yuan Gao, Tate Hauger, Dr. Lawrence Huck, Dr. Yunhui Li, Dr. Weiwei Li, Dr. Sean McClure, Dr. Hidenori Mizuno, Jeffrey Murphy, Dr. Sayed Nagy, Dr. Yinghong Qiao, Dr. David Rider, Anne Slaney, Dr. Tonggang Jiu, Dr. Dong Wang, Brian Worfolk, Dr.Vincent Wright, Nathaniel Wu, Xiao Xing, and Dr. Lina Xu. I am grateful for time spent with my buddies at the University of Alberta: Jing Peng, Tongda Shao, Pinxuan Li, Lihong Wang, Xin Zhang, Liang Yu, Dr. Jianbo Gao, Jie Ru, Xiongyao Wang, and Nathan Fitzpatrick.

For my research and this dissertation I want to thank my supervisory committee members: Professor Steven Bergens, Professor Alex Brown, Professor Al Meldrum, and Professor Jonathan Veinot for their time, interest, and insightful comments. I would also wish to thank Professor Viola Birss of my oral defence committee from University of Calgary for her time and thoughtful questions.

For this dissertation I would like to thank Michael Carpenter, Jeffrey Murphy, Nathanael Wu, Jennifer Bruce, Jeremy Bau, and Dr. Lawrence Huck for helpful revisions, discussions and suggestions.

Finally, I wish to thank my family and my wife Ting for their endless love, patience and encouragement and faithful support in all my pursuits.

Xiaojiang Zhang

University of Alberta

September 2011

Table of Contents

Abstract

Acknowledgement

Table of Contents

List of Figures

List of Tables

List of Abbreviations

Chapter 1 A Brief Introduction to Block Copolymer Lithography…..……….*1*

1.1 Background………………………...…………………………………….…....*2*

1.2 Conventional Lithography Techniques………..………………………….…...*3*

History of Printing……………………………….……………….…...…….*3*

Photolithography…………...……………………………………….…....*5*

Electron Beam Lithography (EBL)…………………….…...…….…………….*8*

Nanoimprint Lithography (NIL) & Self-Aligned Imprint Lithography (SAIL)….…………………………………………………...…………...…*11*

1.3 BCP Nanolithography…………...…………………………...……….………*13*

Self-Assembled BCP Microdomains with Low Defect Density and High Alignment ……………………………………………...……………….*15*

1.4 Applications of BCP Self-Assembly…………………...……..………………...*25*

1.5 Scope of the Thesis………...…………………………………….…………...32

1.6 References…...……………………………………....……………………..*34*

Chapter 2 Fast BCP Self-Assembly Achieved by Solvent-Assisted Microwave Annealing……………………………………………*40*

2.1 Introduction…………………………………….…………………………*41*

Blcok Copolymers (BCPs).………..…………………..…………….…...…….*41*

BCP Annealing Techniques……………..……………………………….……..*42*

BCP Self-Assembly Speed………………………….……………………..*44*

2.2 Results and Discussions…………………..…………….………………………*45*

BCP Thin Films.…….……………………………….……………………*45*

Microwave Annealing.…………..………………………..………………..*47*

Fabrication of Metallic Nanoparticles on Silicon Substrates..………………..*51*

Rapid Self-Assembly in Microwaves……..……………….…………..…..*52*

Thermal Annealing.…………………………………………..……...*57*

Effects of Time on Microwave Annealing………………..…………………*58*

Effects of Temperature and Solvent on Microwave Annealing……..………*58*

Microwave Annealing vs. Pure Thermal Annealing…….…………………...*64*

Substrate Resistivity………………………………………………………..*65*

Compatibility with Topographical Graphoepitaxy…………………..............*68*

2.3 Conclusions……………………………………..………………………..*75*

2.4 Experimental Section……….………………………………………………...*76*

2.5 References……………………………………………………………….....81

Chapter 3 Control of Spacing of Metal and Hybrid Nanostructures Templated by Rapidly Self-assembled Binary BCP Blends Using Microwave Heating……………..………………………………..*85*

3.1 Introduction……………………………………………………………..*85*

Control of Spacing Using BCP Blends…...…………..................................*86*

Novel Morphologies Obtained Using BCP Blends…………………..............*89*

3.2 Results and Discussion.…………………………………………….............*91*

Choosing Appropriate Silicon Substrate……………………………………..*91*

Annealing in a Conventional Microwave Oven…………….……………..*93*

Binary BCP Blends: PS-*b*-P2VP / PS-*b*-P2VP……...………………………*96*

Graphoepitaxially Directed Self-Assembly of Binary BCP Blends………...102

Annealing in Conventional Microwave Oven: Time Evolution of BCP Self-Assembly……………………………………………………………………104

Binary BCP Blends: PS-*b*-P2VP / PS-*b*-P4VP….…………………………..…106

3.3 Conclusions.……………………………………….……………………...112

3.4 Experimental Section……………………………………………………..113

3.5 References…………………………………………………………………...117

Chapter 4 Selective Fabrication of Ordered Titania Nanostructures on Etched Silicon Surfaces Using BCP Thin Films as Templates..*120*

4.1 Introduction………………………………….……………………………120

Nanopatterning of Titania Using BCP Thin Films as Templates.…………..121

4.2 Results and Discussion……………………………………………………124

Silicon Etching Using BCPs as Soft Masks…………………………........124

Formation of Titania Nanobowls………………………………...................126

The Role of H_2O_2 Oxidation Step in the Deposition of Titania……............133

Formation of Continuous Titania Films……………………………….……135

Release of the Titania Nanobowls………………………………………..138

Gold Deposition on Titania Nanobowls…………………………………….141

4.3 Conclusions…………………………………………………………………144

4.4 Experimental Section……….………………………………………….………145

4.5 References…………………………………………………………….………150

Chapter 5 Conclusion and Outlook…………………………….……………..*156*

5.1 Chapter Summaries.…………………………………………………………156

5.2 Proposed Research Directions…………………………………….………159

Solvothermal Annealing of BCPs…………………………………………...159

Localized BCP Self-Assembly in Microwaves…………………………...161

NIL with BCP Self-Assembly for Mass Production…..................................*165*

5.3. References……………………………………………….………………………*173*

List of Figures

Figure 1.1 Basic schematic illustration of "pitch" and "half-pitch".

Figure 1.2 Basic schematic illustration of how photolithography works. Patterns are created on a wafer by using a light source to expose photoresist-coated surfaces through a photo mask.

Figure 1.3 (a) Picture of the probe array used in the parallel scanning near-field photolithography. (b) and (c) Schematic outline of the silicon cantilever probe. (d) Schematic outline of photodeprotection reaction of NPPOC-APTES. (e) AFM height image of a zigzag pattern created by parallel scanning near-field photolithography.

Figure 1.4 E-beam lithography can be used to write either positive or negative patterns in a resist. When positive resist is used, developer solution removes exposed material, leaving positive patterns on the surface; when negative resist is used, developer solution removes unexposed material, leaving negative patterns on the surface.

Figure 1.5 (a) Schematic outline of the direct pattering of polymer SAMs using EBL. (b) and (c) AFM height images of EBL patterned PIBMA and PNPMA SAMs, respectively.

Figure 1.6 Schematic outline of the NIL process.

Figure 1.7 SEM images of Pt nanostructures templated by self-assembled BCPs. (a) and (b), hexagonal arrays. (c) and (d), linear arrays.

Figure 1.8 Directed self-assembly of BCPs on topological feature-defined surface and lithographically predefined chemically patterned surface.

Figure 1.9 (a) Schematic representation of the packing of spheres within a V-shaped groove. (b) SEM image of V grooves etched in a Si (100) substrate. (c) SEM image of PS-PFS films in V grooves after annealing and etching.

Figure 1.10 (a) Schematic representation of BCP lithography process using a chemically pre-patterned surface to direct the assembly of the BCP domains in registry with the underlying surface pattern. (b) SEM images of PS-*b*-PMMA domains annealed on chemical surface patterns.

Figure 1.11 (a) Schematic representation of BCP lithography procedure to align BCP domains in an ultra-large area: (i) Conventional I-line lithography was used to pattern graphoepitaxial features on a neutral polymer-brush-coated Si substrate. (ii) BCP self-assembly was confined within the graphoepitaxial features. (iii) Self-assembled BCP patterns were used to selectively etch the underlying polymer brush layer. (iv) Residual photoresist and polymer were removed to expose the chemical nanopattern. (v) BCP self-assembly in an ultra-large area on chemically patterned surface. (b) Lamellar forming BCPs self-assembled within photoresist trenches. (inset image: graphoepitaxial pattern prepared by I-line photolithography). (c) Cylinder forming PS-*b*-PMMA BCP self-assembled on chemically patterned substrates. (d) Lamellar forming PS-*b*-PMMA BCP self-assembled on chemically patterned substrates.

Figure 1.12 (a)-(c), SFM phase images of highly ordered PEO-*b*-PMMA-*b*-PS triblock copolymer thin films that were solvent-annealed for 12 h in a benzene vapor. (d)-(f) are triangulation images corresponding to SFM images shown in (a)-(c), respectively.

Figure 1.13 TEM image of gold nanoparticles patterned by PS-*b*-P4VP BCP.

Figure 1.14 (a) BCP self-assembly and plasma etching were used to pattern metallic nanowires on a substrate. (b) SEM image of the oxidized PDMS pattern after self-assembly and reactive ion etching. (c) SEM image of the oxidized PDMS pattern after metal deposition. (d) SEM image of metal surface after plasma etching. (e) SEM image of metallic nanowires.

Figure 1.15 (a) Schematic representation of deprinting process on a silicon substrate with a monolayer of gold salt loaded BCP micelles using a PS stamp. Different patterns can be obtained with the same PS stamp at different temperature. (b) SEM images of hexagonally arranged Au nanoparticle patterns on silicon substrate.

Figure 1.16 (a) Schematic presentation of the preparation of square packed perpendicular BCP cylinders using solvent annealing. (b) Schematic and SEM images of graphoepitaxy confined, highly ordered square arrays.

Figure 1.17 (a) Geometries required for fabricating most integrated circuits. (defined by the Semiconductor Industry Association's member companies) (b) SEM images of the directed self-assembled polymer structures.

Figure 2.1 (a) Generalized structure of an AB diblock copolymer. (b) Chemical structures of the PS-*b*-P2VP and PS-*b*-PMMA block copolymers used in this study and SEM images of the nanostructures generated using self-assembled PS-*b*-P2VP and PS-*b*-PMMA block copolymers as the platform.

Figure 2.2 Pictures of conventional annealing methods. (a) Solvent annealing in desiccators. (b) Thermal annealing in a vacuum oven.

Figure 2.3 (a) Outline of BCP directed self-assembly using chemical pre-patterning. (b) SEM images of the directed assembly of PS-*b*-PMMA on chemically patterned surfaces at various annealing times and temperatures.

Figure 2.4 Picture of block copolymer thin film-coated silicon substrates.

Figure 2.5 Outline for block copolymer thin film preparation.

Figure 2.6 (a) Picture of the microwave annealing reaction tube. (b) Schematics of experimental approaches of microwave annealing with PS-*b*-P2VP and PS-*b*-PMMA BCPs.

Figure 2.7 SEM images showing nanostructures observed for unannealed BCPs.

Figure 2.8 Picture of Biotage Initiator 2.5 microwave system.

Figure 2.9 Schematic representation of metal deposition process.

Figure 2.10 Platinum and BCP patterns prepared by microwave annealing. (a), (b), and (e) SEM images of Pt nanolines templated from 60 s microwave anneal using PS-*b*-P2VP (23.6k-*b*-10.4k). In (a), the substrate was unpatterned, and in (b), the substrate was flat silicon with EBL fabricated silica topological features. (c) and (d) SEM images of 180 s microwave annealed PS-*b*-PMMA (45k-*b*-20k) on (c) unpatterned silicon substrate and (d) flat silicon with two parallel silica lines.

Figure 2.11 (a) Picture of experimental setup to mimic the solvent-assisted microwave annealing. (b) Picture of BCP sample before annealing. (c) Picture of BCP sample after annealing.

Figure 2.12 Influence of annealing time on BCP organization. (a)-(d) SEM images of Pt nanofeatures prepared from microwave annealed PS-*b*-P2VP BCPs. (e) SEM images of microwave annealed PS-*b*-PMMA (45k-*b*-20k). The first panel (0 s) in each series shows the BCP samples prior to annealing.

Figure 2.13 Studies to determine the effect of solvent and temperature. (a)-(c) SEM images of Pt nanostructures templated by microwave annealed PS-*b*-P2VP (23.6k-*b*-10.4k). (d) Picture of the Teflon isolation chamber used in the solvent isolation experiments. (e) Plots of defect density versus annealing temperature for several BCPs, solvents and annealing conditions.

Figure 2.14 Studies to determine the effect of solvent and temperature. (a) and (b), SEM images of Pt nanostructures templated by THF-assisted microwave annealed PS-*b*-P2VP (32.5k-*b*-12k). (c) and (d), SEM images of THF-assisted microwave annealed PS-*b*-PMMA (45k-*b*-20k).

Figure 2.15 SEM images of Pt nanostructures templated by 180 s microwave annealed PS-*b*-P2VP (23.6k-*b*-10.4k) using different solvents: (a) DCB, (b) DMF, (c) water, and (d) ethanol.

Figure 2.16 (a) And (b) SEM images of Pt nanostructures templated by thermally annealed PS-*b*-P2VP (32.5k-*b*-12k) and (44k-*b*-18.5k) BCPs, respectively.

Figure 2.17 Influence of substrate resistivity over BCP organization. (a) and (b) SEM images of Pt nanostructures templated from PS-*b*-P2VP (32.5k-*b*-12.0k) thin films that were microwave annealed at 130 ℃ for 180 s on Si(100) substrates of varying resistivity in the presence of (a) THF and (b) toluene. (c) Plots of the evolution of defect density as the substrate resistivity is varied.

Figure 2.18 Outline of fast BCP self-assembly along graphoepitaxial features using microwave annealing.

Figure 2.19 SEM images of Pt nanostructures templated from microwave annealed BCPs on e-beam patterned silicon substrates. The microwave annealing was performed at 130 ℃ for 60 s.

Figure 2.20 SEM images of Pt nanostructures templated from microwave-annealed BCPs at different temperatures. The microwave annealing was performed at (a) 80 ℃ and (b) 130 ℃ for 60 s.

Figure 2.21 Fast ordering of BCPs on surfaces with graphoexpitaxial features. (a) SEM images of microwave annealed PS-*b*-PMMA (45k-*b*-20k) structures aligned along silica walls. The BCP samples were microwave annealed for 180 s in the presence of THF. (b) SEM images of Pt nanostructures templated from microwave annealed PS-*b*-P2VP (32.5k-*b*-12.0k) BCPs. The BCP samples were microwave annealed for 60 s in the presence of THF. (c) Plots of the evolution of defect density as annealing temperature was varied on surfaces with graphoepitaxial features.

Figure 2.22 SEM of silica nanostructures templated by microwave annealed PS-*b*-PDMS. The annealing was preformed at 140 ℃ for 180 s.

Figure 2.23 Component structures for all defects observed in the experiments.

Figure 3.1 SEM images of PS-*b*-PMMA (46k-*b*-21k)/PS (21k)/PMMA (21k) blends. The volume fraction of homopolymer in the blends is shown in the upper left corner of each SEM image.

Figure 3.2 Typical morphologies of A-B diblock copolymer.

Figure 3.3 TEM images of binary PS-*b*-PMMA blend thin films annealed in acetone vapor.

Figure 3.4 Images of wax samples on silicon substrates. (a) and (b): before microwave irradiation; (c), (d), and (e): after microwave irradiation. It can be seen that nearly all of the wax on substrate 1 is gone, due to a combination of vaporization and run-off; sample 2 was completely melted; both samples 3 and the wax sample without a silicon substrate were unchanged. Numbers correspond to those in the experiment.

Figure 3.5 (a) Picture of sealed Teflon annealing chamber inside a household conventional microwave oven. (b) Picture of the disassembled Teflon annealing chamber. (c) Schematic outline of fabrication of ordered metallic nanowires using microwave annealing.

Figure 3.6 BCP annealing in a conventional microwave oven. (1) Adding solvent to the container. (2) Adding sample to the container. (3) Sealing the container. (4) Microwave annealing. (5) Sample removal.

Figure 3.7 SEM image of Pt nanopatterns templated from a microwave annealed binary PS-*b*-P2VP BCP blend BC 7:3.

Figure 3.8 Outline for spacing control using binary PS-*b*-P2VP BCP blends.

Figure 3.9 SEM images of Pt nanopatterns templated from PS-*b*-P2VP/PS-*b*-P2VP binary blends that were microwave annealed for 60 s and feature spacing and defect density as functions of the mass fraction of X in X/Y blend.

Figure 3.10 SEM images of Pt nanopatterns templated from binary blends BF and AB that were microwave annealed for 60 s.

Figure 3.11 Linear feature spacing control along graphoepitaxially created silica wall-like strictures spaced 500 nm apart. SEM images of Pt nanostructures with six different spacings, templated by two neat BCPs and four blends: (a) BCP B, (b) blend BC 7:3, (c) BPC C, (d) blend BC 4:6, (e) blend AD 5:5, and (f) blend AD 4:6. In all cases, the microwave annealing time was 80 seconds.

Figure 3.12 Influence of annealing time on the BCP pattern organization. (a) - (d) SEM images of Pt nanostructures templated by microwave annealed neat BCP and BCP blends. (e) Plots of the evolution of defect density for BCPs and binary BCP blends microwave annealed for 0 second to 120 seconds. (f) SEM images of Pt nanostructures templated by thermally annealed blend BC 5:5.

Figure 3.13 Outline for using binary PS-*b*-P2VP / PS-*b*-P4VP blends to produce hybrid nanostructures.

Figure 3.14 SEM image of Pt nanostructures templated by 24 hours solvent annealed blend V.

Figure 3.15 SEM images of Pt nanostructures templated by 60 s microwave annealing. (a) Blend III and (b) blend IV.

Figure 3.16 SEM images of Pt nanostructures templated by blend VI. (a) As-cast, (b) 90 seconds microwave annealed at 60 % power, (c) 120 seconds microwave annealed at 60 % power, and (d) 60 seconds microwave annealed at maximum power.

Figure 3.17 SEM images of Pt nanostructures templated by blend I. (a) Thermally annealed for 36 hours; (b) microwave annealed for 60 seconds.

Figure 3.18 Damaged Teflon container.

Figure 4.1 Outline of the preparation of titania nanostructures using PS-*b*-P4VP BCP templates.

Figure 4.2 (a) Plan view TEM image of a hexagonal mesostructured titania film tempalted by BCPs. (b) Plan view image of a cubic mesostructured titania film.

Figure 4.3 Outline of selective etching on Si(111) surface to produce a quasi-hexagonal pit array.

Figure 4.4 SEM images of etched Si(111) substrates. (a) Plan view and (b) tilted.

Figure 4.5 Scheme of experimental setup for titania deposition.

Figure 4.6 Outline for titania deposition exclusively in the etched pit regions.

Figure 4.7 X-ray diffraction (XRD) patterns of titania nanobowls prepared by hydrolysis of $TiCl_4$ on silicon surfaces (black) and titania nanobowls annealed at 550 ºC in air for 3 hours (red). According to the XRD pattern, the titania nanobowls on etched silicon surfaces before annealing in air are amorphous. The peaks on the pattern of the annealed titania nanobowls correspond to anatase.

Figure 4.8 SEM images of titania nanobowls formed on etched silicon surfaces. (a) and (b) plan view, (c) - (f) side view.

Figure 4.9 Scanning Auger microscopy (SAM) mapping of titania nanobowls on silicon, (a) SEM image, (b) Ti LMM SAM, (c) Si KLL SAM, and (d) Ti LMM (red) and Si KLL (green) intensities overlaid on (a).

Figure 4.10 (a) SEM images and (b) scanning Auger microscopy (SAM) of titania nanobowls on etched silicon surfaces: (I) SEM, (II) Ti LMM (red) and Si KLL (green) intensities overlaid on (I), (III) Ti LMM SAM, and (IV) Si KLL SAM. The titania deposition lasted for 120 s.

Figure 4.11 (a) SEM images and (b) scanning Auger microscopy (SAM) of titania nanobowls on etched silicon surfaces: (I) SEM, (II) Ti LMM (red) and Si KLL (green) intensities overlaid on (I), (III) Ti LMM SAM, and (IV) Si KLL SAM. The titania deposition lasted for 1200 s.

Figure 4.12 (a) SEM image of etched silicon surface after titania deposition in which the oxidation time was 20 minutes. (b) Scanning Auger microscopy (SAM) images of the sample: (I) SEM image, (II) Ti LMM SAM, and (III) Si KLL SAM.

Figure 4.13 Formation of titania thin films on etched silicon surface.

Figure 4.14 SEM images of titania films formed over the entire etched surface followed by full oxidation by 30% (w/w) hydrogen peroxide treatment after HF etching.

Figure 4.15 Outline of formation of titania thin films on an etched Si(111) surface.

Figure 4.16 (a) and (b) Tilted SEM images of titania films formed exclusively on the silicon native oxide interface.

Figure 4.17 Plan view and tilted SEM images of titania nanobowls on etched Si(111) surfaces released through exposure to dilute HF (aq).

Figure 4.18 SEM images of released titania nanobowls in various orientations on etched Si(111) surfaces.

Figure 4.19 SEM image of released titania nanobowls on silicon surface after 3 min ultra-sonication in water.

Figure 4.20 SEM images of damaged titania nanobowls on silicon surfaces after 10 minutes etching with a 5% HF (aq) solution.

Figure 4.21 Mechanism of photodeposition of gold nanoparticles on titania surface under UV light.

Figure 4.22 SEM images of gold nanoparticle-decorated titania nanobowls.

Figure 4.23 (a) SEM image of a titania/gold-coated silicon surface. (b) Ti LMM Auger signal mapping, and (c) gold Auger MNN signals of the four different sites chosen from (a).

Figure 5.1 Solvothermal annealing of BCPs.

Figure 5.2 Isolated segment structures obtained by directed assembly of BCP.

Figure 5.3 Proposed strategy of localized BCP self-assembly in microwaves.

Figure 5.4 SEM images of localized BCP self-assembly in microwaves. (a) and (b) With Au nanostructures. (c) and (d) With silica nanoparticles.

Figure 5.5 Schematic illustration of thickness gradient on a surface.

Figure 5.6 (a) Schematic presentation of procedures for controlled self-assembly of BCPs using NIL. (b) SEM image of lines structures obtained from controlled self-assembly of PS-b-PMMA. (c) SEM image of PS domain structures on free-space surface. (d) AFM cross-section profile of an imprint-annealing sample.

Figure 5.7 (a) Schematic presentation of BCP self-assembly using a thermal nanoimprint process. Fluoroalkyl (FA)-modified homopolymer was used to promote mold release. (b) SEM image of self-assembled PS-*b*-PDMS thin films on PS-coated silicon substrates in the presence of FA-PS. (c) SEM image of directed self-assembled PS-b-PDMS in the presence of FA-PS. (d) Magnified image of (c). (e) SEM image of PS-*b*-PDMS nanostructures self-assembled in the absence of FA-PS additives during thermal imprinting process.

Figure 5.8 Schematic presentation of fabrication of patterned SSQ films using NIL technique.

Figure 5.9 Fast microwave annealing of BCPs with NIL on microwave transparent substrate.

List of Tables

Table 3.1 Wax melting test.

Table 3.2 Table of the PS-*b*-P2VP / PS-*b*-P4VP blends used in this study.

Table 3.3 Table of commercially available PS-*b*-P2VP BCPs used in this work, identified in the text by the letter given. Number averaged molecular weights of each block and overall polydispersity indices are listed.

List of Abbreviations

AES	Auger electron spectroscopy
AFM	Atomic force microscope
Aq	Aqueous
BCP	Block copolymer
DCB	Dichlorobenzene
DIB	Diiodobutane
DMF	N,N-dimethylformamide
EBL	Electron beam lithography
EUV	Extreme ultraviolet lithography
EUV-IL	Extreme ultraviolet interferometric lithography
HSQ	Hydrogen silsesquioxane
MIBK	Methyl isobutyl ketone
NIL	Nanoimprint lithography
NP	Nanoparticle
NPPOC-APTES	2-nitrophenylpropyloxycarbonyl-protected aminopropyltriethoxysilane
OTS	Octadecyltrichlorosilane
PDI	Polydispersity index
PEO-*b*-PMMA-*b*-PS	Poly(ethylene oxide-*block*-methyl methacrylate-*block*-styrene)
PEO-*b*-PPO-*b*-PEO	Poly(ethylene oxide)-*block*-poly(propylene oxide)-*block*-poly(ethylene oxide)

PHEMA	Poly(2-hydroxyethyl methacrylate)
PI-*b*-PS-*b*-PFS	Polyisoprene-*block*-polystyrene-*block*-polyferrocenylsilane
PIBMA	Poly(isobutyl methacrylate)
PMMA	Poly(methyl methacrylate)
PNPMA	Poly(neopentyl methacrylate)
PTFEMA	Poly(2,2,2-trifluoroethyl methacrylate)
PS-*b*-P2VP	Polystyrene-*block*-poly-2-vinylpyridine
PS-*b*-P4VP	Polystyrene-*block*-poly-4-vinylpyridine
PS-*b*-PDMS	Polystyrene-*block*-Poly(dimethylsiloxane)
PS-*b*-PEO	Polystyrene-*block*-poly(ethylene oxide)
PS-*b*-PFS	Polystyrene-*block*-polyferrocenyldimethylsilane
PS-*b*-PMMA	Polystyrene-*block*-polymethylmethacrylate
SAIL	Self-aligned imprint lithography
SAM	Self-assembled monolayer
SAM	Scanning Auger microscopy
SEM	Scanning electron microscope
SFM	Scanning force microscopy
SSQ	Silsesquioxane
TALH	Titanium(IV) bis(ammonium lactate) dihydroxide
THF	Tetrahydrofuran
TMAH	Tetramethylammonium hydroxide
UV	Ultraviolet

UV-NIL	Ultraviolet-based nanoimprint lithography
XPS	X-ray photoelectron spectroscopy
XRD	X-ray diffraction

Chapter 1
A Brief Introduction to Block Copolymer Lithography

This thesis addresses new approaches to achieve rapid self-assembly of block copolymers (BCPs), to control the BCP-induced feature spacings, and to build nanostructures using BCP thin films as templates. The fabrication strategies, experimental designs, and characterization of the resulting nanostructures will be presented.

This chapter, an overview of the entire thesis, includes a background to BCP self-assembly. After a brief introduction to the history of printing and lithography, two of the most important conventional lithography techniques - photolithography and electron beam lithography - will be discussed, listing their advantages and limitations. The concept of BCP lithography will be addressed as the main content in this chapter. Significant challenges remain for BCP lithography to be successfully commercialized, such as how to reduce the defects in the system, how to increase the ordering speed, and how to control the orientation of self-assembly. This thesis discusses the perfection and registration of BCP self-assembly systems. Examples that deal with reducing the defect density and controlling BCP self-assembly using conventional top-down lithography techniques will also be presented.

1.1. Background

Moore's Law states that the number of devices on an integrated chip doubles about every 18 months.[1] The drive to maintain the rapid speed of shrinking half-pitch, which is half the distance between identical features in an array (Figure 1.1), continues in the semiconductor manufacturing industry. As stated in the International Technology Roadmap for Semiconductors (ITRS-2009),[2] the challenge of improving the resolution and extending the applications of the well-established optical-based lithography technology while simultaneously developing alternative technologies to replace optical lithography must be overcome. It is also critical that the fabrication costs remain economical while the functionality of a chip becomes greater. Lloyd R. Harriott mentioned in 2001 that the improvements in lithography led to roughly half of the density improvements in industry.[1] Lithography is, however, the single most expensive cost factor in integrated chip manufacturing.[3] The self-assembly of BCPs is now emerging as a complementary strategy to photolithography due to its cost-effective nature and its compatibility with the existing manufacturing processes.[4–6] The processing advantages of BCPs include readily controllable feature sizes by tuning the molecular weights, the tendency of BCPs to form spontaneous self-oriented uniform patterns over a large area, and the achievable various nanostructures, such as spheres, cylinders, gyroids, and lamellae. Sub-lithographic resolution could be achieved by combining these self-assembled patterns with lithographically defined patterns.[2] There is no doubt that BCP self-assembly is a potential approach to produce sub-50 nm features and that the self-assembled

dense arrays of nanostructures offer feature resolutions that are too expensive or too difficult to be fabricated by conventional lithography for some applications. However, it is unlikely that BCP self-assembly is going to replace conventional lithography processing, as addressed by Charles T. Black, who stated, "*The semiconductor industry will likely never abandon photolithography as its primary patterning approach but will rather increasingly seek symbiotic techniques for augmenting lithographic resolution capabilities.*".[5,7]

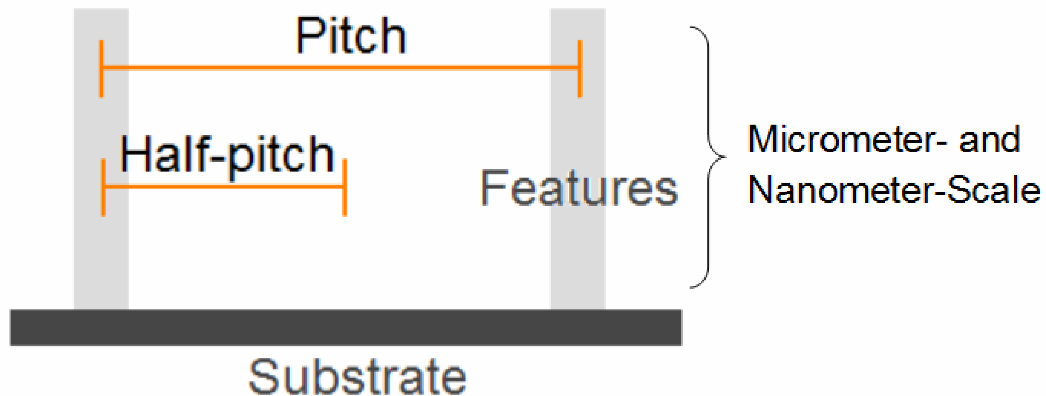

Figure 1.1. Basic Schematic illustration of "pitch" and "half-pitch".

1.2. Conventional Lithography Techniques

History of Printing

The earliest surviving examples of wood-block printing from China, dependent on the two inventions of paper and ink, date back to 220 AD.[8] The way the Chinese used to print was very simple: the text was first written on a piece of thin paper that was then placed face down onto a wooden plate, followed by carving out the characters to make a solid printing plate. The major

disadvantage of wood-block printing is that it took a long time to fabricate the printing blocks since a new block had to be carved for every page in a book. Movable type was invented during the Song Dynasty (960-1279) in China by Bi Sheng. Individually carved characters on identical pieces of clay were used in the movable type printing system. To make the pieces, one Chinese character was carved in relief on a piece of soft moistened clay that was hardened by firing after carving. The pieces of characters were then assembled to allow printing.

Lithography (from Greek, *lithos*, meaning stone and *graphein*, meaning to write), invented in 1796 by Bavarian author Alois Senefelder, is a method of mass producing patterns transferred from a solid master plate to smooth surfaces.[9] It works on a simple principle that oily substances and water repel each other. To transfer ink to the blank paper sheet to produce a printed page, a stone with a flat surface is first marked with crayon or other waxy (hydrophobic) substance and coated with a thin layer of water (hydrophilic). When the ink is applied, it is attracted exclusively to the hydrophobic area and repelled by the hydrophilic area.

Unlike other lithography techniques that will be discussed next, such as light, e-beams, and X-rays, the resolution of most printing techniques is not a strong driving force for improvement since the naked human eye can only observe objects as small as ~50 μm.[10] However, for the modern lithography techniques that will be discussed here, resolution is critical.

Photolithography

Photolithography/optical lithography is a long-standing technology that is widely used in the semiconductor industry to produce micrometer-sized features by selectively removing/etching parts of a thin film (Figure 1.2).[7,11–16] In photolithography, a photosensitive material is first coated onto a substrate and exposed to a light source through a mask. The exposure leads to a chemical change in the exposed regions of the photosensitive material that can be selectively removed or retained by a developing solvent, leaving a positive or negative pattern on the surface.

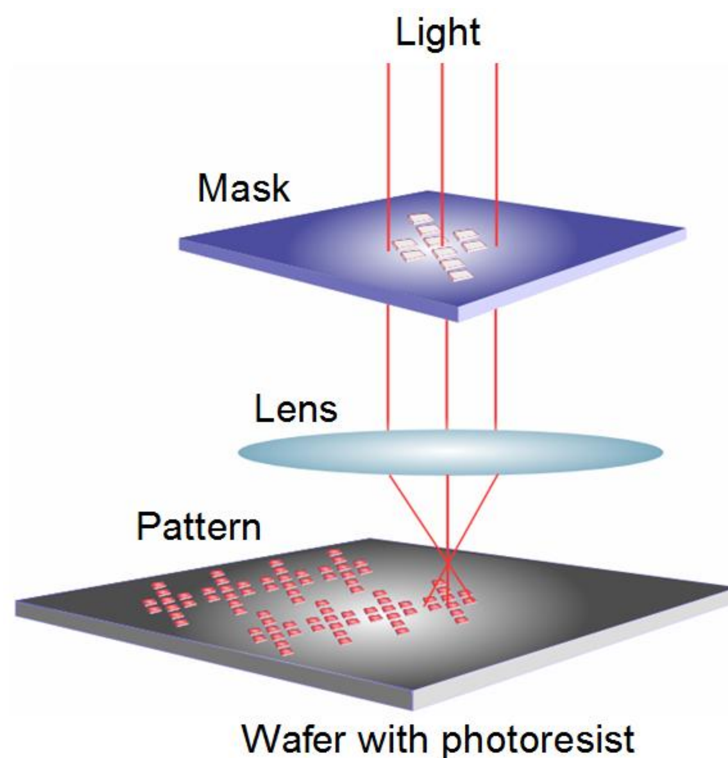

Figure 1.2. Basic schematic illustration of how photolithography works. Patterns are created on a wafer by using a light source to expose photoresist-coated surfaces through a photo mask.

The primary advantage of optical lithography is the capability of simultaneous fabrication of many features on large areas, which allows high throughput and low cost. The major limit of optical lithography is, however, the resolution. The resolution of optical lithography is determined by the Rayleigh equation in which the resolution is proportional to the exposure wavelength and inversely proportional to the numerical aperture of the optical system.[1] To improve the resolution of photolithography, the wavelength of the light source needs to be reduced, and the photoresist materials, processing equipment, photomask and optical illumination techniques need to be improved.[1,17] For the semiconductor industry, it is critical that manufacturing costs remain economic in step with developments in design and processes. According to the ITRS roadmap, the leading candidate for next generation lithography approaches is extreme ultraviolet lithography (EUV).[2] However, major challenges still remain and are numerous, such as the power source, cost of ownership, high-resolution resists, and defects in masks. If all these issues cannot be solved or improved simultaneously, the EUV technique will not be cost-effective.[2]

In order to further extend the limits of photolithography, unconventional approaches have been investigated as described in the following example. As shown in Figure 1.3, Weaver and coworkers demonstrated an example of patterning self-assembled monolayers (SAMs) using an unconventional parallel scanning near-field photolithography. 2-nitrophenylpropyloxycarbonyl-protected aminopropyltriethoxysilane (NPPOC-APTES) was used as a photosensitive SAM

on silicon dioxide surfaces. As illustrated in Figure 1.3 (d), the NPPOC protecting group could be cleaved to yield an amine functional group under UV exposure. By using a Snomipede probe array to control the UV irradiation [Figure 1.3 (a)-(c)], features could be written on the surface and imaged by atomic force microscopy (AFM).[18]

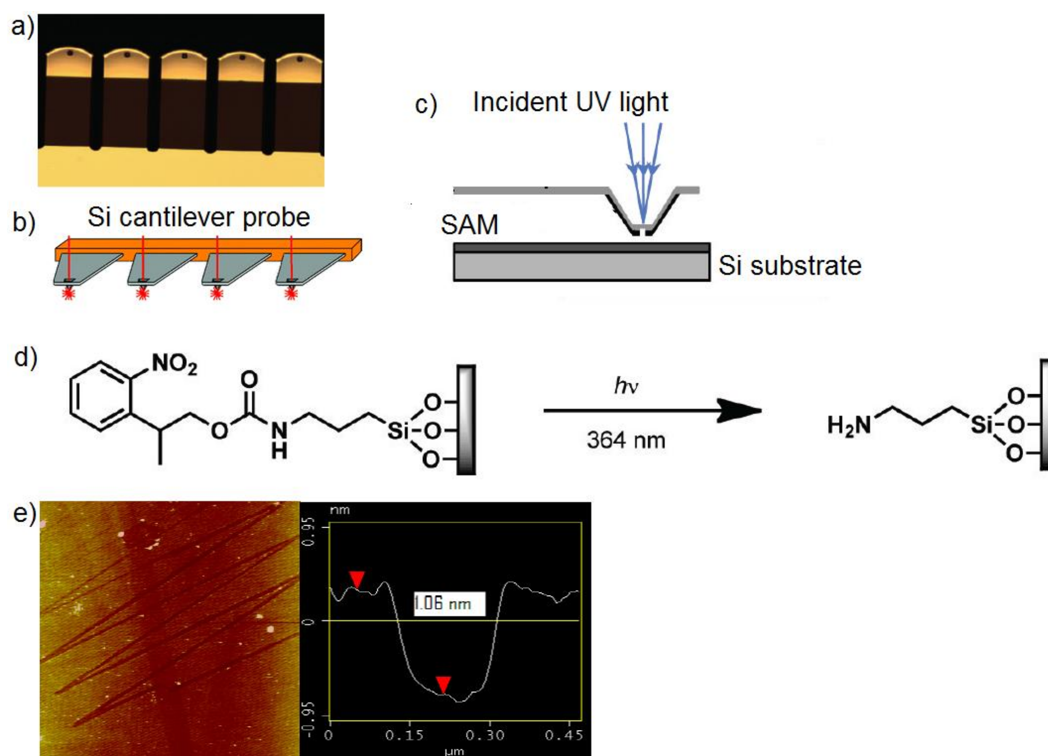

Figure 1.3. (a) Picture of the probe array used in the parallel scanning near-field photolithography. (b) and (c) Schematic outline of the silicon cantilever probe. (d) Schematic outline of photodeprotection reaction of NPPOC-APTES. (e) AFM height image of a zigzag pattern created by parallel scanning near-field photolithography. Reprinted with permission from ref. 17. Copyright © 2010 American Chemical Society.

Electron Beam Lithography (EBL)

E-beam lithography utilizes a beam of electrons, rather than photons, to create features on a resist covered surface.[19] Unlike photolithography, EBL is a mask-free direct writing system. As illustrated in Figure 1.4, the typical procedure of EBL involves coating the substrate with a resist, "writing" on the resist with an e-beam, and finally removing either the exposed or non-exposed areas of the resist to obtain positive or negative patterns. The primary application of EBL is in making masks for photolithography because the resolution is not restricted by the diffraction limit of light. In addition, EBL has a resolution down to a few nanometers as well as a large depth of focus. However, in the mass-production industry, the key limitation of EBL is the very low throughput that is the result of the very long writing time. For example, exposing a region of 1 cm^2 would take ~10 days; covering a 12 $inch^2$ silicon wafer would take two decades, making EBL 10 million times slower than current photolithography systems.[2] Another drawback of EBL is the high cost - each EBL writing system itself costs ~$4 million.[20]

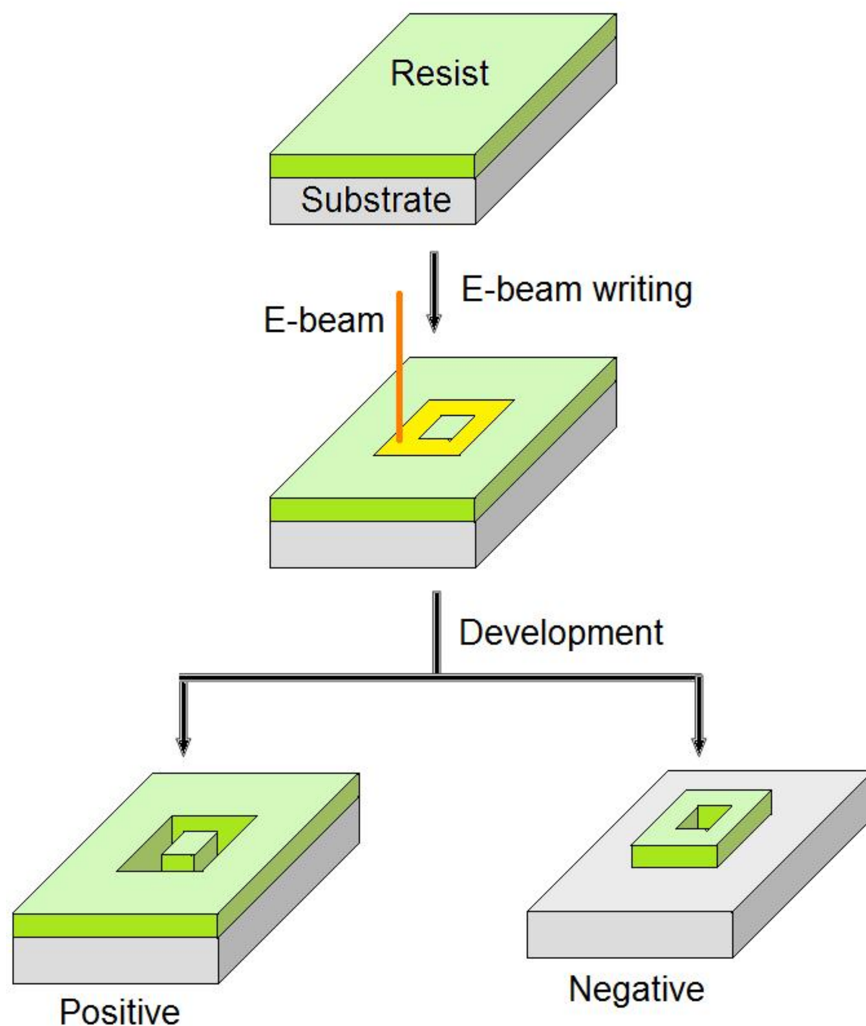

Figure 1.4. E-beam lithography can be used to write either positive or negative patterns in a resist. When positive resist is used, developer solution removes exposed material, leaving positive patterns on the surface; when negative resist is used, developer solution removes unexposed material, leaving negative patterns on the surface.

EBL has also been used for fundamental research. For example, Rastogi *et al.* recently reported the direct fabrication of patterned polymer SAMs *via* a single step EBL process.[21] Polymer SAMs of poly(methyl methacrylate) (PMMA), poly(2-hydroxyethyl methacrylate) (PHEMA), poly(isobutyl

methacrylate) (PIBMA), poly(neopentyl methacrylate) (PNPMA), and poly(2,2,2-trifluoroethyl methacrylate) (PTFEMA) were patterned on silicon substrates with a resolution down to 50 nm using the direct e-beam patterning (Figure 1.5). This direct patterning of SAMs using e-beam degradable methacylate polymer is a simple and efficient method to fabricate patterned macromolecular architectures with nanoscale precision.

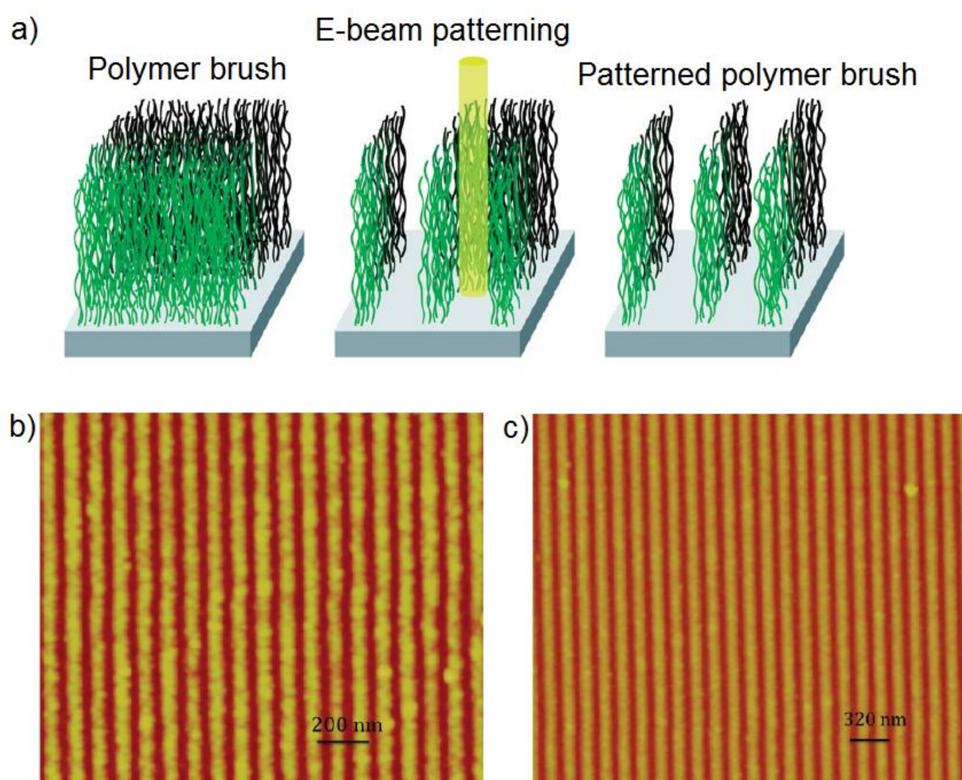

Figure 1.5. (a) Schematic outline of the direct pattering of polymer SAMs using EBL. (b) and (c) AFM height images of EBL patterned PIBMA and PNPMA SAMs, respectively. Reprinted with permission from ref. 10. Copyright © 2010 American Chemical Society.

Nanoimprint Lithography (NIL) & Self-Aligned Imprint Lithography (SAIL)

Nanoimprint lithography (NIL) is a nonconventional lithographic method that is high-throughput, low-cost and consists of a much simpler process than photolithography and EBL.[22] In NIL, nano-scaled features are fabricated by mechanical or chemical deformation of the resist with a subsequent etching process. NIL has two primary forms: hot embossing NIL and ultraviolet-based nanoimprint lithography (UV-NIL), as shown in Figure 1.6. With hot embossing NIL, a thermoplastic resist is first spin-coated onto a substrate. The resist-coated substrate is then heated to a specified temperature, and a hard mold with a surface relief pattern is applied to the surface. The substrate and the mold are then cooled. After the mold is removed, the resist coating on the substrate is "imprinted" with a reverse pattern from the template. In UV-NIL, the substrate is first coated with a photo-curable resist which is a low viscosity, photopolymerizable organosilicon solution. A transparent hard mold with surface relief pattern is then applied on the resist at room temperature and UV exposure is used to cure the solution. When the mold is removed from the surface, it leaves the reverse pattern on the surface.[23–26]

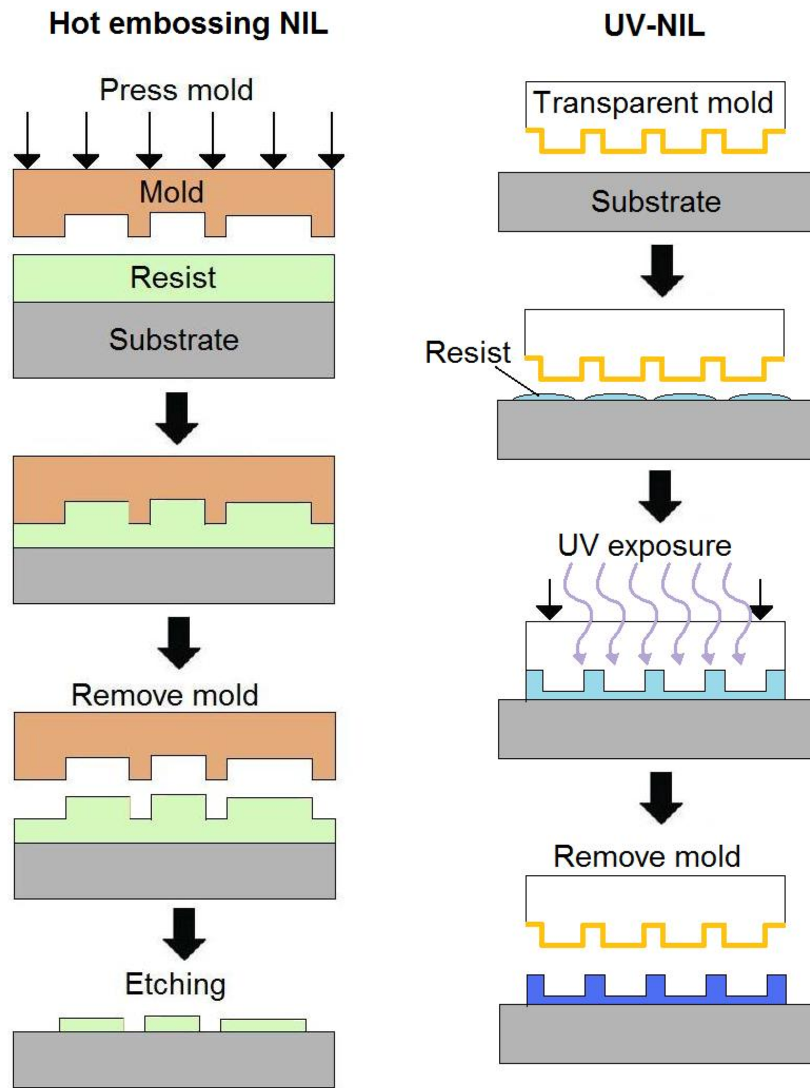

Figure 1.6. Schematic outline of the NIL process. In hot embossing NIL (left), a hard mold with a surface relief pattern is applied to the surface when it is heated to a specified temperature. In UV-NIL (right), a transparent hard mold with surface relief pattern is applied on the resist-coated surface and UV exposure is used to cure the photo-curable resist.

Another state-of-the-art technique is self-aligned imprint lithography (SAIL), an imprint process developed by HP Labs.[27,28] Unlike conventional photolithography in which different masks and multiple alignment steps are

required for each layer, SAIL encodes multiple patterns into different heights of the masking structures. No alignment is needed in SAIL since all of the patterning information is impressed onto the template as a single three-dimensional masking structure.

1.3. BCP Nanolithography

As optical lithography approaches its fundamental limits in feature resolution, new economical strategies are sought to complement these powerful technologies and achieve sub-50 nm scale accuracy in a cost-effective manner.[1,17,29] Of the new approaches, self-assembly is now emerging as one powerful option and the use of self-assembled BCPs to generate organized nanostructures at the sub-50 nm scale is the subject of intense research.[30–38] The domain structures in BCP thin films provide a variety of templates for pattern transfer. The two conventional means to achieve dimensional uniformity and organization of BCP thin film templates are solvent annealing and thermal annealing. With such materials, feature sizes down to a few nanometers can now be generated, while somewhat larger polymers can be used to produce patterns that reliably extend across very large areas or with very low defect densities.[39] Figure 1.7 shows four examples of metal nanostructure patterns on silicon substrates obtained by using self-assembled BCP thin films as the template.

BCP self-assembly could be an extension to photolithography because BCPs are comparable to the silicon based processing in the semiconductor industry and the physical property of BCPs is similar to that of the photoresists.

Mansky and coworkers first proposed the idea of using BCP thin films as masks to generate lithographic features in 1995.[40] During the last decade, BCP self-assembly has received remarkable attention. However, there are still many problems that need to be solved before BCP self-assembly can be effectively used in semiconductor fabrication processes, including how to reduce the defects of the self-assembled patterns; how to accurately control the registration; and how to increase the self-assembly speed.

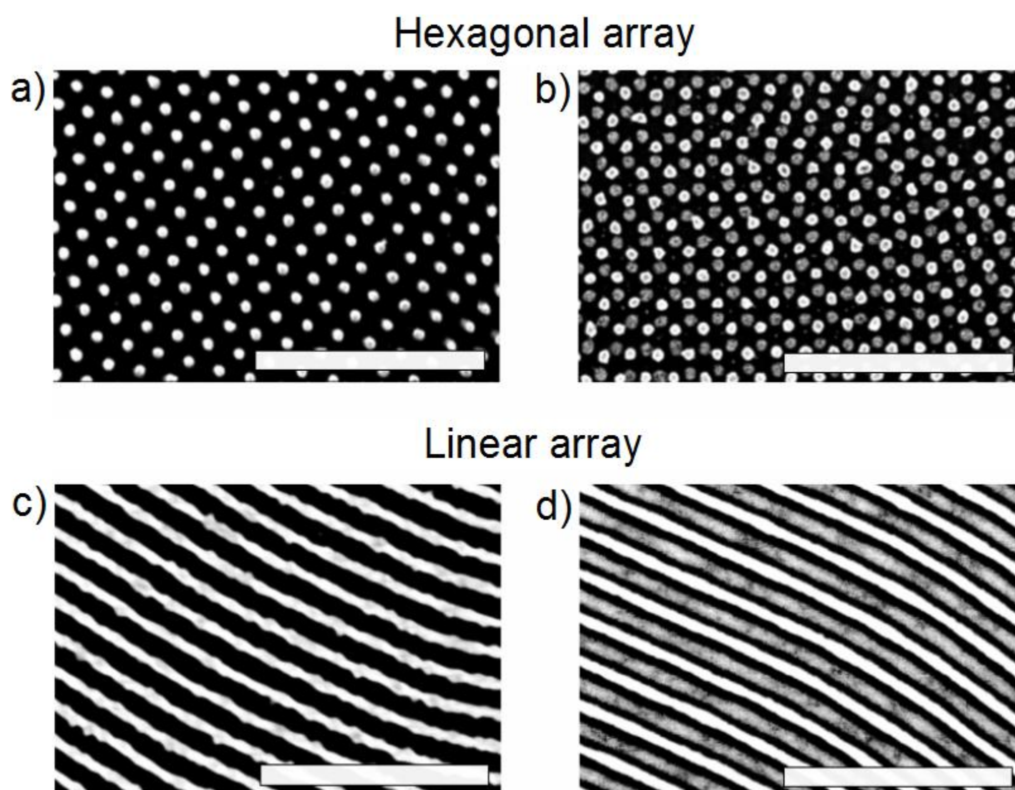

Figure 1.7. SEM images of Pt nanostructures templated by self-assembled BCPs. (a) and (b), hexagonal arrays. (c) and (d), linear arrays. Scale bar = 500 nm.

Self-Assembled BCP Microdomains with Low Defect Density and High Alignment

As already mentioned, one of the driving forces for the intense research on BCP lithography is compatibility with existing semiconductor processing techniques. The limitation of self-assembled BCP thin films is that periodic microdomain ordering with zero defects can only be achieved over "small" areas at the micrometer-scale.[39] The ordering uniformity largely depends on the BCP phase-separation thermodynamics, polydispersity (PDI), and the quality of the surfaces.[41–43] As mentioned in the ITRS roadmap, if block copolymer self-assembly is to be considered as a competitive patterning option for many advanced applications, it must be capable of forming patterns with smaller sizes, larger densities, and low defect density, comparable to that which can be achieved by conventional lithographic methods.[2] To meet the industrial fabrication requirement, the defects in the self-assembled BCP systems need to be reduced and BCP self-assembly must be able to form structures in desired locations with respect to existing structures on the surface. Several approaches, such as graphoepitaxy and chemically prepatterned surfaces (Figure 1.8), have been used to achieve a low-defect level and to control the orientation of BCP microdomains in the self-assembly systems.[10]

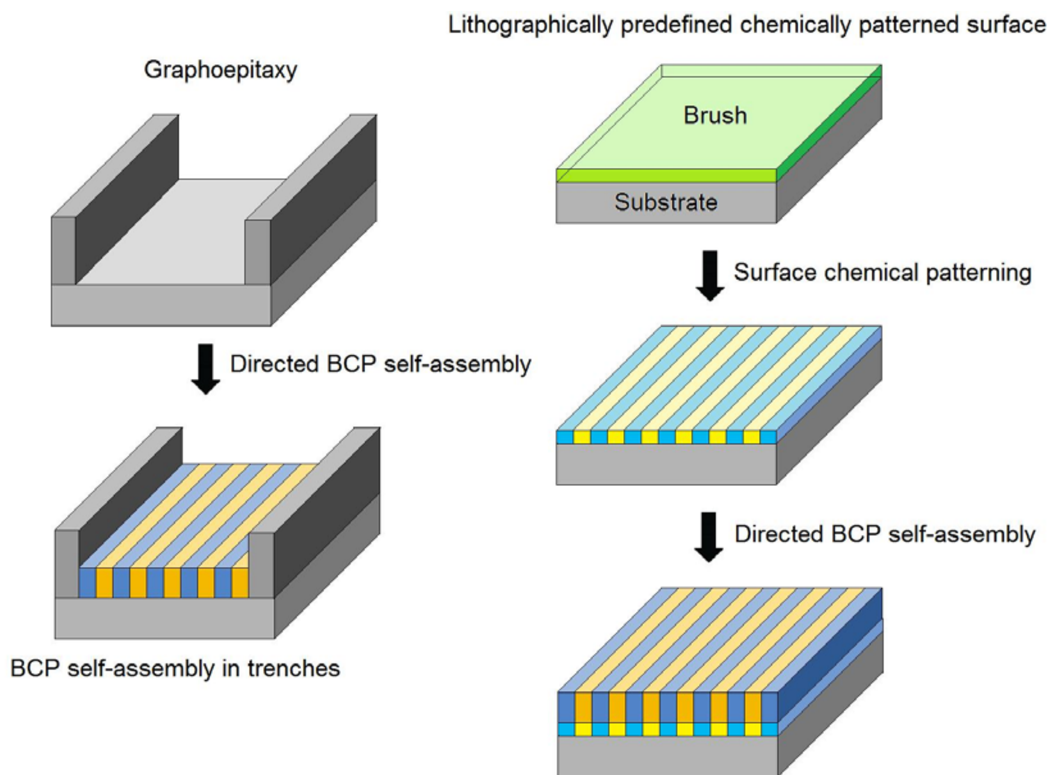

Figure 1.8. Directed self-assembly of BCPs on topological feature-defined surface and lithographically predefined chemically patterned surface.

Graphoepitaxy uses topographic features that are created by lithography to direct the ordering of BCP thin films. Sublithographic resolution (higher resolution compared to the maximum resolution allowed by the previously established lithography methods) is achieved using graphoepitaxy since the microdomains in BCPs self-register to the lithographically defined pattern.[44–46] One advantage of graphoepitaxy is that the topographic patterns are easy to fabricate using conventional photolithography. The key to such a spontaneous alignment of self-assembled BCPs is the surface property of the topological features in terms of the preferential wettability of one of the domains of the BCP.[47] Therefore, the quality of a graphoepitaxy-guided self-assembled patterns

largely depend on the quality of the lithographic pattern. Kramer and coworkers first used graphoepitaxy to produce spherical polystyrene-*block*-poly-2-vinylpyridine (PS-*b*-P2VP) domains with long-range order in good quality.[48,49] For controlling the orientation and registration of the PS-*b*-P2VP domains using photolithographic etched rectangular mesas on silicon substrates, it is found that the width of the mesa is vital to obtain good alignment. Three dimensional self-assembly of spherical-morphology polystyrene-*block*-polyferrocenyldimethylsilane (PS-*b*-PFS) BCP was studied by Chuang *et al.* using V-shaped trenches that were etched on silicon substrates (Figure 1.9).[50]

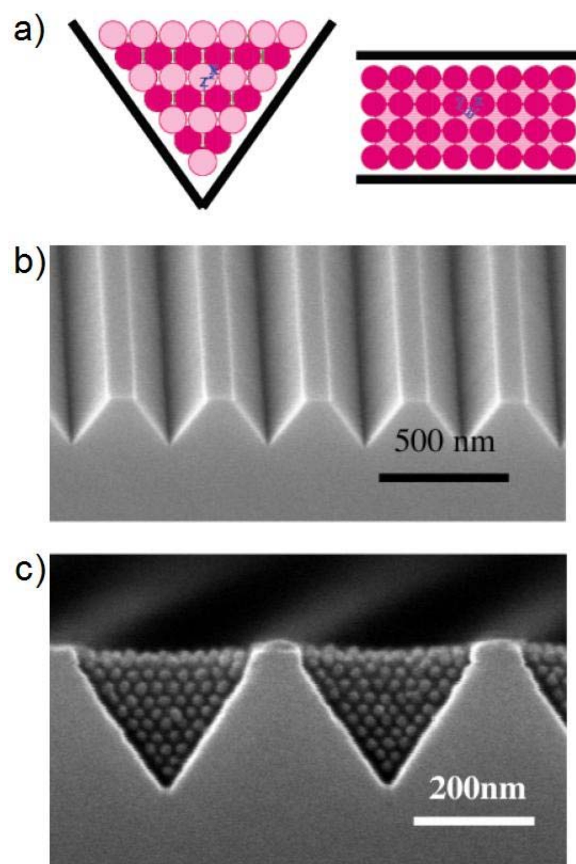

Figure 1.9. (a) Schematic representation of the packing of spheres within a V-shaped groove. (b) SEM image of V grooves etched in a Si (100) substrate. (c) SEM image of PS-PFS films in V grooves after annealing and etching. Reprinted with permission from ref. 36. Copyright © 2006 American Chemical Society.

To largely reduce the number of defects in the self-assembled patterns, Russell and coworkers described a new approach to control the self-assembly of polystyrene-*block*-poly(ethylene oxide) (PS-*b*-PEO) BCP microdomains using faceted surfaces of commercially available sapphire substrates.[39] The faceted sapphire surfaces were obtained by annealing in air at 1300 ~ 1500 °C for 24 hours to form a sawtooth pattern. Then BCPs were spin-cast onto the sapphire surface and a solvent annealing process was applied to the BCP thin films.

Highly ordered arrays with long-range crystalline order were formed on the surfaces. Furthermore, feature sizes as small as 3 nm in diameter were achieved as well as low pattern defect density and high area densities (10 terabits per square inch). This work opened the door for low defect, high-density systems. The simplicity of this concept makes it attractive; however, the highly ordered patterning largely depends on the substrate topography.

The second route that has been used to obtain ultra-low defect BCP self-assembly systems and to register and align phase-separated BCP microdomains is lithographically defined surface chemical nanopatterns.[51] In these approaches, an organic thin film with a thickness of a few nanometers (called "brush") is first deposited on a substrate; then a precisely predefined pattern is transferred to the surface by using a high-resolution lithography technique such as EBL or EUV. The key of the predefined pattern is to create a modified surface with regions of different surface energies and chemistries. When BCP is coated on the pre-patterned surface and annealed, the two blocks in the BCP tend to phase-separate and preferentially migrate towards the chemically compatible regions on the surface to achieve minimum surface free energy (Figure 1.10). Using a chemically patterned surface to orient the long-range order of BCP self-assembly was first proposed by Krausch and coworkers.[52] In the original work, pre-patterned SAM on a Au substrate with regions of different surface energies was used to guide the phase-separation of a homopolymer blend (PS/PVP, 1:1 w/w). In another example, chemically striped surfaces were used to direct the self-assembly of poly(styrene-block-methyl methacrylate) (PS-*b*-PMMA) to obtain

defect-free patterns by Nealey and coworkers.[51,53] The integration of PS-*b*-PMMA thin films with extreme ultraviolet interferometric lithography (EUV-IL)-defined surface patterns led to self-registered, defect-free structures. The quality of the self-assembled BCP domain structures was determined by the size and quality of the underlying lithographic pattern. It is found that when the dimensions of the BCP microdomains match the dimensions of the underlying chemical pattern, defect-free assemblies can be achieved. However, if the contrast of the two chemically different regions is strong enough, self-assembled defect-free patterns can also be obtained even in the presence of significant mismatch between the dimensions of the BCP microdomains and the dimensions of the lithographically defined surface pattern.[54,55]

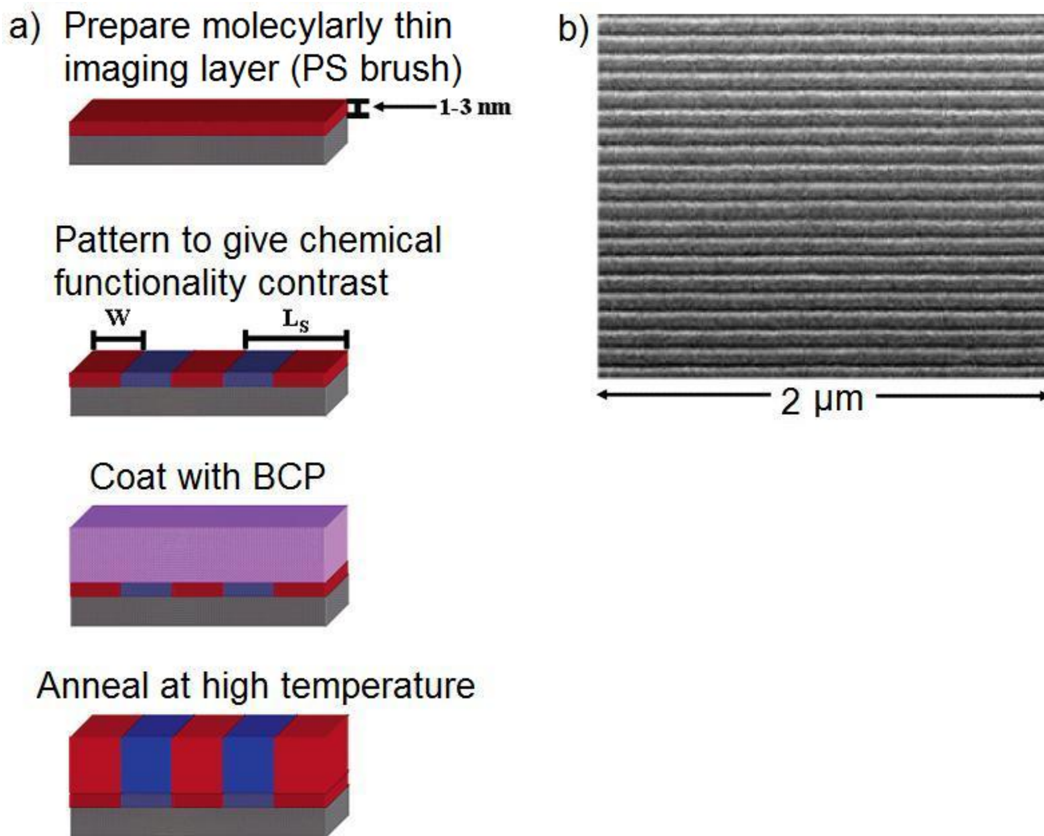

Figure 1.10. (a) Schematic representation of BCP lithography process using a chemically pre-patterned surface to direct the assembly of the BCP domains in registry with the underlying surface pattern: standard lithographic procedures were used to create a periodic pattern on an ultrathin organic imaging layer-coated substrate. Then a BCP thin film was coated on the chemical surface pattern and thermal-annealed. (b) SEM images of PS-*b*-PMMA domains annealed on chemical surface patterns. Reprinted with permission from ref. 37. Copyright © 2007American Chemical Society.

Kim and coworkers recently demonstrated a simple approach to align BCPs with a lamellar array over a large area by combining graphoepitaxy with a chemically patterned surface (Figure 1.11).[56] Instead of employing EBL or EUV to prepattern the underlying surface, conventional photolithography was used to

create topographical photoresist features on a polymer brush-coated surface. When BCP was graphoepitaxially assembled on the surface and partially etched, the resulting BCP thin film was used as a mask to etch the underlying surface. Once the residual BCP and photoresist were removed, the chemically patterned surface could be used for epitaxial block copolymer self-assembly. This approach is a good example of the high compatibility of BCP self-assembly with a standard conventional photolithography process.

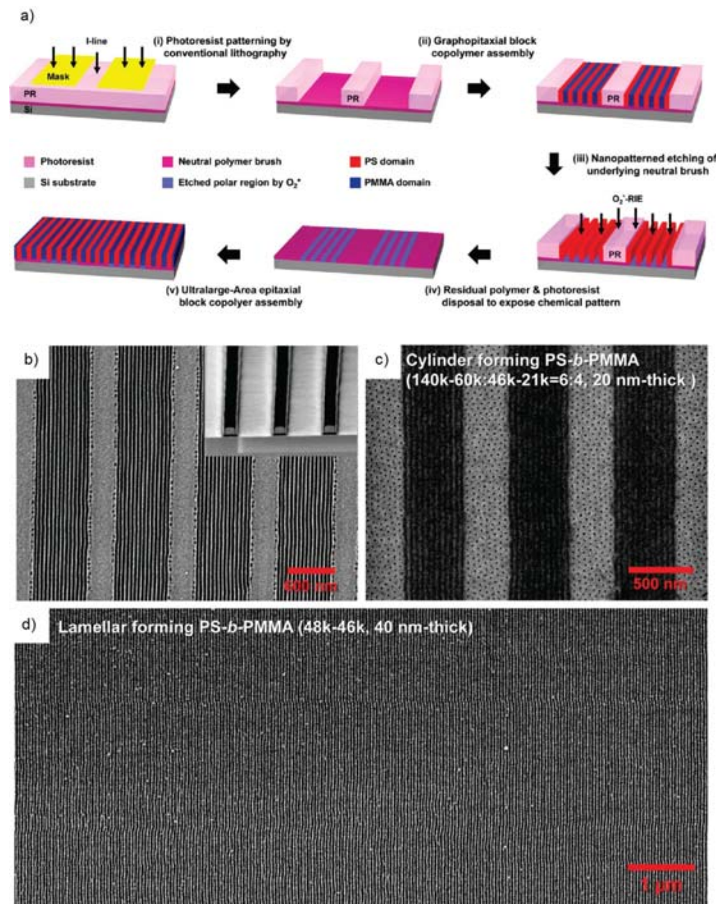

Figure 1.11. (a) Schematic representation of BCP lithography procedure to align BCP domains in an ultra-large area: (i) Conventional I-line lithography was used to pattern graphoepitaxial features on a neutral polymer-brush-coated Si substrate. (ii) BCP self-assembly was confined within the graphoepitaxial features. (iii) Self-assembled BCP patterns were used to selectively etch the underlying polymer brush layer. (iv) Residual photoresist and polymer were removed to expose the chemical nanopattern. (v) BCP self-assembly in an ultra-large area on chemically patterned surface. (b) Lamellar forming BCPs self-assembled within photoresist trenches. (inset image: graphoepitaxial pattern prepared by I-line photolithography). (c) Cylinder forming PS-*b*-PMMA BCP self-assembled on chemically patterned substrates. (d) Lamellar forming PS-*b*-PMMA BCP self-assembled on chemically patterned substrates. Reprinted with permission from ref. 39. Copyright © 2010 American Chemical Society.

Another approach that can also achieve a defect-free system is the ABC triblock copolymer strategy.[57] Triblock copolymers of poly(ethylene oxide-*b*-methyl methacrylate-b-styrene) (PEO-*b*-PMMA-*b*-PS), in which the PMMA was used as a sacrificial block, were synthesized by controlled living radical polymerization in order to combine the facile degradation of PS-*b*-PMMA with the long-range lateral order of PS-*b*-PEO. This method led to defect-free nanoporous arrays. The morphology of the corresponding thin films was studied by scanning force microscopy (SFM) (Figure 1.12).

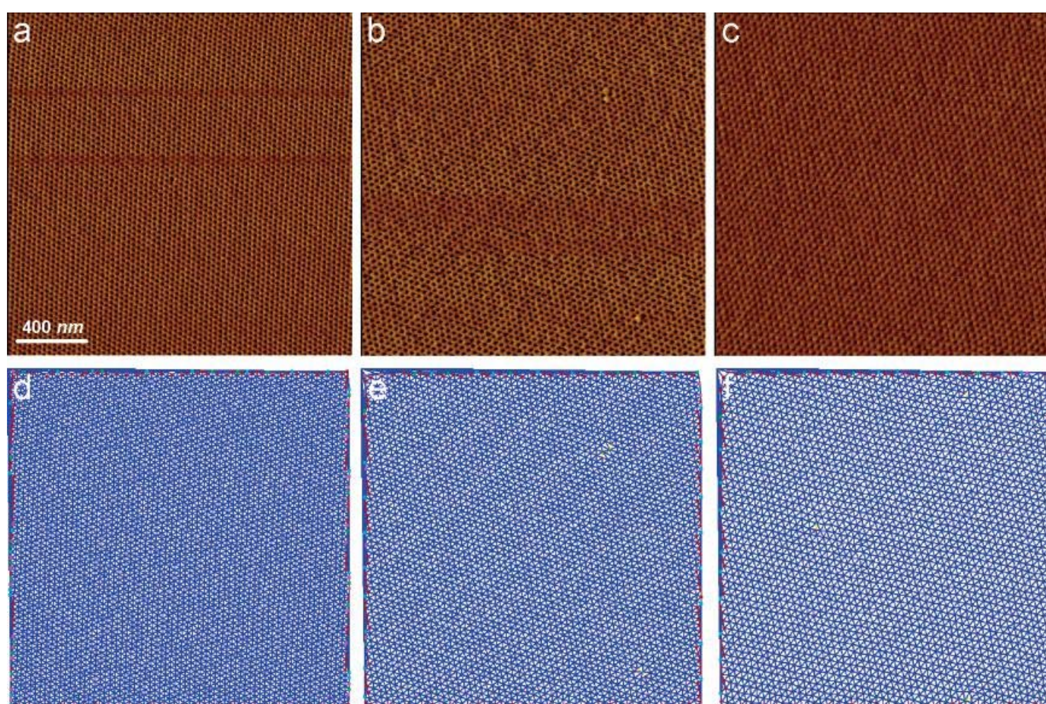

Figure 1.12. (a)-(c), SFM phase images of highly ordered PEO-*b*-PMMA-*b*-PS triblock copolymer thin films that were solvent-annealed for 12 h in a benzene vapor.. (d)-(f) are triangulation images corresponding to SFM images shown in (a)-(c), respectively. Reprinted with permission from ref. 28. Copyright © 2006 American Chemical Society.

1.4. Applications of BCP Self-Assembly

BCPs are powerful candidates for potential advanced applications in areas of information storage, photonic crystals, and drug delivery,[58–62] and because of their self-organizing capability, tremendous research efforts have been made over the last few years to study the BCP functionalized surfaces.[63–66] One of the most important applications of BCP self-assembly is the usage of phase-separated BCP thin films as patterning templates. Since BCPs self-assemble to form dense arrays of nanostructures, BCP lithography provides a simple way to mass-produce nanoscale features. The phase separation of chemically distinct blocks brings a platform to deposit nanomaterials, such as metals and oxides, in desired microdomains of BCP thin films. Preferential deposition of Au nanoparticles on the PS domains in PS-*b*-PMMA was first demonstrated by Sita and coworkers.[67] Alkane- and arenethiol-passivated gold nanoparticles were deposited on PS-*b*-PMMA films and because of the different interaction energies between the passivants and the two blocks, nanoparticles were preferentially adsorbed to the PS microdomains. Using a chemical reduction, Valetsky and coworkers demonstrated a way to prepare gold nanoparticles with gold salt-loaded PS-*b*-PVP BCP micelles (Figure 1.13).[68]

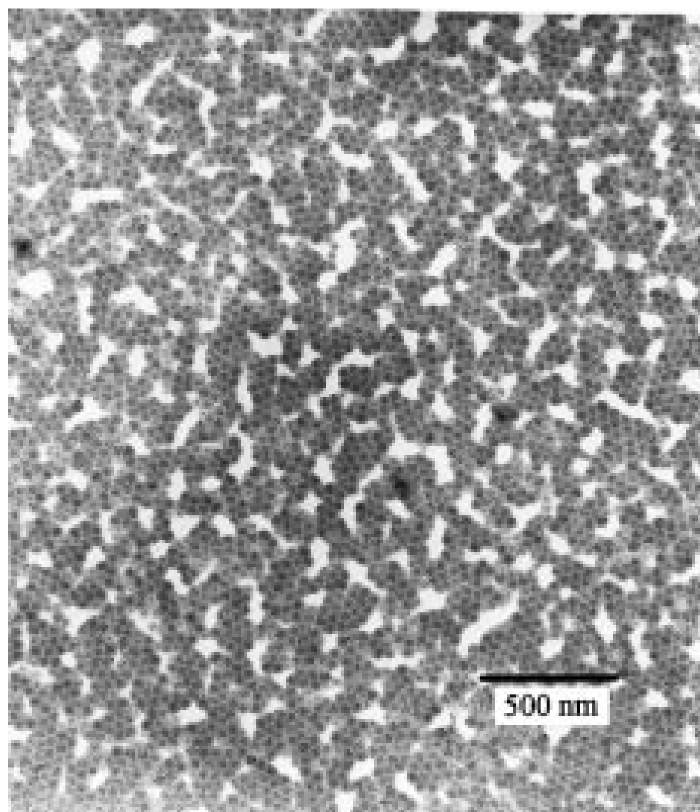

Figure 1.13. TEM image of gold nanoparticles patterned by PS-*b*-P4VP BCP. Reprinted with permission from ref. 41. Copyright © 1999 American Chemical Society.

The use of high-quality poly(styrene-*b*-dimethylsiloxane) (PS-*b*-PDMS) linear patterns to fabricate an extensive set of metal nanowire arrays, including Ti, W, Pt, Co, Ni, Ta, Au, and Al, with widths down to 9 nm, was demonstrated recently.[69] As shown in Figure 1.14, PS-*b*-PDMS was first solvent-annealed and plasma etched to form a thin film of PDMS cylinders on the surface, and a metal film was then deposited on top of the PDMS grating pattern. Due to the different plasma etching rates of PDMS and metal, further etching resulted in aligned metallic wire patterns.

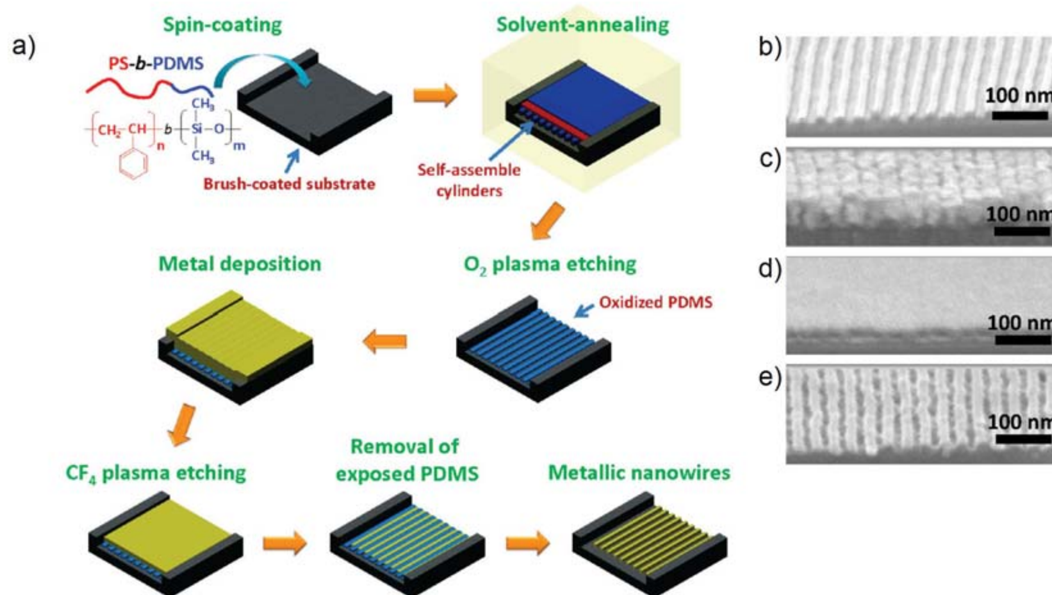

Figure 1.14. (a) BCP self-assembly and plasma etching were used to pattern metallic nanowires on a substrate. (b) SEM image of the oxidized PDMS pattern after self-assembly and reactive ion etching. (c) SEM image of the oxidized PDMS pattern after metal deposition. (d) SEM image of metal surface after plasma etching. (e) SEM image of metallic nanowires. Reprinted with permission from ref. 42. Copyright © 2010 American Chemical Society.

Another example of using BCP thin films as templates to pattern metallic nanostructures involves combining BCP self-assembly with a top-down "microcontact deprinting" technique (Figure 1.15). Lensen and coworkers demonstrated a simple patterning method for gold nanoparticles using a topographically micropatterned polystyrene (PS) stamp to selectively deprint parts of the BCP pattern.[70] This technique provides a fast and economic way to obtain hierarchical patterns of nanoparticles on the surface.

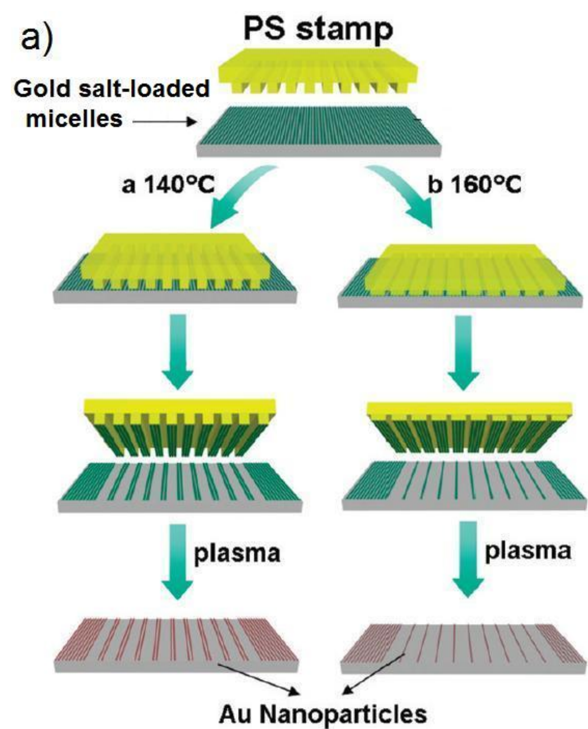

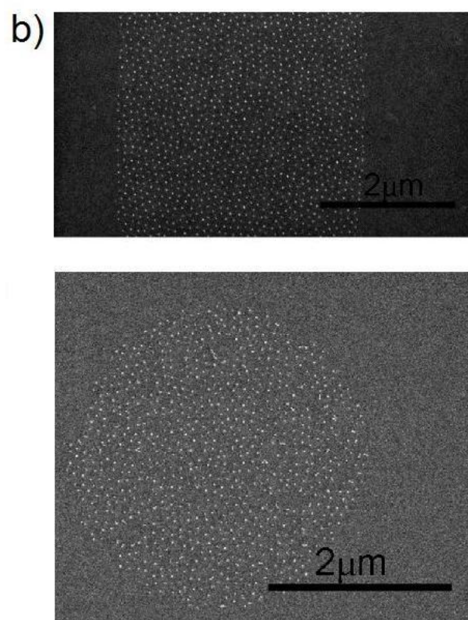

Figure 1.15. (a) Schematic representation of deprinting process on a silicon substrate with a monolayer of gold salt-loaded BCP micelles using a PS stamp. Different patterns can be obtained with the same PS stamp at different temperature. (b) SEM images of hexagonally arranged Au nanoparticle patterns on silicon substrate. Reprinted with permission from ref. 43. Copyright © 2009 American Chemical Society.

From a commercial point of view, the long-range of ordering and precise registration brought by BCP self-assembly reaches industry standards for producing integrated circuits.[71] The immediate application of BCP self-assembly in integrated circuit manufacturing is in products that only require pattern uniformity, such as dot and rod arrays.[30,53,72–74] One of the most commonly used BCPs is PS-*b*-PMMA, which can be used for lithographic masks to produce dot arrays, vertical rods, or nanopores. For example, Black and coworker utilized the self-assembled PS-*b*-PMMA structure as a template to fabricate high density decoupling capacitors.[75] For industrial applications, self-assembled layers of PS-*b*-PMMA which contains hexagonal arrays of cylindrical holes are used as nanolithography templates for the fabrication of IBM's air gap microprocessors.[76] BCP thin film masks are also used for patterning high-density dot arrays patterned on semiconductor surfaces for magnetic data storage applications.[77] For uniformly ordered dot arrays, the hexagonal structures formed by BCP self-assembly are not consistent with the industry standard rectilinear coordinate system. Efforts have been made to achieve ordered square arrays from BCP self-assembly,[78,79] but square-symmetry patterns are not easy to obtain from BCP self-assembly. Instead of using just one BCP, BCP blends were used. In an example of this shown in Figure 1.16, square patterns of polyferrocenylsilane (PFS) were achieved using a polyisoprene-blockpolystyrene-*block*-polyferrocenylsilane (PI-*b*-PS-*b*-PFS) triblock terpolymer blended with 15% PS homopolymer. Oxygen plasma was used to remove the PI and PS when the phase-separation was completed in the BCP thin film.

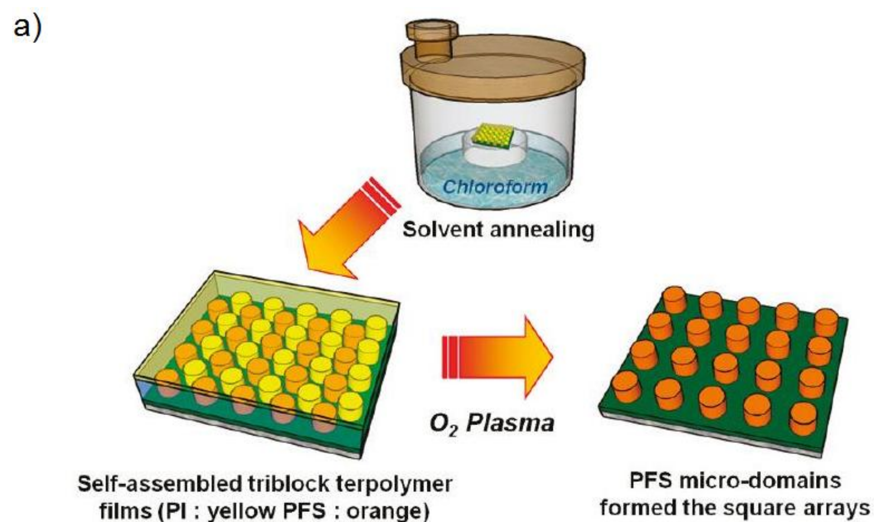

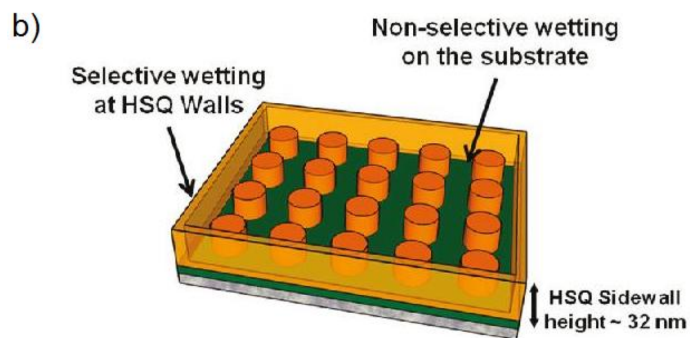

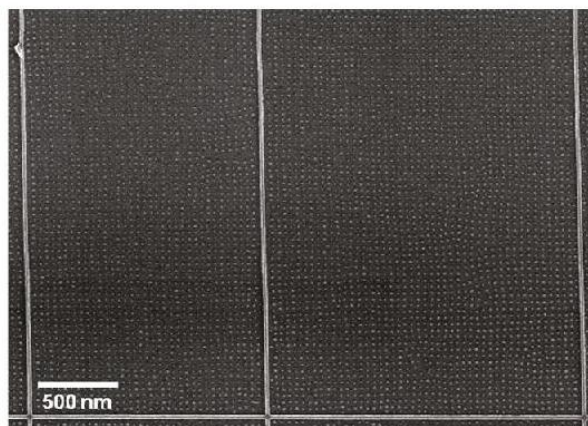

Figure 1.16. (a) Schematic presentation of the preparation of square packed perpendicular BCP cylinders using solvent annealing. (b) Schematic and SEM images of graphoepitaxy confined, highly ordered square arrays. Reprinted with permission from ref. 48. Copyright © 2011 American Chemical Society.

BCP self-assembly also provides a means to pattern the essential set of pattern geometries that are required for the semiconductor industry. Nealey and coworkers successfully used chemically "pre-patterned surfaces" (the surface which was patterned using lithography before the addition of BCPs to provide strong thermodynamic driving forces for BCP self-assembly) to direct the domain structures of PS-*b*-PMMA BCPs into a variety of structures such as jogs and T-junctions (Figure 1.17).[80] The PS domains are displayed in light gray, while the PMMA domains are dark gray in the SEM images. These structures that were obtained from self-assembled BCPs demonstrated the possibility that block copolymer materials, with their intrinsically advantageous self-assembling properties, may be amenable for broad applications in advanced lithography, including device layouts used in existing nanomanufacturing processes.[80]

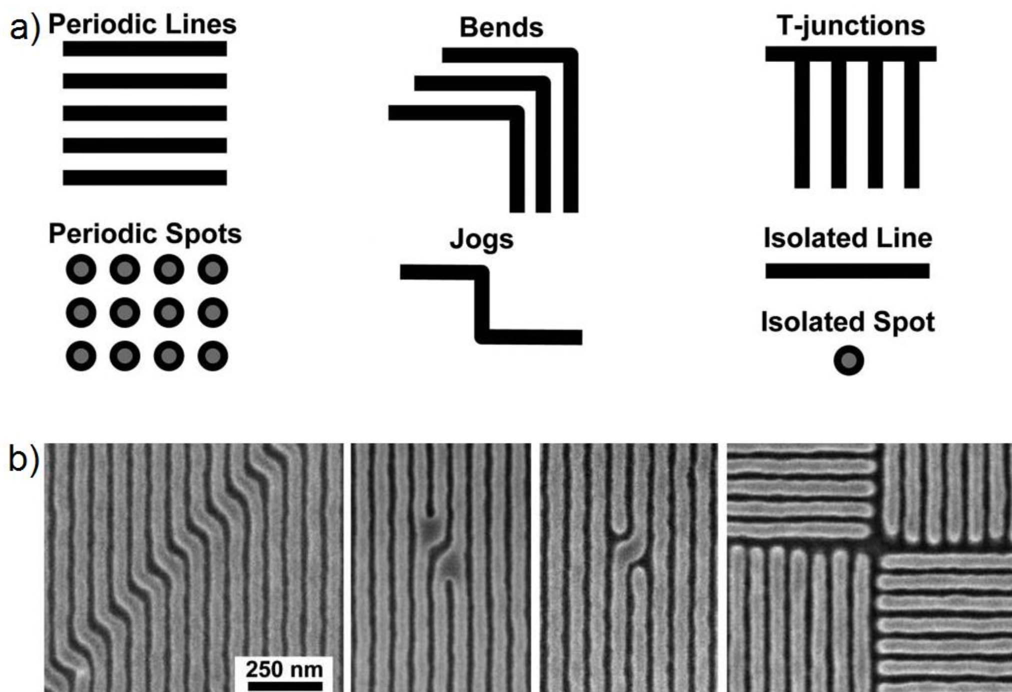

Figure 1.17. (a) Geometries required for fabricating most integrated circuits. (defined by the Semiconductor Industry Association's member companies) (b) SEM images of the directed self-assembled polymer structures. Reprinted with permission from ref. 50. Copyright © 2007 American Chemical Society.

1.5. Scope of the Thesis

This thesis presents BCP lithography from three perspectives: (1) reducing the self-assembly speed and defect density of BCPs; (2) controlling the feature spacing in BCP self-assembly; and (3) using block copolymer templates to fabricate nano-scale structures.

Chapter 2 starts with an introduction to BCPs and conventional BCP annealing techniques that are used to achieve BCP self-assembly. A new microwave-based solvothermal annealing approach is discussed. A study of the annealing time, annealing temperature, solvent, and substrate effects in the

microwave system is presented. After synthesis, the self-assembled BCP nanostructures were metallized with Pt for better visualization by SEM. The SEM images of the Pt nanostructures templated by self-assembled BCPs were then analyzed to obtain the defect density of each pattern.

A microwave annealing technique in a conventional household microwave oven is presented in Chapter 3. Low-defect nanostructures were obtained in the $100 oven within 60 s. Furthermore, using binary PS-*b*-P2VP/PS-*b*-P4VP BCP blends to create hybrid dot/line nanostructures as well as using binary PS-*b*-P2VP/PS-*b*-P2VP BCP blends to achieve fine control over linear feature spacings are discussed.

Chapter 4 describes a simple approach to pattern titania nanostructures, in which BCP thin films are used as the template, and hexagonally packed PS-*b*-P4VP micelles, deposited on a silicon substrate, are then etched by HF. Because of the PS-*b*-P4VP mask, an etch pit array was fabricated on the surface. Titania nanobowls were deposited inside the etched pits by $TiCl_4$ hydrolysis, and gold nanoparticles were deposited on the titania nanobowls. Chapters 2, 3, and 4, which represent collaborative work carried out by the author, were reproduced in part with permission from: (1) Zhang, X.; Harris, K. D.; Wu, N. L. Y. Murphy, J. N.; Buriak, J. M. *ACS Nano* **2010**, *4*, 7021-7029. Copyright © 2010 American Chemical Society. (2) Zhang, X.; Murphy, J. N.; Wu, N. L. Y.; Harris, K. D.; Buriak, J. M. *Macromolecules* **2011**, *Accepted*. Copyright © 2011 American Chemical Society. (3) Zhang, X. Qiao, Y. Xu, L.; Buriak, J. M. *ACS Nano* **2011**, *5*, 5015-5024. Copyright © 2011 American Chemical Society.

Finally, Chapter 5 presents a summary of each chapter and the outlook for this thesis work.

1.6. References

(1) Harriott, L. R. *Proc. IEEE* **2001**, *89*, 366-374.

(2) *International Technology Roadmap for Semiconductors, 2009 Edition*; Semiconductor Industry Association: San Jose, CA, 2009.

(3) de Diaz, S. L. .; Fowler, J. W.; Pfund, M. E.; Mackulak, G. T.; Hickie, M. *IEEE Trans. Semi. Manu.* **2005**, *18*, 622- 632.

(4) Black, C. T.; Bezencenet, O. *IEEE Trans. Nanotech.* **2004**, *3*, 412- 415.

(5) Black, C. T. *ACS Nano* **2007**, *1*, 147-150.

(6) Kim, H.-C.; Rettner, C. T.; Sundström, L. *Nanotechnology* **2008**, *19*, 235301.

(7) Brunner, T. A. *J. Vac. Sci. Technol. B* **2003**, *21*, 2632-2637.

(8) *http://en.wikipedia.org/wiki/Printing*.

(9) *http://en.wikipedia.org/wiki/Lithography*.

(10) Carter, K. R. *ACS Nano* **2010**, *4*, 595-598.

(11) Dill, F. H. *IEEE Trans. Electron Dev.* **1975**, *22*, 440- 444.

(12) Schmid, H.; Biebuyck, H.; Michel, B.; Martin, O. J. F. *Appl. Phys. Lett.* **1998**, *72*, 2379-2381.

(13) Levenson, M. D.; Viswanathan, N. S.; Simpson, R. A. *IEEE Trans. Electron Dev.* **1982**, *29*, 1828- 1836.

(14) Thompson, L. F.; Kerwin, R. E. *Annu. Rev. Mater. Sci.* **1976**, *6*, 267-301.

(15) Xia, Y.; Whitesides, G. M. *Annu. Rev. Mater. Sci.* **1998**, *28*, 153-184.

(16) Whitesides, G. M.; Ostuni, E.; Takayama, S.; Jiang, X.; Ingber, D. E. *Annu. Rev. Biomed. Eng*. **2001**, *3*, 335-373.

(17) Ito, T.; Okazaki, S. *Nature* **2000**, *406*, 1027-1031.

(18) Haq, E. ul; Liu, Z.; Zhang, Y.; Ahmad, S. A. A.; Wong, L.-S.; Armes, S. P.; Hobbs, J. K.; Leggett, G. J.; Micklefield, J.; Roberts, C. J.; Weaver, J. M. R. *Nano Lett.* **2010**, *10*, 4375-4380.

(19) Vieu, C.; Carcenac, F.; Pépin, A.; Chen, Y.; Mejias, M.; Lebib, A.; Manin-Ferlazzo, L.; Couraud, L.; Launois, H. *Appl. Surf. Sci.* **2000**, *164*, 111-117.

(20) *http://en.wikipedia.org/wiki/Electron_beam_lithography*.

(21) Rastogi, A.; Paik, M. Y.; Tanaka, M.; Ober, C. K. *ACS Nano* **2010**, *4*, 771-780.

(22) Chou, S.; Krauss, P.; Renstrom, P. *J. Vac. Sci. Technol. B* **1996**, *14*, 4129-4133.

(23) Park, H. J.; Kang, M.-G.; Guo, L. J. *ACS Nano* **2009**, *3*, 2601-2608.

(24) Jung, G.-Y.; Johnston-Halperin, E.; Wu, W.; Yu, Z.; Wang, S.-Y.; Tong, W. M.; Li, Z.; Green, J. E.; Sheriff, B. A.; Boukai, A.; Bunimovich, Y.; Heath, J. R.; Williams, R. S. *Nano Lett.* **2006**, *6*, 351-354.

(25) Mårtensson, T.; Carlberg, P.; Borgström, M.; Montelius, L.; Seifert, W.; Samuelson, L. *Nano Lett.* **2004**, *4*, 699-702.

(26) McAlpine, M. C.; Friedman, R. S.; Lieber, C. M. *Nano Lett.* **2003**, *3*, 443-445.

(27) Mei, P.; Jackson, W. B.; Taussig, C. P.; Jeans, A. **2006**, U. S. Patent No. 7056834 B2.

(28) Jackson, W. B.; Perlov, C.; Amanza-Workman, M.; Braymen, S.; Chaiken, A.; Jeffrey, F.; Hauschildt, J.; Jeans, A.; Kwon, O.; Luo, H.; Mei, P.; Taussig, C. *2007 Digest of the IEEE/LEOS Summer Topical Meetings* **2007**, 125-126.

(29) Broers, A. N. *IBM J. Res. & Dev.* **1988**, *32*, 502-513.

(30) Bang, J.; Jeong, U.; Ryu, D. Y.; Russell, T. P.; Hawker, C. J. *Adv. Mater.* **2009**, *21*, 4769-4792.

(31) Black, C. T.; Ruiz, R.; Breyta, G.; Cheng, J. Y.; Colburn, M. E.; Guarini, K. W.; Kim, H.-C.; Zhang, Y. *IBM J. Res. Dev.* **2007**, *51*, 605-633.

(32) Whitesides, G. M.; Grzybowski, B. *Science* **2002**, *295*, 2418-2421.

(33) Black, C. T.; Guarini, K. W.; Milkove, K. R.; Baker, S. M.; Russell, T. P.; Tuominen, M. T. *Appl. Phys. Lett.* **2001**, *79*, 409-411.

(34) Stoykovich, M. P.; Nealey, P. F. *Mater. Today* **2006**, *9*, 20-29.

(35) Cheng, J. Y.; Ross, C. A.; Smith, H. I.; Thomas, E. L. *Adv. Mater.* **2006**, *18*, 2505-2521.

(36) Schwartz, E. L.; Bosworth, J. K.; Paik, M. Y.; Ober, C. K. In *Advances in Resist Materials and Processing Technology XXVII*; Allen, R. D., Ed.; SPIE: San Jose, California, USA, 2010; Vol. 7639, p. 76390G-11.

(37) Bates, F. S.; Fredrickson, G. H. *Phys. Today* **1999**, *52*, 32-38.

(38) Park, M.; Harrison, C.; Chaikin, P. M.; Register, R. A.; Adamson, D. H. *Science* **1997**, *276*, 1401-1404.

(39) Park, S.; Lee, D. H.; Xu, J.; Kim, B.; Hong, S. W.; Jeong, U.; Xu, T.; Russell, T. P. *Science* **2009**, *323*, 1030-1033.

(40) Mansky, P.; haikin, P.; Thomas, E. L. *J. Mater. Sci* **1995**, *30*, 1987-1992.

(41) Jung, Y. S.; Chang, J. B.; Verploegen, E.; Berggren, K. K.; Ross, C. A. *Nano Lett.* **2010**, *10*, 1000-1005.

(42) Stuen, K. O.; Thomas, C. S.; Liu, G.; Ferrier, N.; Nealey, P. F. *Macromolecules* **2009**, *42*, 5139.

(43) Detcheverry, F. A.; Nealey, P. F.; de Pablo, J. J. *Macromolecules* **2010**, *43*, 6495-6504.

(44) Cheng, J. Y.; Sanders, D. P.; Truong, H. D.; Harrer, S.; Friz, A.; Holmes, S.; Colburn, M.; Hinsberg, W. D. *ACS Nano* **2010**, *4*, 4815-4823.

(45) Kwon, S.; Yan, X.; Contreras, A. M.; Liddle, J. A.; Somorjai, G. A.; Bokor, J. *Nano Lett.* **2005**, *5*, 2557-2562.

(46) Ruiz, R.; Dobisz, E.; Albrecht, T. R. *ACS Nano* **2011**, *5*, 79-84.

(47) Bita, I.; Yang, J. K. W.; Jung, Y. S.; Ross, C. A.; Thomas, E. L.; Berggren, K. K. *Science* **2008**, *321*, 939 -943.

(48) Segalman, R. A.; Hexemer, A.; Kramer, E. J. *Macromolecules* **2003**, *36*, 6831-6839.

(49) Segalman, R. A.; Yokoyama, H.; Kramer, E. J. *Adv. Mater.* **2001**, *13*, 1152-1155.

(50) Chuang, V. P.; Cheng, J. Y.; Savas, T. A.; Ross, C. A. *Nano Lett.* **2006**, *6*, 2332-2337.

(51) Ouk Kim, S.; Solak, H. H.; Stoykovich, M. P.; Ferrier, N. J.; de Pablo, J. J.; Nealey, P. F. *Nature* **2003**, *424*, 411-414.

(52) Boltau, M.; Walheim, S.; Mlynek, J.; Krausch, G.; Steiner, U. *Nature* **1998**, *391*, 877-879.

(53) Ruiz, R.; Kang, H.; Detcheverry, F. A.; Dobisz, E.; Kercher, D. S.; Albrecht, T. R.; de Pablo, J. J.; Nealey, P. F. *Science* **2008**, *321*, 936-939.

(54) Edwards, E. W.; Müller, M.; Stoykovich, M. P.; Solak, H. H.; de Pablo, J. J.; Nealey, P. F. *Macromolecules* **2007**, *40*, 90-96.

(55) Edwards, E. W.; Montague, M. F.; Solak, H. H.; Hawker, C. J.; Nealey, P. F. *Adv. Mater.* **2004**, *16*, 1315-1319.

(56) Jeong, S.-J.; Moon, H.-S.; Kim, B. H.; Kim, J. Y.; Yu, J.; Lee, S.; Lee, M. G.; Choi, H.; Kim, S. O. *ACS Nano* **2010**, *4*, 5181-5186.

(57) Bang, J.; Kim, S. H.; Drockenmuller, E.; Misner, M. J.; Russell, T. P.; Hawker, C. J. *J. Am. Chem. Soc.* **2006**, *128*, 7622-7629.

(58) Hong, A. J.; Liu, C.-C.; Wang, Y.; Kim, J.; Xiu, F.; Ji, S.; Zou, J.; Nealey, P. F.; Wang, K. L. *Nano Lett.* **2010**, *10*, 224-229.

(59) Verbakel, F.; Meskers, S. C. J.; Janssen, R. A. J. *Chem. Mater.* **2006**, *18*, 2707-2712.

(60) Yoon, J.; Lee, W.; Thomas, E. L. *Nano Lett.* **2006**, *6*, 2211-2214.

(61) Discher, D. E.; Eisenberg, A. *Science* **2002**, *297*, 967 -973.

(62) Kataoka, K.; Harada, A.; Nagasaki, Y. *Adv. Drug Deliv. Rev.* **2001**, *47*, 113-131.

(63) Meiners, J. C.; Elbs, H.; Ritzi, A.; Mlynek, J.; Krausch, G. *J. Appl. Phys.* **1996**, *80*, 2224.

(64) Park, J. H.; Sun, Y.; Goldman, Y. E.; Composto, R. J. *Langmuir* **2010**, *26*, 10961-10967.

(65) Arnold, M.; Cavalcanti - Adam, E. A.; Glass, R.; Blümmel, J.; Eck, W.; Kantlehner, M.; Kessler, H.; Spatz, J. P. *ChemPhysChem* **2004**, *5*, 383-388.

(66) Glass, R.; M ller, M.; Spatz, J. P. *Nanotechnology* **2003**, *14*, 1153-1160.

(67) Zehner, R. W.; Lopes, W. A.; Morkved, T. L.; Jaeger, H.; Sita, L. R. *Langmuir* **1998**, *14*, 241-244.

(68) Bronstein, L.; Chernyshov, D.; Valetsky, P.; Tkachenko, N.; Lemmetyinen, H.; Hartmann, J.; Förster, S. *Langmuir* **1999**, *15*, 83-91.

(69) Jung, Y. S.; Lee, J. H.; Lee, J. Y.; Ross, C. A. *Nano Lett.* **2010**, *10*, 3722-3726.

(70) Chen, J.; Mela, P.; Möller, M.; Lensen, M. C. *ACS Nano* **2009**, *3*, 1451-1456.

(71) Black, C. T. *Appl. Phys. Lett.* **2005**, *87*, 163116.

(72) Segalman, R. A. *Materials Science and Engineering: R: Reports* **2005**, *48*, 191-226.

(73) Warren, S. C.; Messina, L. C.; Slaughter, L. S.; Kamperman, M.; Zhou, Q.; Gruner, S. M.; DiSalvo, F. J.; Wiesner, U. *Science* **2008**, *320*, 1748-1752.

(74) Stoykovich, M. P.; Muller, M.; Kim, S. O.; Solak, H. H.; Edwards, E. W.; de Pablo, J. J.; Nealey, P. F. *Science* **2005**, *308*, 1442-1446.

(75) Black, C.; Guarini, K.; Zhang, Y.; Kim, H.; Benedict, J.; Sikorski, E.; Babich, I.; Milkove, K. *IEEE Electron Device Lett.* **2004**, *25*, 622-624.

(76) Hamm, S. *Business Week* **2007**, IBM's Chip Breakthrough.

(77) Hamley, I. W. *Nanotechnology* **2003**, *14*, R39-R54.

(78) Tang, C.; Lennon, E. M.; Fredrickson, G. H.; Kramer, E. J.; Hawker, C. J. *Science* **2008**, *322*, 429-432.

(79) Son, J. G.; Gwyther, J.; Chang, J.-B.; Berggren, K. K.; Manners, I.; Ross, C. A. *Nano Lett.* **2011**, *11*, 2849-2855.

(80) Stoykovich, M. P.; Kang, H.; Daoulas, K. C.; Liu, G.; Liu, C.-C.; de Pablo, J. J.; Müller, M.; Nealey, P. F. *ACS Nano* **2007**, *1*, 168-175.

Chapter 2
Fast BCP Self-Assembly Achieved by Solvent-Assisted Microwave Annealing

In this work, the e-beam lithographical features were fabricated by Nathanael Wu; the defect densities quantification was carried out by Jeffrey Murphy; Figure 2.6 (b) and Figure 2.9 were drawn by Dr. Kenneth Harris. Dr. Harris, Jeffrey Murphy, and Nathanael Wu all contributed to useful discussions.

Self-assembling materials are the building blocks of polymer lithography for bottom-up fabrication processes. This chapter describes a rapid BCP ordering technique that we developed over the past two years.[1] As briefly mentioned in the previous chapter, solvent annealing and thermal annealing are the two conventional means to achieve dimensional uniformity and organization of BCP thin film templates. In most cases, traditional self-assembling approaches based on solvent annealing and thermal annealing are very time-consuming and therefore are not suitable to be used on a commercial basis. The quick and efficient annealing of self-assembling BCP materials is a major challenge. In order to decrease the annealing time, we investigated the use of microwaves as a simple way to anneal BCPs. In this thesis work, a solvent-assisted thermal annealing approach that uses microwave heating as a fast annealing technique is described. The structure and orientation of the self-assembled BCPs are controlled by the annealing temperature, substrate conductivity and topographical patterns. This method, which leads to the fabrication of well-ordered BCP

domains with long-range order, is expected to be useful in commercial BCP lithography applications.

2.1. Introduction

Block Copolymers (BCPs)

BCPs, in this case, refer to polymer chains assembled from two or more monomer types that are spatially linked end-to-end through covalent bonds and grouped into blocks. Figure 2.1 (a), shows the simplest type of BCP, an AB type diblock copolymer which contains two distinct homopolymer units, A and B. When the two components, A and B, are immiscible, the diblock copolymer can spontaneously form ordered nanostructures, such as spheres, cylinders, gyroids and lamellae, because the covalent linkage between the two blocks prevents phase segregation.[2–17] BCP lithography makes use of the chemical phase segregation of BCPs to spontaneously generate organized patterns across a substrate. Figure 2.1 (b), shows two examples of the fingerprint-like cylindrical nanostructures generated by self-assembled poly(styrene)-*block*-poly(2-vinylpyridine) (PS-*b*-P2VP) and poly(styrene)-*block*-poly(methyl methacrylate) (PS-*b*-PMMA) BCPs.

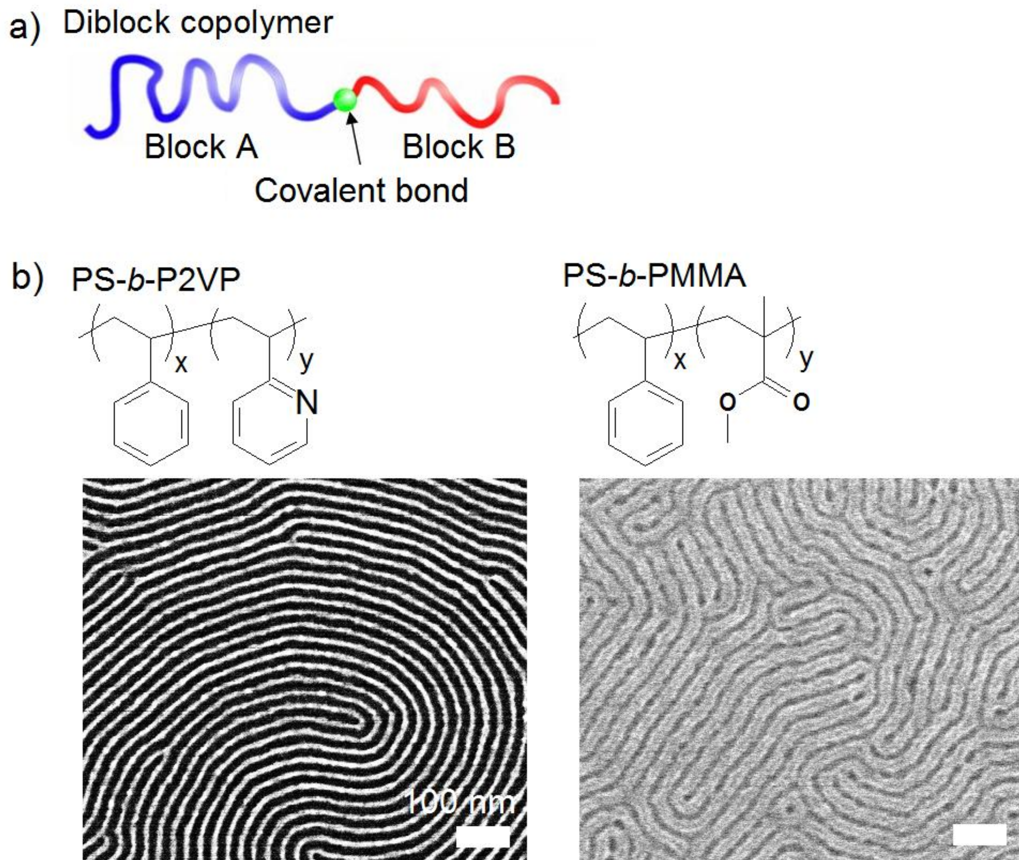

Figure 2.1. (a) Generalized structure of an AB diblock copolymer. (b) Chemical structures of the PS-*b*-P2VP and PS-*b*-PMMA block copolymers used in this study and SEM images of the nanostructures generated using self-assembled PS-*b*-P2VP and PS-*b*-PMMA block copolymers as the platform.

BCP Annealing Techniques

BCPs are generally cast from solution to form thin films on substrates, and in most cases, the BCP film initially forms a kinetically frozen non-equilibrium structure. Following the film deposition, there is usually an annealing step which uses external stimuli, such as thermal energy and solvent vapor, to achieve or accelerate equilibrium and modulate the resulting ordered structures. The two most important conventional annealing methods are thermal annealing and solvent

annealing (Figure 2.2). In thermal annealing, the mobility of the BCPs is increased by holding the samples at a temperature above the glass transition (T_g) temperature. In the solvent annealing, the BCPs are held under a controlled saturated solvent vapor atmosphere and the mobility of the BCPs is increased as the film absorbs solvent from the vapor phase. The solvent plasticizes the blocks and reduces the glass transition temperature of the BCPs below ambient temperature, allowing the BCP nanostructure to relax into a lower energy orientation.[18] During annealing, efforts can also be made to control the orientation of the phase-separated domains. With different strategies, such as using chemically pre-patterned substrates, graphoepitaxy, electric fields, shear, or temperature gradients, scientists can now control and manipulate the assembly of BCP domains in thin films over a very long range.[19–23]

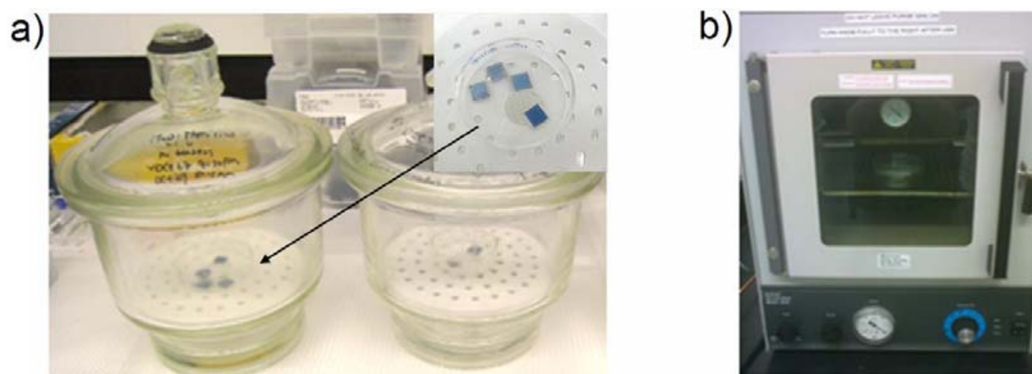

Figure 2.2. Pictures of conventional annealing methods. (a) Solvent annealing in desiccators. (b) Thermal annealing in a vacuum oven.

BCP Self-Assembly Speed

One design issue that is rarely addressed in BCP self-assembly is the assembly speed. The Semiconductor Industry Association ITRS roadmap 2007 stipulates that "***the net time required to form and fix a pattern must be short, less than 4 minutes***", yet few publications address this issue.[24] Nealey and coworkers recently showed that fast BCP (PS-*b*-PMMA) self-assembly could occur at high temperatures (above 200 ^{o}C) in minutes. These examples of rapid self-assembly were achieved on chemically prepatterned substrates, but not on flat, unpatterned surfaces (Figure 2.3).[25] In most other cases, the annealing step takes hours or even days.[26] In this chapter, we demonstrate a solvent-assisted microwave annealing approach that is capable of rapidly generating organized BCP patterns in minutes. The rapid BCP assembly can be achieved by using a commercial microwave reactor as the heating source. The work in this chapter describes the effects of a wide range of processing conditions on the quality and assembly speed of these microwave-annealed patterns.

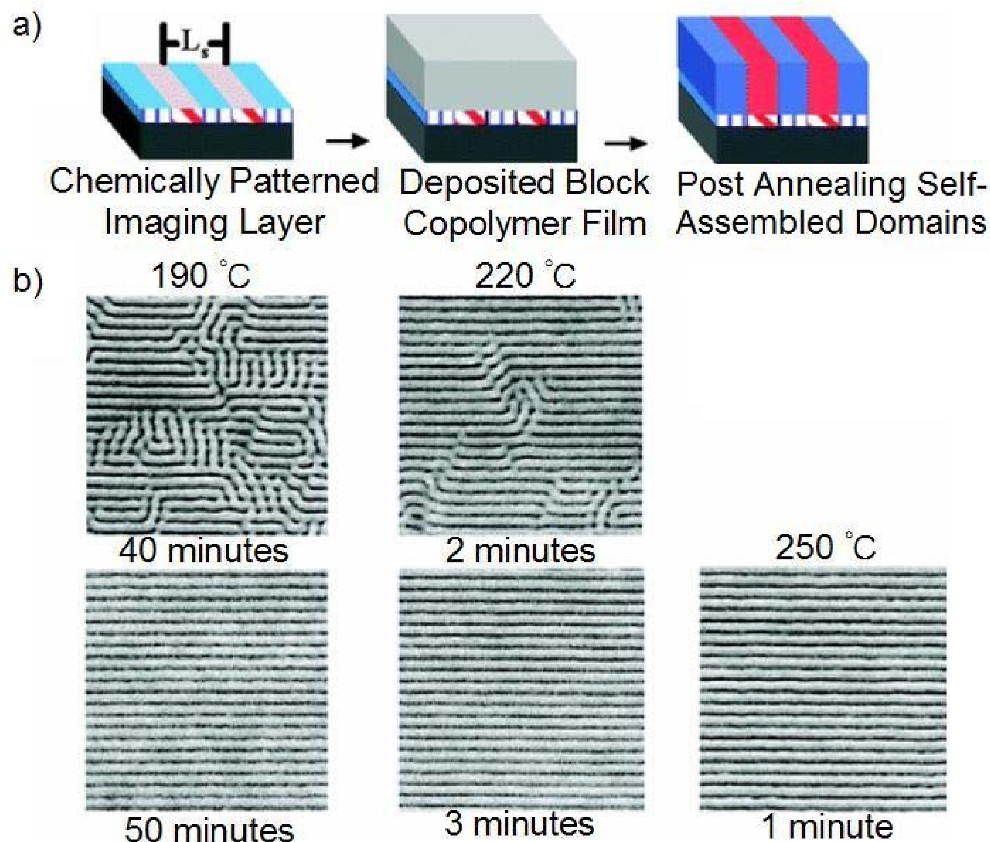

Figure 2.3. (a) Outline of BCP directed self-assembly using chemical pre-patterning. (b) SEM images of the directed assembly of PS-*b*-PMMA on chemically patterned surfaces at various annealing times and temperatures. All micrographs are 1 μm × 1 μm. Reprinted with permission from ref. 25. Copyright © 2008 American Chemical Society.

2.2. Results and Discussions

BCP Thin Films

The amphiphilic diblock copolymers used here were PS-*b*-P2VP and PS-*b*-PMMA, with molecular weights (g/mol) of PS-*b*-P2VP = 23600-*b*-10400, 32500-*b*-12000, 44000-*b*-18500, 50000-*b*-16500, and PS-*b*-PMMA = 45000-*b*-20000. In order to prepare the BCP thin films on flat silicon substrates (Figure 2.4), the BCPs were weighed and dissolved in neat toluene at room temperature by stirring

overnight to make a 1% w/w solution of polymer micelles. The BCP micelles were transferred to the selected silicon substrate by spin-casting of the BCP solution at 4200 rpm for 50 s under an argon environment. The spherical polymer micelles formed a pseudo-hexagonally packed pattern with PVP and PMMA cores surrounded by a PS matrix (Figure 2.5). The conditions for making a BCP thin film were adopted from the previously established procedures in the Buriak group to make a single layer of BCP micelles.[2]

Figure 2.4. Picture of block copolymer thin film-coated silicon substrates. The silicon substrates are 1 cm by 1 cm in size.

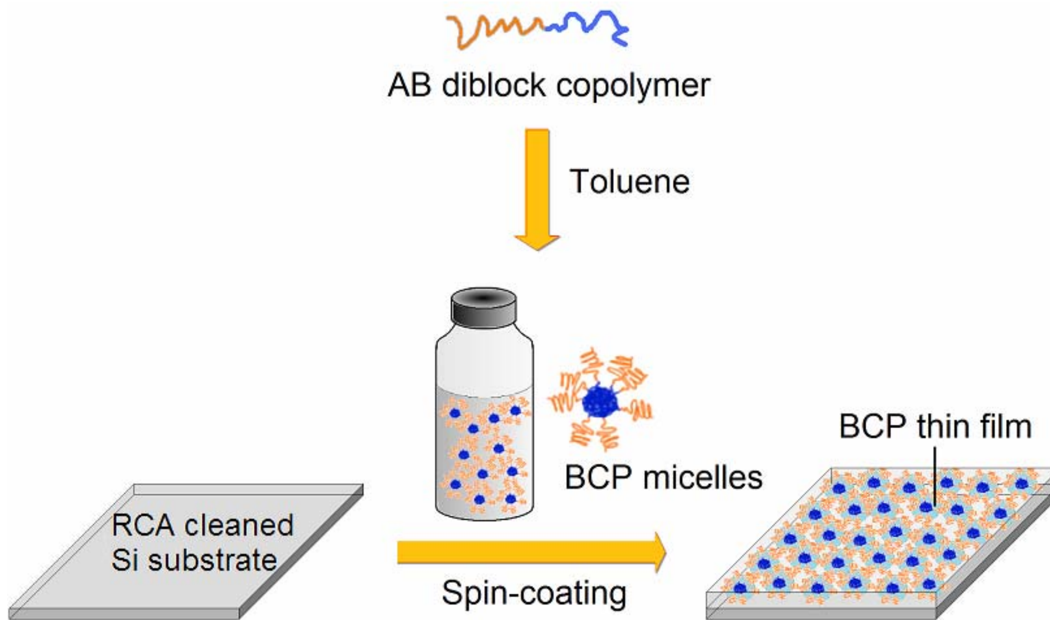

Figure 2.5. Outline for block copolymer thin film preparation. Diblock copolymer is first dissolved in toluene and the solution is then spin-coated onto a flat silicon substrate to make a BCP thin film.

Microwave Annealing

Figure 2.6 (b) illustrates the basic experimental strategy that we used to prepare ordered BCP films on silicon surfaces. First, a BCP film, PS-*b*-P2VP or PS-*b*-PMMA [molecular structures are shown in Figure 2.1 (b)], was spin-coated on a cleaned silicon substrate with a self-assembled quasi-ordered hexagonal pattern.

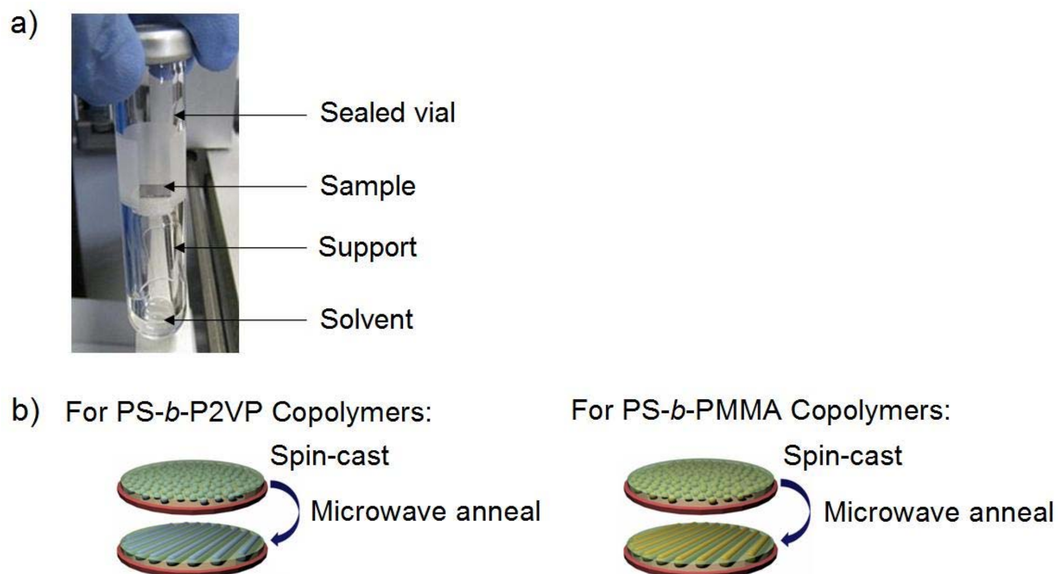

Figure 2.6. (a) Picture of the microwave annealing reaction tube. (b) Schematics of experimental approaches of microwave annealing with PS-*b*-P2VP and PS-*b*-PMMA BCPs. Reprinted with permission from ref. 1. Copyright © 2010 American Chemical Society.

The SEM images of nanostructures observed for unannealed BCPs [shown in Figure 2.7, (a)-(d)] are quasi-hexagonal patterns of Pt nanostructures that were templated from PS-*b*-P2VP (23.6k-*b*-10.4k), (32.5k-*b*-12k), (44k-*b*-18.5k), and (50k-*b*-16.5k), respectively. Figures (e) and (f) show the nanostructure of unannealed PS-*b*-PMMA (45k-*b*-20k). Figure (f) is the quality-enhanced image of (e). A Biotage Initiator 2.5 system (Figure 2.8), which provides high powered and focused microwave heating, was used as the microwave source to anneal the polymer film. Inside the sample tube, a microwave-safe glass support was built to hold the silicon shard above the solvent [Figure 2.6 (a)]. The tube was then sealed and placed inside the reaction chamber of the Initiator. The microwave-induced

heating transformed the BCP dot array pattern in a very short time to a fingerprint pattern that has cylindrical domains of P2VP/PMMA surrounded by a PS matrix. Solvent annealing and thermal annealing are commonly used to control the orientation of BCP systems by increasing the mobility in BCP films through partial solubilization and bringing to the glass transition state,[26] respectively. Solvothermal microwave irradiation combines the two - it brings the BCP films near or above the glass transition temperature (T_g) and simultaneously plasticizes the BCP films in a saturated solvent vapor. Thus, a rapid assembly of the BCP becomes possible. Microwave irradiation of polar systems provides a non-contact, rapid heating strategy. It has been reported by Kappe and coworkers that the microwave-assisted heating is the result of a purely thermal process that the strongly microwave-absorbing ceramic material SiC can be used to achieve fast passive heating.[27,28] Silicon is a fairly good microwave absorber;[29,30] it also has good thermal conductivity that allows it to be used as a heating medium to transfer the heat to the spin-coated polymers in the microwave annealing.[31]

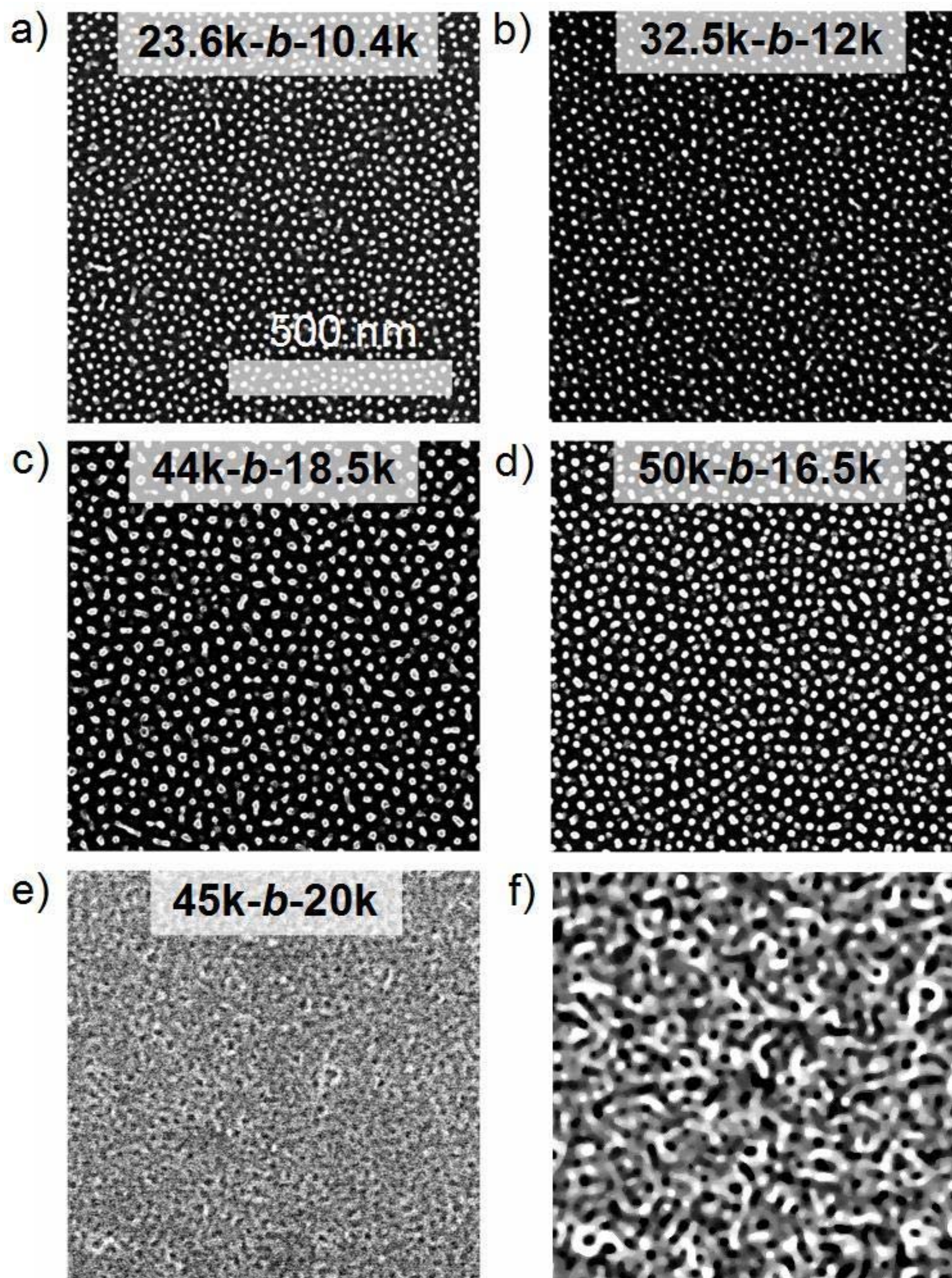

Figure 2.7. SEM images showing nanostructures observed for unannealed BCPs. Reprinted with permission from ref. 1. Copyright © 2010 American Chemical Society.

Figure 2.8. Photograph of Biotage Initiator 2.5 microwave system.

Fabrication of Metallic Nanopatterns on Silicon Substrates

One means by which the organized BCP films can be transferred into metallic nanopatterns is a metallization treatment (Figure 2.9) that also improves the visualization by scanning electron microscopy. Different metals can be deposited, but platinum was used in the work reported in this chapter.[2,32] In brief, the organized BCP films were treated with aqueous Na_2PtCl_4 in the presence of HCl (aq). HCl enables protonation of the basic P2VP block, encouraging the formation of stable $PtCl_4^{2-}$ / P2VP complexes through electrostatic interactions. Oxygen plasma was subsequently used to remove the polymer and simultaneously reduce $PtCl_4^{2-}$ ions to platinum metal. The structure of the metallic platinum nanolines after plasma cleaning was imaged using scanning electron microscopy.

The quality of the metallic nanostructures is dependent on the metallization conditions such as the metal salt concentration, the soaking time, and the plasma conditions.[2]

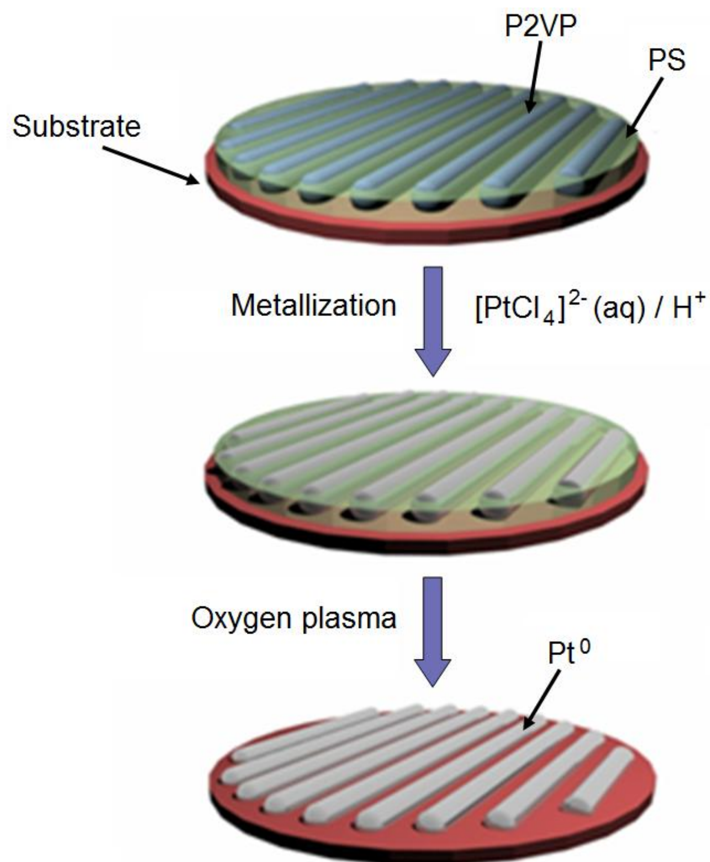

Figure 2.9. Schematic representation of metal deposition process. The PS-*b*-P2VP BCP is first loaded with $[PtCl_4]^{2-}$ ions by soaking in an acidic solution, and oxygen plasma is then used to reduce the metal ions and remove the polymer.

Rapid Self-Assembly in Microwaves

With the help of the research microwave system, assemblies of BCPs were achieved in short periods of time on unpatterned substrates. In our standard

procedures, in which microwave power was held a target temperature for 5-60 s, long range ordering was achieved. This new method has high reproducibility since the temperature is precisely controlled by the microwave system. Figure 2.10 shows several examples of nanopatterns templated by microwave annealed BCP thin films. The annealing temperature holding time was 1 minute for all cases. Figure 2.10 (a) shows Pt nanolines that were templated from microwave annealed PS-*b*-P2VP (23.6k-*b*-10.4k) (130 °C, target hold time = 60 s) on an unpatterned Si(100) surface. Figure 2.10 (b) and (e) show Pt nanolines that were templated from microwave annealed PS-*b*-P2VP (23.6k-*b*-10.4k) (130 °C, target hold time = 60 s) on topologically patterned flat Si(100) surfaces. Figure 2.10 (c) and (d) are SEM images of BCP PS-*b*-PMMA (45k-*b*-20k) that was microwave annealed for 180 s at 180 °C on unpatterned and topologically patterned flat Si(100) surfaces, respectively. To image PS-*b*-PMMA in SEM, the BCPs were treated with oxygen plasma for 20 s. The dark and light regions were PMMA and PS domains, respectively.[33] The platinum and BCP nanoline structures shown in Figure 2.10 are parallel but not necessarily straight. These self-organizing BCP systems are balanced by organizing forces such as the chemical incompatibility of the two blocks and the intrinsic entropy. More organization requires an overall reduction in the system entropy, however, as resolution limits go lower, dealing with the intrinsic entropy of polymers is very hard.[34] For industrial applications, the device performance is ultimately affected by the line edge roughness (LER), and according to the ITRS roadmap, BCP self-assembly must be able to achieve <1.3 nm LER to be considered a viable and competitive patterning option.[24,35–39]

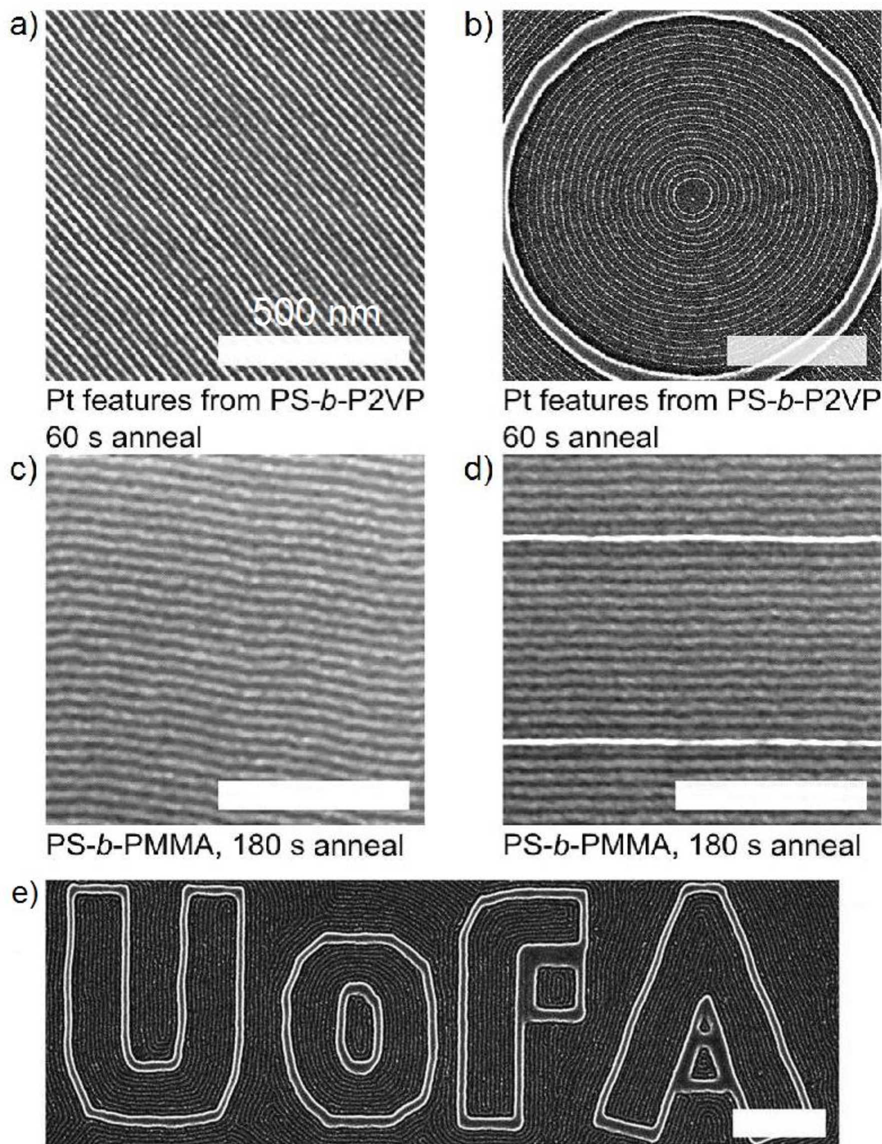

Figure 2.10. Platinum and BCP patterns prepared by microwave annealing. (a), (b), and (e) SEM images of Pt nanolines templated from 60 s microwave anneal using PS-*b*-P2VP (23.6k-*b*-10.4k). In (a), the substrate was unpatterned, and in (b), the substrate was flat silicon with EBL fabricated silica topological features. (c) and (d) SEM images of 180 s microwave annealed PS-*b*-PMMA (45k-*b*-20k) on (c) unpatterned silicon substrate and (d) flat silicon with two parallel silica lines. To image PS-*b*-PMMA BCPs, the samples were treated with oxygen plasma for 20 s. Reprinted with permission from ref. 1. Copyright © 2010 American Chemical Society.

Thermal Annealing

There are many key factors in the microwave annealing process that need to be studied carefully, such as the target temperature, the target temperature holding time, and the solvent used. Solvent-assisted microwave annealing combines thermal annealing and solvent annealing. However, we could not mimic solvent-assisted annealing using a traditional heating source, such as an oil bath - solvent condensation always took place on the substrates because the substrates were colder than the solvent vapor. As shown in Figure 2.11 (a), a vial which is identical to the microwave setup and contained the sample and the solvent THF was placed in an oil bath and heated at 130 ^{o}C for 60 s. Figure 2.11 (b) and (c) are pictures of BCP thin films taken before and after the control experiment.

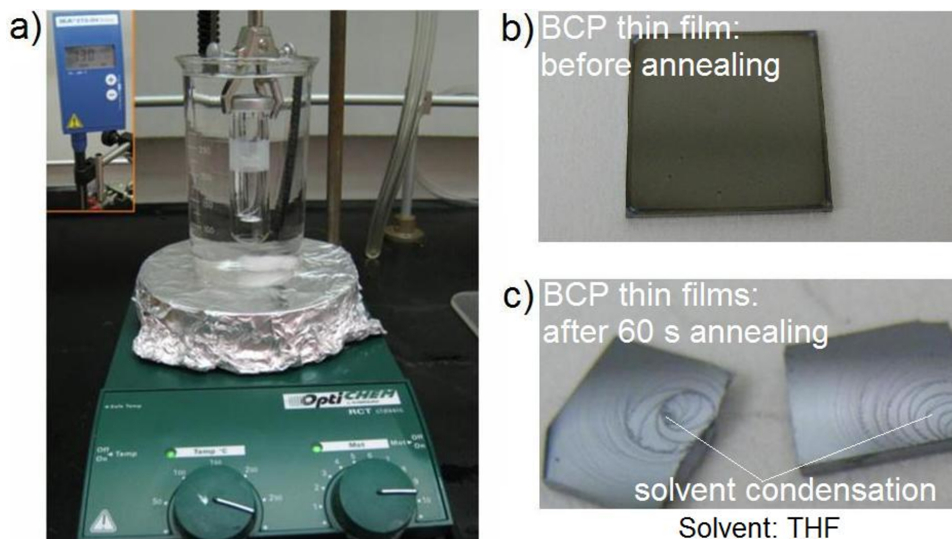

Figure 2.11. (a) Picture of experimental setup to mimic the solvent-assisted microwave annealing. (b) Picture of PS-*b*-P2VP (32.5k-*b*-12k) BCP sample before annealing. (c) Picture of BCP thin film samples after annealing. Reprinted with permission from ref. 1. Copyright © 2010 American Chemical Society

Effects of Time on Microwave Annealing

One feature of the microwave initiator is the precise control of temperature and time. In this study, a chosen target temperature and a target temperature holding time were always applied. The target temperature is the highest temperature of the reaction vial that is set, measured and controlled by the system in the microwave annealing process; it usually takes several seconds to several minutes for the initiator to achieve the target (if the temperature does not increase fast enough, the microwave will automatically shut down; the temperature increase of the Biotage system is 2-5 ^{o}C/second), depending on the given target, the amount of the solvent, and the type of solvent. In our study, the time used to achieve the target ranged from 15 s to about 2 minutes. Before the microwave shuts down, the target is held for a given time. Finally a cooling step was applied. The condensed air-cooling is controlled by the Initiator and depends upon the target temperature, the amount of solvent, and the solvent type. The cooling steps usually lasted 20 s to about 2 minutes. For polymers with small molecular weights, the time required to achieve the equilibrium structures can be very short, as shown in the SEM images of Figure 2.12. For example, in Figure 2.12 (a), the as cast "dots" structure converted into the cylindrical structure by holding PS-*b*-P2VP (23.6k-*b*-10.4k) at 130 ^{o}C for 5 s. As a result, the measured defect density was largely reduced. Figure 2.12 (f) shows plots of the evolution of defect density for various BCPs microwave annealed at 130 °C using THF as the solvent (note: the dotted lines between data points are used to facilitate discrimination between data sets and are not intended to convey any interpolated information).

For polymers with larger sizes, it takes longer to achieve the equilibrium structures. Holding the BCP PS-*b*-PMMA (45k-*b*-20k) at 130 ^{o}C for 180 s resulted in a much lower defect density of the structure [36 defect pairs/μm^2, given in Figure 2.12 (f)].

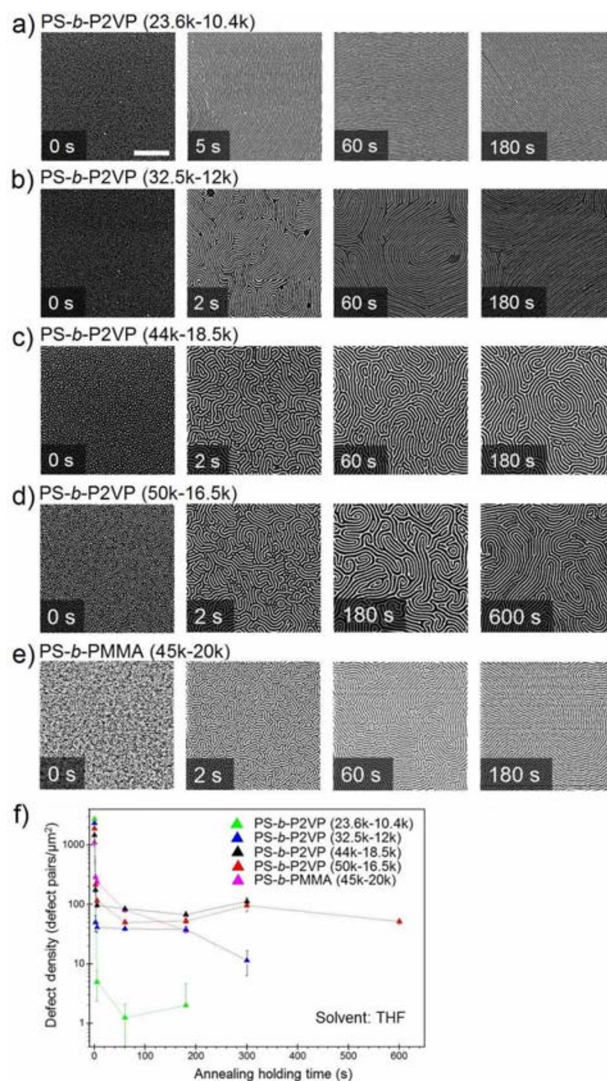

Figure 2.12. Influence of annealing time on BCP organization. (a)-(d) SEM images of Pt nanofeatures prepared from microwave annealed PS-*b*-P2VP BCPs. (e) SEM images of microwave annealed PS-*b*-PMMA (45k-*b*-20k). The first panel (0 s) in each series shows the BCP samples prior to annealing. Scale bar = 500 nm. Reprinted with permission from ref. 1. Copyright © 2010 American Chemical Society.

Effects of Temperature and Solvent on Microwave Annealing

Bringing the BCP film above the glass transition temperature or the use of solvent vapor increases the mobility by plasticizing the film.[11,40–42] In this study, three BCPs with average molecular weight (M_n) ranging from 34 kg/mol [PS-*b*-P2VP (23.6k-*b*-10.4k)] to 65 kg/mol [PS-*b*-PMMA (45k-*b*-20k)] were used to determine the transition from hexagonal arrays to cylindrical arrays during the microwave annealing process by probing the temperature and solvent effects. Figure 2.13 (a) and (b) are SEM images of Pt nanostructures templated by PS-*b*-P2VP (23.6k-*b*-10.4k) polymer structures formed after 60 s of THF-assisted and toluene-assisted microwave annealing, respectively, at different temperatures to show the influence of temperature and solvents. This BCP was chosen because it undergoes fast formation of the cylindrical structures and provides a complete picture of the transition, even when using very low microwave power. The SEM images of metallized PS-*b*-P2VP (32.5k-*b*-12k) and PS-*b*-PMMA (45k-*b*-20k) after 180 s of solvent-assisted microwave annealing are shown in Figure 2.14. The nanolines formed at a lower temperature in the presence of THF as opposed to toluene. In the case of THF, the size of the self-assembled fingerprint patterns could expand from less than 100 nm to several micrometers when the temperature used for annealing increased from 80 ^{o}C to 160 ^{o}C. Fingerprint patterns are already apparent at 80 ^{o}C. In a 1.5 μm by 1.5 μm frame, parallel nanolines were seen when the target temperature was higher than 140 ^{o}C. For comparison, Figure 2.13 (b) shows the results of the nanoline structures formed in the presence of toluene for the same BCP. With toluene, a higher temperature than with THF was

needed to obtain a similar size of fingerprint; i.e. parallel nanolines were seen in a 1.5 μm by 1.5 μm frame at 160 ^{o}C for toluene. This indicates that THF is a better solvent for microwave annealing since lower temperatures are sufficient. For both THF and toluene, higher energy microwave annealing lead to better polymer order. When isolated from the solvents, as shown in the control experiments [presented in Figure 2.13 (c), 2.14 (b) and (d)], less ordered patterns were attained when a BCP film was annealed (in the absence of any solvents). Figure 2.13 (f) shows plots of the evolution of density of defects for microwave annealed BCPs at different temperatures with and without solvents. Several observations can be made: (1) a higher microwave annealing temperature facilitates a thermodynamically driven reorganization; (2) effective solvents further encourage the organization of BCPs and samples annealed without a solvent tend to be much more disordered; and (3) larger BCPs require longer ordering times than the smaller ones.

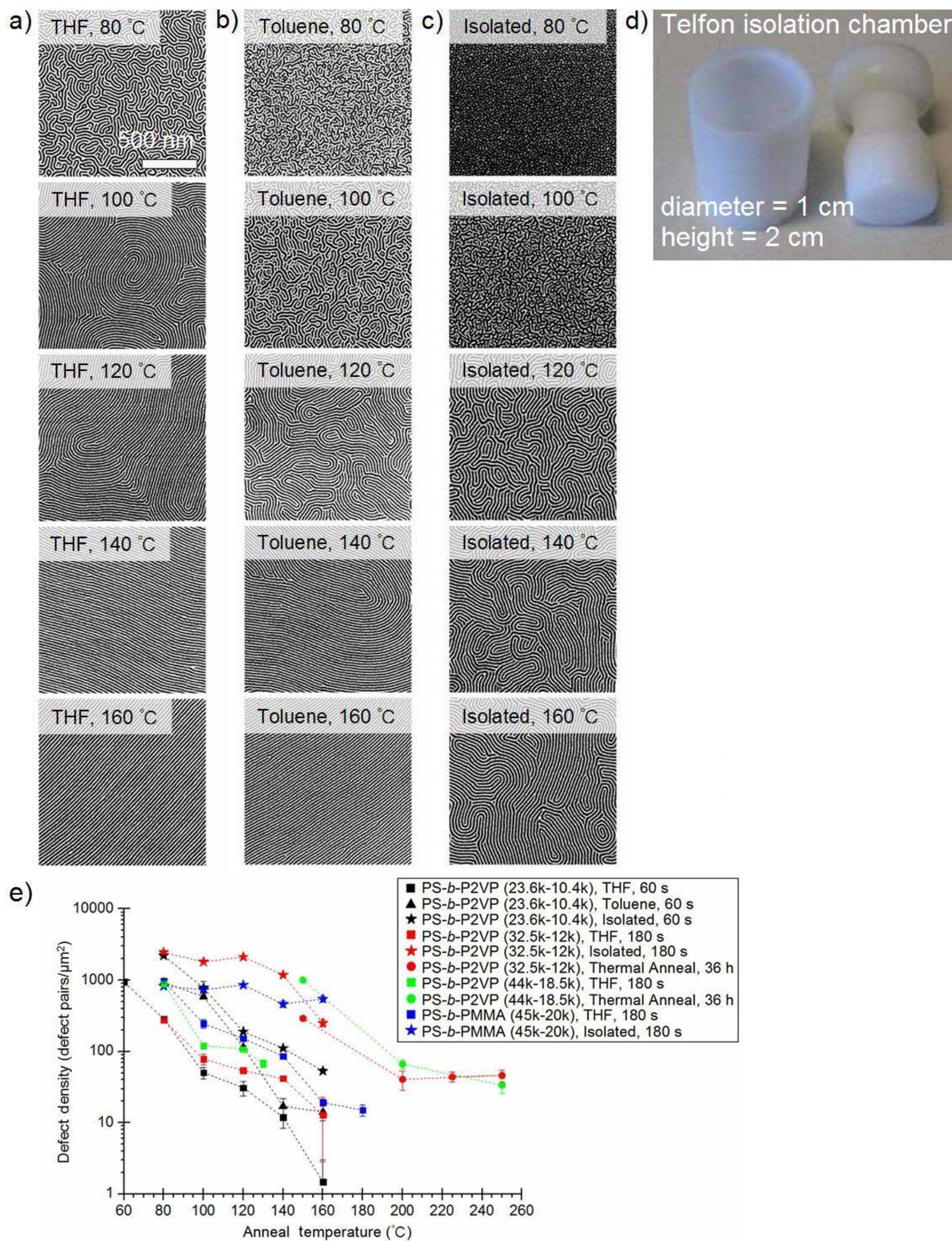

Figure 2.13. Studies to determine the effect of solvent and temperature. (a)-(c) SEM images of Pt nanostructures templated by microwave annealed PS-*b*-P2VP (23.6k-*b*-10.4k). (d) Picture of the Teflon isolation chamber used in the solvent isolation experiments. (e) Plots of defect density versus annealing temperature for several BCPs, solvents and annealing conditions. Reprinted with permission from ref. 1. Copyright © 2010 American Chemical Society.

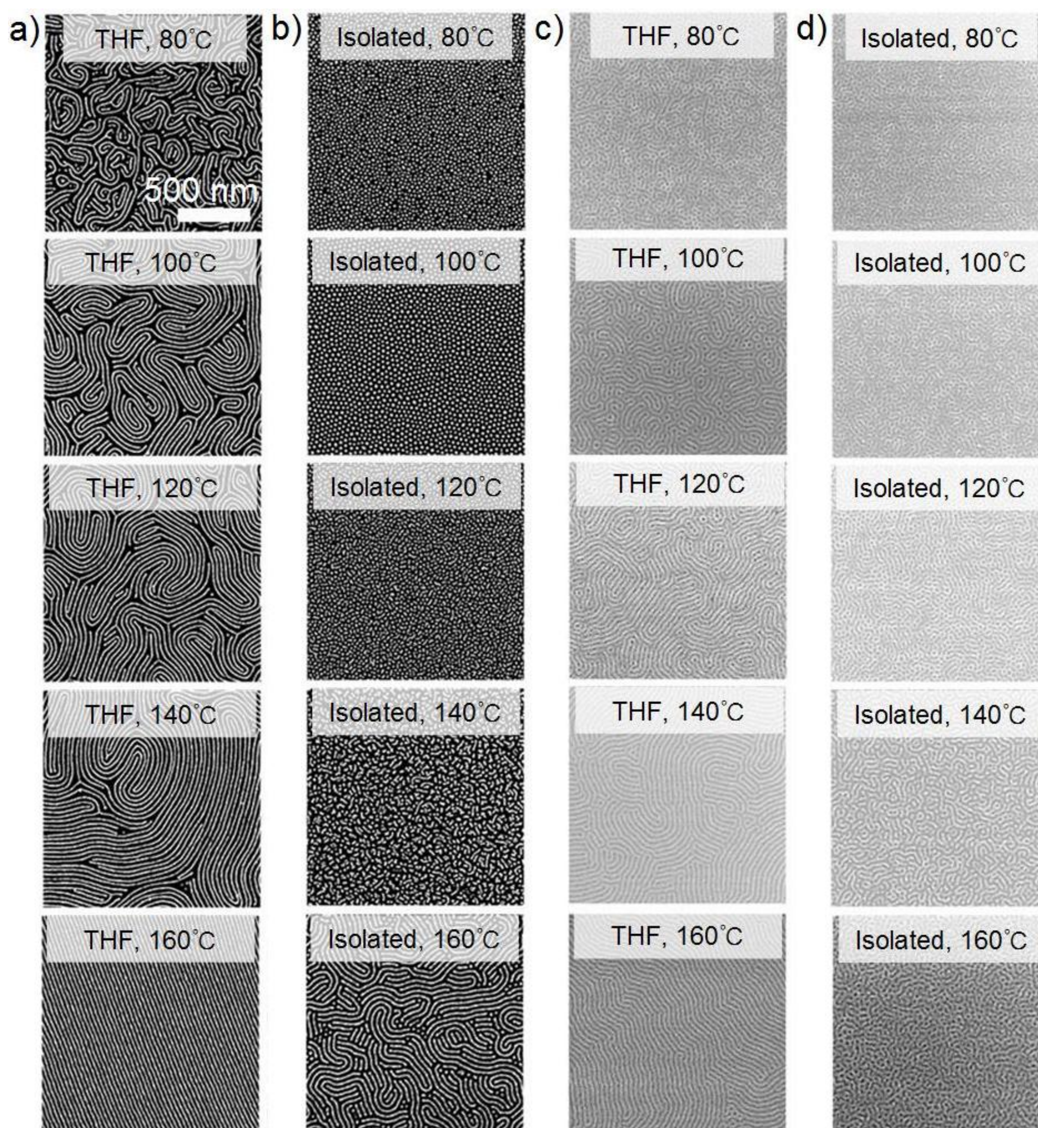

Figure 2.14. Studies to determine the effect of solvent and temperature. (a) and (b), SEM images of Pt nanostructures templated by THF-assisted microwave annealed PS-*b*-P2VP (32.5k-*b*-12k). (c) and (d), SEM images of THF-assisted microwave annealed PS-*b*-PMMA (45k-*b*-20k). Reprinted with permission from ref. 1. Copyright © 2010 American Chemical Society.

The solvents are heated under microwave irradiation conditions by "microwave dielectric heating" effects in which the amount of heat generated in

the heating process is dependent on the ability of the dipoles or ions in the solvent to align themselves with the frequency of the oscillating electromagnetic field.[27] Water, ethanol, N,N-dimethylformamide, and dichlorobenzene were also used as the solvent in the microwave annealing in addition to THF and toluene. SEM images of Pt nanostructures templated from microwave annealed PS-*b*-P2VP (23.6k-*b*-10.4k) using these solvents are shown in Figure 2.15. From the results, an effective solvent for microwave annealing should be a microwave absorber and effective solvents also appear to solubilize both polymer blocks without strongly favoring either. In the case of water and ethanol, self-assembled BCP microdomains were not observed after microwave annealing [Figure 2.15 (c) and (d)].

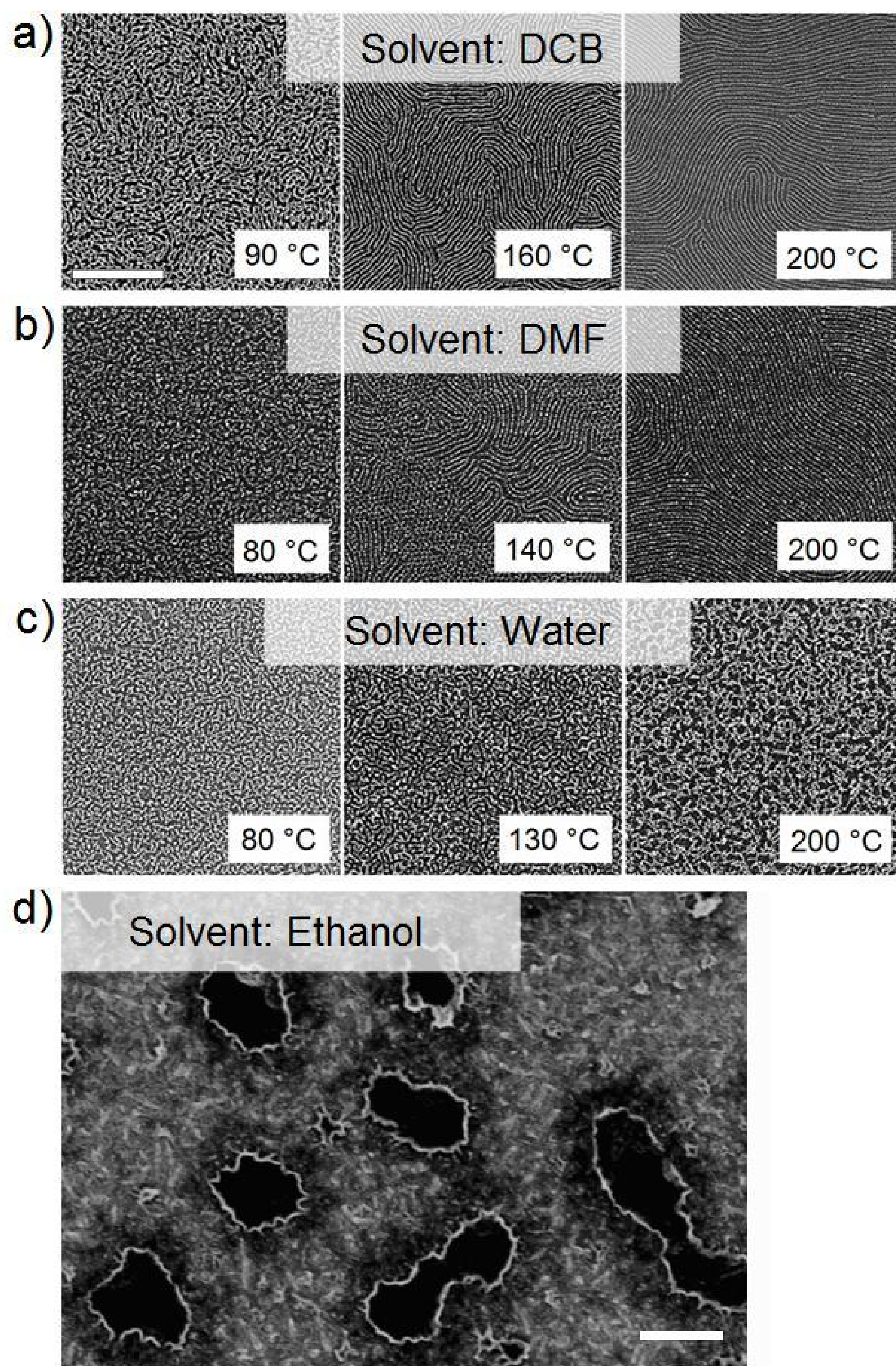

Figure 2.15. SEM images of Pt nanostructures templated by 180 s microwave annealed PS-*b*-P2VP (23.6k-*b*-10.4k) using different solvents: (a) DCB, (b) DMF, (c) water, and (d) ethanol. Scale bar = 500 nm. Reprinted with permission from ref. 1. Copyright © 2010 American Chemical Society.

Microwave Annealing vs. Pure Thermal Annealing

When pure thermal annealing was compared to solvent-assisted microwave annealing, it was shown that to attain a similar structure and similar defect density, pure thermal annealing required longer annealing times (36 h vs. several minutes) and higher anneal temperatures (Figure 2.16). The thermal annealing was carried out in a vacuum oven. BCP thin film coated silicon substrates were first placed inside the oven at room temperature and then annealed at desired temperatures in vacuum for 24 h. A 12 h cooling process was applied before the samples were removed from the oven.

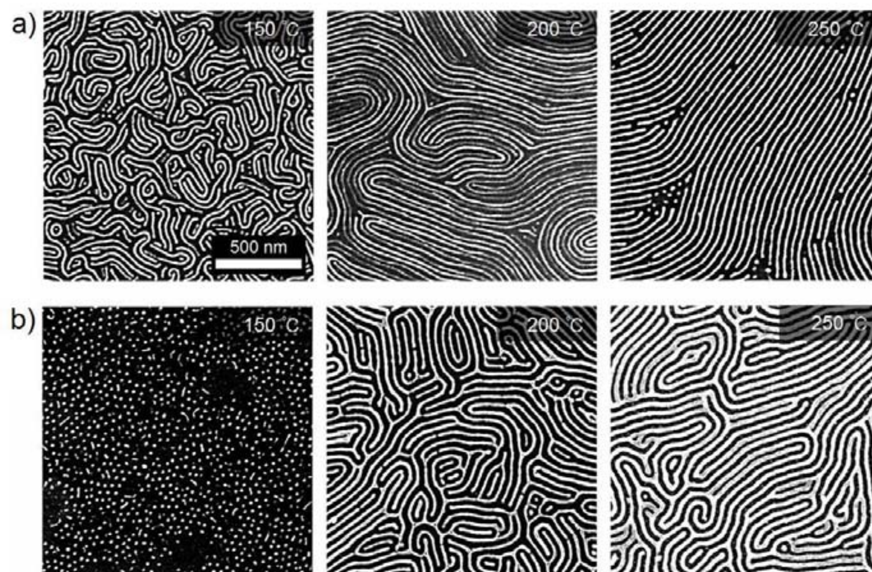

Figure 2.16. (a) And (b) SEM images of Pt nanostructures templated by thermally annealed PS-*b*-P2VP (32.5k-*b*-12k) and (44k-*b*-18.5k) BCPs, respectively. Reprinted with permission from ref. 1. Copyright © 2010 American Chemical Society.

Substrate Resistivity

Substrate resistivity is another key factor in microwave annealing. To investigate the critical role of substrate resistivity in rapid microwave annealing, we ran BCP samples that were spin-coated on silicon substrates with various resistivities. Four n-type silicon(100) substrates with a nominal resistivity of 1-5 Ω·cm, 0.08-0.1 Ω·cm, 0.01-0.02 Ω·cm, and 0.002-0.005 Ω·cm were used. The annealing target temperature was 130 ^{o}C and was held for 180 s for the THF and toluene assisted microwave annealing of BCPs on substrates with different resistivities. Top-down SEM images in Figure 2.17 (a) and (b) show how the organization of the annealed BCP films improved as the resistivity of the substrate was reduced. Distinctly different self-assembled BCP structures were observed. For instance, the metallized polymer domain morphologies in Figure 2.17 (a) show a quasi-hexagonal dot pattern and short nanoline structures with a length around 200 nm on the 1-5 Ω·cm substrates; fewer dots and longer nanolines formed on the 0.08-0.1 Ω·cm substrates; fingerprint structures with an average size of 600 nm appeared on the 0.01-0.0 2Ω·cm substrates; and parallel nanoline structures were obtained on the 0.002-0.005 Ω·cm substrates. Similar results were observed in the toluene assisted annealing system. For example, a dot pattern was seen on the 1-5 Ω·cm substrates; fewer dots and short nanolines formed on the 0.01-0.02 Ω·cm substrates; and fingerprint structures were obtained on the 0.002-0.005 Ω·cm substrates. To quantify the conductivity evolution, defect density in the domain structure of the samples was counted within a 1.5 μm by 1.5 μm frame.

The lowest conductivity silicon substrate has two orders of magnitude more defects than the highest conductivity silicon substrate, as shown in Figure 2.17 (c).

Lower resistivity wafers appear to be better microwave absorbers in the Biotage microwave system since more organized BCP nanostructures were observed on substrates with lower resistivities. The free carriers in silicon that vibrate according to the electrical field of the microwave may result in the observed microwave absorption in the doped silicon substrates.[29] Such a vibration causes a flow of electrons in the silicon that generates heat through resistance heating mechanisms.[29] In doped silicon, the number of free carriers is dependent on the doping level. In n-type silicon, which is doped with group V elements, the extra electrons in the lattice are the free carriers that can vibrate under microwave irradiation to generate heat. The more free carriers (extra electrons) in the n-type silicon, the more microwave energy it can absorb.

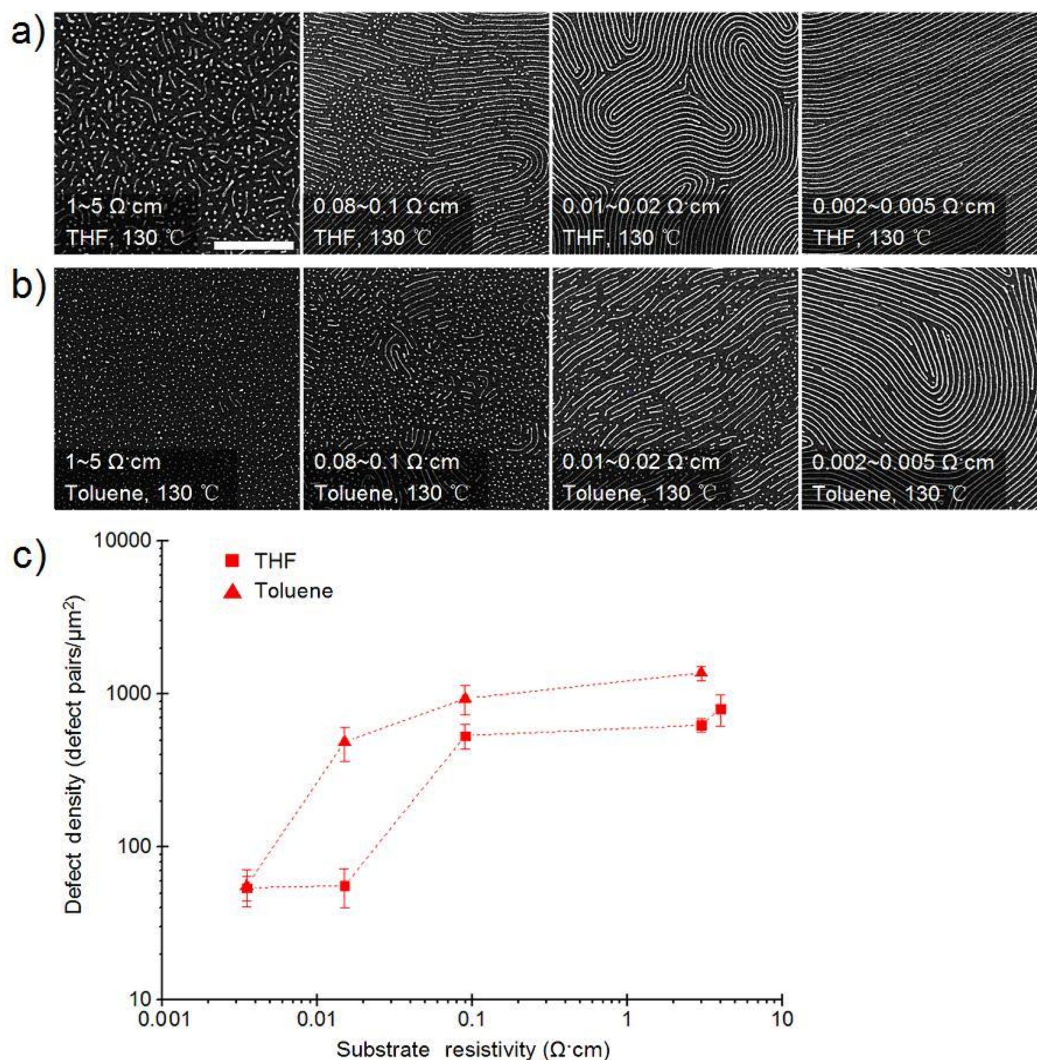

Figure 2.17. Influence of substrate resistivity over BCP organization. (a) and (b) SEM images of Pt nanostructures templated from PS-*b*-P2VP (32.5k-*b*-12.0k) thin films that were microwave annealed at 130 ℃ for 180 s on Si(100) substrates of varying resistivity in the presence of (a) THF and (b) toluene. (c) Plots of the evolution of defect density as the substrate resistivity is varied. Reprinted with permission from ref. 1. Copyright © 2010 American Chemical Society.

Compatibility with Topographical Graphoepitaxy

Graphoepitaxy was used to control the alignment of BCP self-assembly under microwave annealing conditions. Wall-like 2D silica features of circles, lines, ellipses, stars, and letters were fabricated by e-beam lithography (by Nathanael Wu). Figure 2.18 illustrates the experimental procedure: PS-*b*-P2VP was spin-coated onto a topographically pre-patterned silicon substrate; the sample was then microwave annealed for 60 s followed by metallization and plasma processes. Finally, the polymer template was used to make Pt nanolines and they were observed to be confined inside the silica walls. The graphoepitaxial templates achieved a precisely controlled orientation of self-assembled BCP over long-range order.

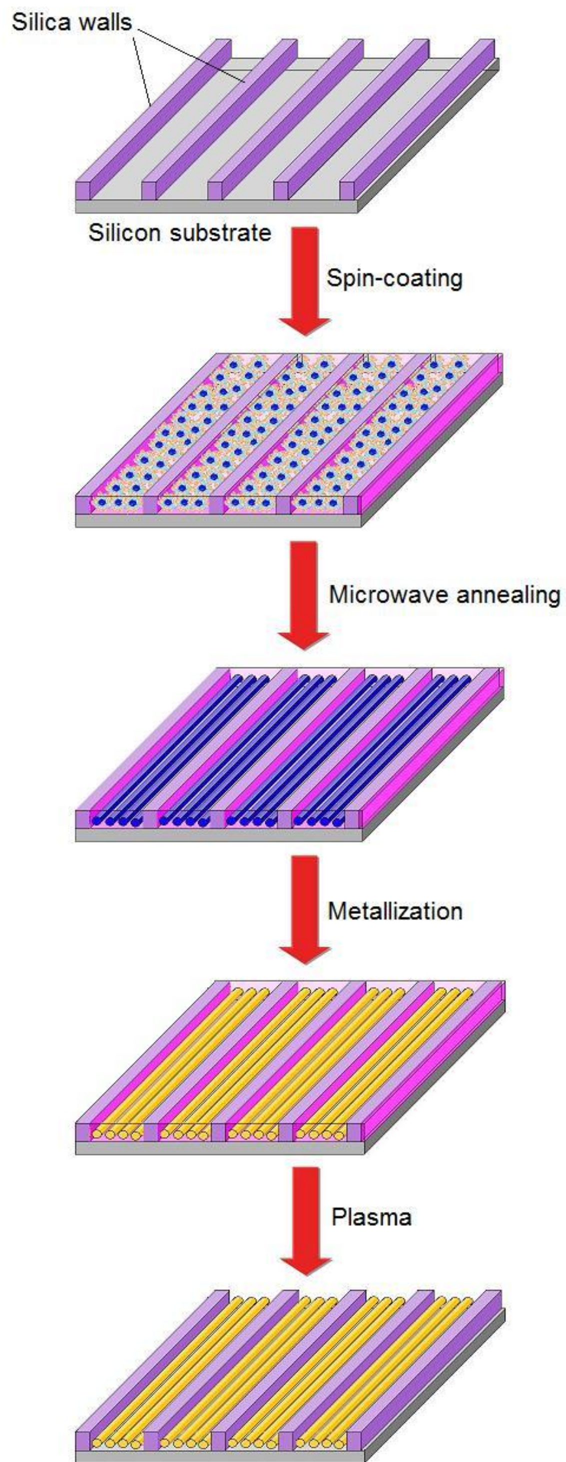

Figure 2.18. Outline of fast BCP self-assembly along graphoepitaxial features using microwave annealing.

Wall-like features were used and each silica line was produced with one e-beam scan that largely reduced the fabrication time (compared to trench-like graphoepitaxial features). The presence of the silica features leads to the formation of highly ordered, confined Pt nanolines, shown in the top-down SEM images in Figure 2.19. Pt nanolines formed on the surface patterned with circles that ranged from 500 nm to 4 μm. By combining high-resolution lithography and our solvent-assisted microwave annealing, directed features could be created on the surface within minutes.

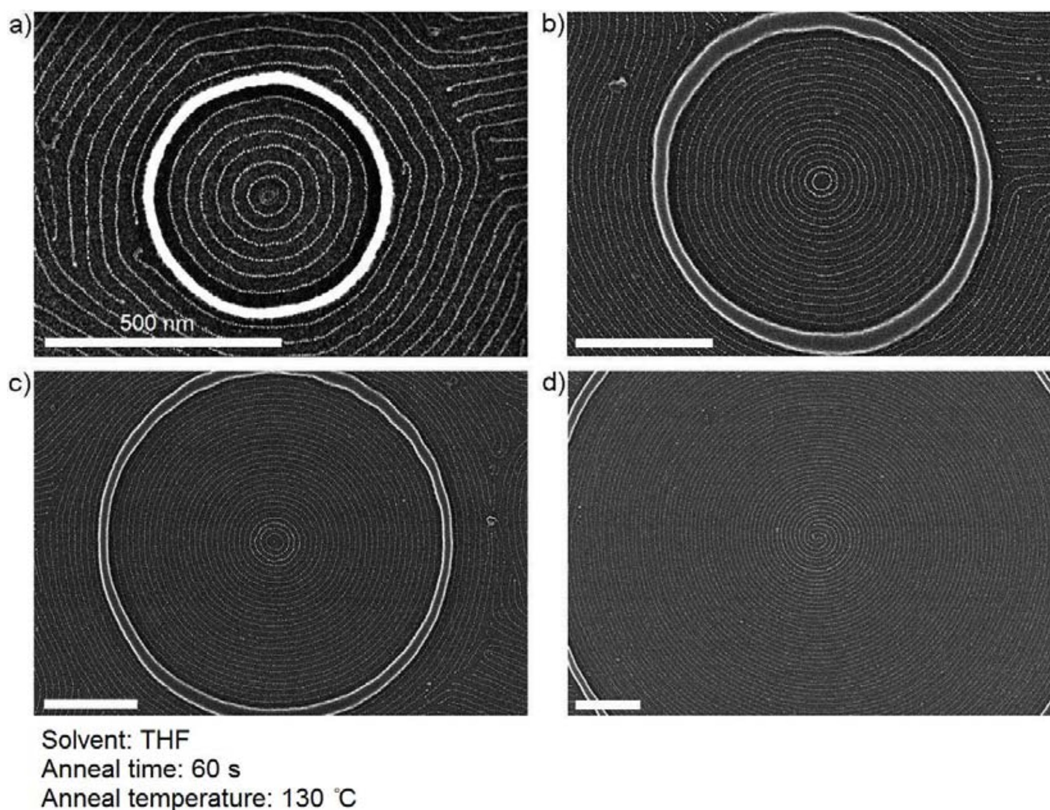

Figure 2.19. SEM images of Pt nanostructures templated from microwave annealed BCPs on e-beam patterned silicon substrates. Reprinted with permission from ref. 1. Copyright © 2010 American Chemical Society.

Additional evidence for how the wall-like silica lines confine and direct the self-assembly of BCPs was demonstrated by annealing at different temperatures. The temperature effect has been discussed; we have shown how the polymer morphology changes with increasing temperature. With the presence of silica features on the surface, the temperature effect was very similar. PS-*b*-P2VP and PS-*b*-PMMA BCPs were spin-coated on silicon substrates patterned with silica line features; these samples were annealed for 180 s at different temperatures and then metallized with platinum (for PS-*b*-PMMA, they were treated with oxygen plasma after annealing to improve the visualization in SEM); the remaining polymer was removed by plasma. In the top-view and side-view SEM micrographs, at a high annealing temperature (130 $^{\circ}$C), the concentric circle platinum nanolines were well oriented inside the silica circle with a diameter of 1.5 μm; at low temperature (80 $^{\circ}$C), most of the nanolines were not oriented (Figure 2.20), except those close to the silica lines.

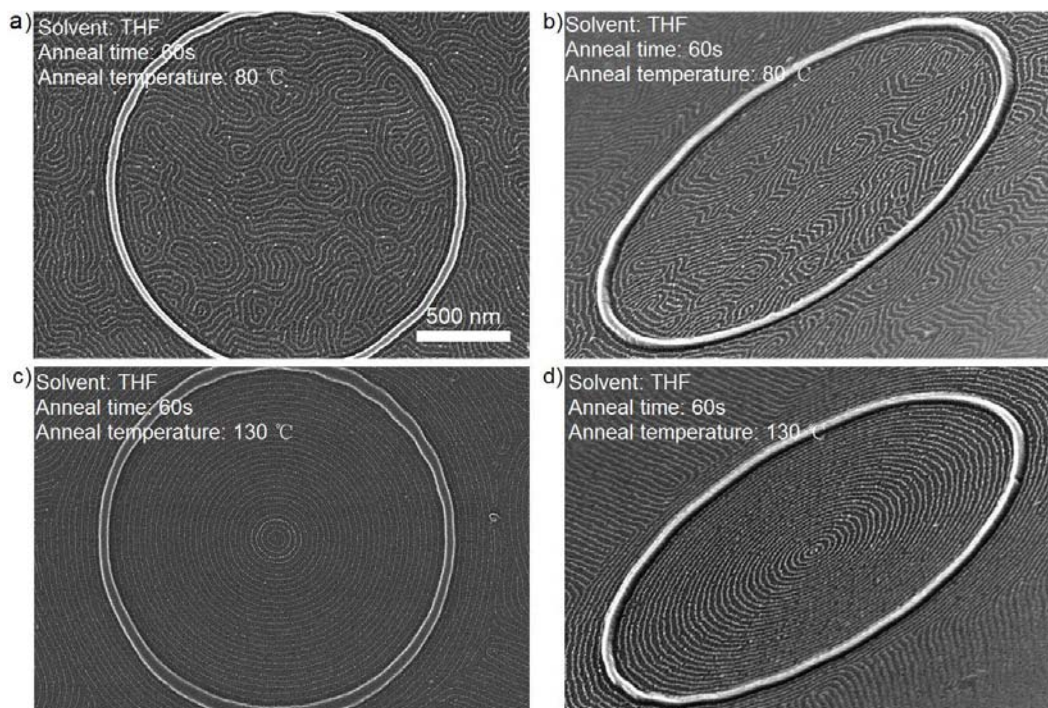

Figure 2.20. SEM images of Pt nanostructures templated from microwave-annealed BCPs at different temperatures. The microwave annealing was performed at (a) 80 ℃ and (b) 130 ℃ for 60 s. The substrates were pre-patterned with silica features by EBL. Reprinted with permission from ref. 1. Copyright © 2010 American Chemical Society.

A clearer comparison is given in Figure 2.21, which shows how the parallel silica lines with a width of 500 nm directed the self-assembly of the BCPs at increasing temperatures. The alignment and defect density of the microwave annealed BCP nanostructures improved as the annealing temperature was increased from 80 ^{o}C to 180 ^{o}C. At lower temperatures, the self-assembled features did not follow the direction provided by two neighboring silica lines. At higher temperatures, the nanolines started to follow the same direction as the silica lines and less curved structures were observed. Parallel platinum nanolines finally formed at 120 ^{o}C and 180 ^{o}C for PS-*b*-P2VP and PS-*b*-PMMA,

respectively. Compared to unpatterned substrates (Figure 2.13), the density of defects decreased and the annealing temperature required to achieve this minimum order was reduced when topographical features were present. In the case of PS-*b*-P2VP (32.5k-*b*-12k), the minimum defect density decreased from 15 defects/μm^2 on an unpatterned substrate [Figure 2.13 (e)] to 2 defects/μm^2 with topographical features [Figure 2.21 (c)], even at a lower temperature.

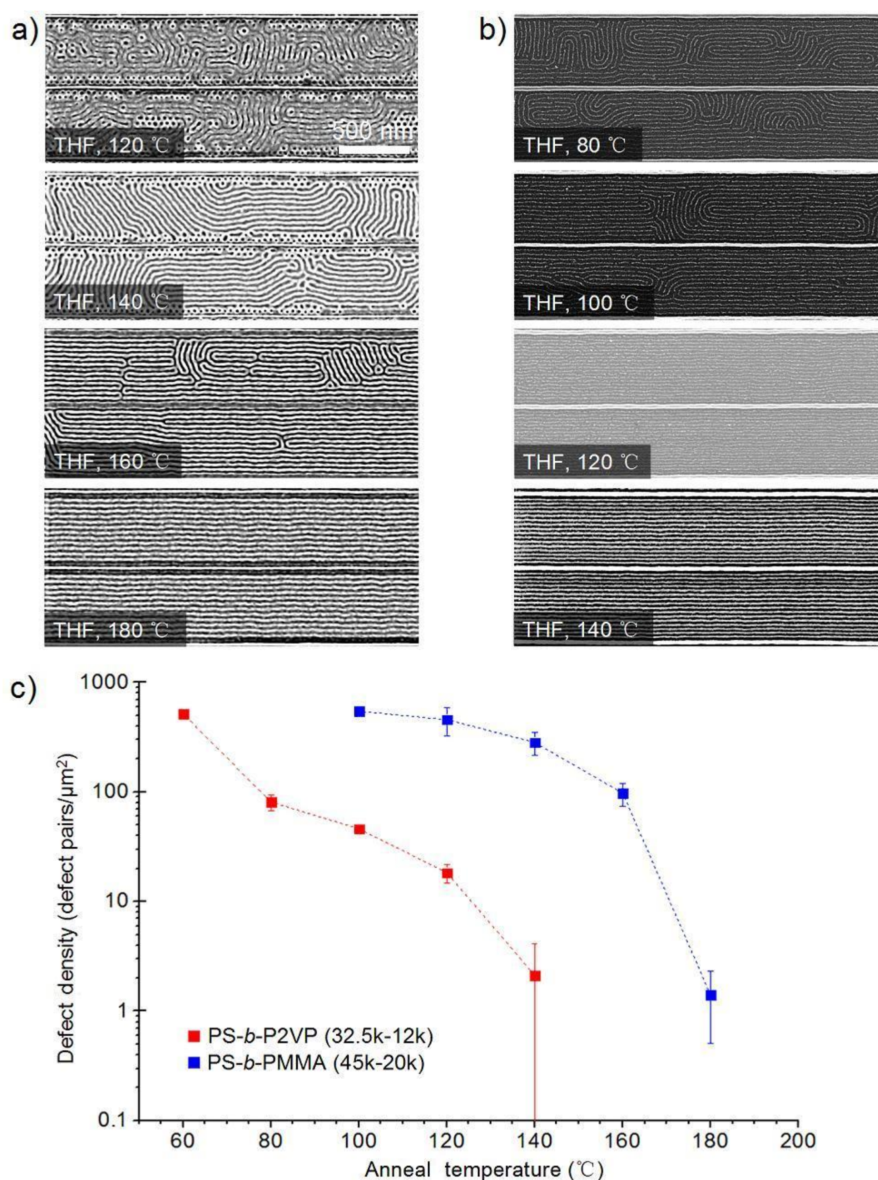

Figure 2.21. Rapid ordering of BCPs on surfaces with graphoexpitaxial features. (a) SEM images of microwave annealed PS-*b*-PMMA (45k-*b*-20k) structures aligned along silica walls. The BCP samples were microwave annealed for 180 s in the presence of THF. (b) SEM images of Pt nanostructures templated from microwave annealed PS-*b*-P2VP (32.5k-*b*-12.0k) BCPs. The BCP samples were microwave annealed for 60 s in the presence of THF. (c) Plots of the evolution of defect density as annealing temperature was varied on surfaces with graphoepitaxial features. Reprinted with permission from ref. 1. Copyright © 2010 American Chemical Society.

2.3. Conclusions

In this chapter, the strategy for rapid self-assembly of BCPs using microwave-based annealing was discussed. The results presented suggest that the combination of microwaves and solvent provide a solution for a rapid polymer annealing strategy. As a fast heating source, microwave energy enables quick and reliable fabrication of self-assembled BCP structures. By changing the annealing microwave power and the conductivity of the silicon substrate, control of directed assembly of BCPs is possible. The use of lithographically-patterned substrates provides control over the orientation and shape of the self-assembled materials. This new annealing technique allows fast-assembly of BCP PS-*b*-PVP and PS-*b*-PMMA; and it is reasonable to expect its applications in other systems on the basis of self-assembling materials and a microwave absorptive substrate, for example, poly(styrene)-*block*-poly(dimethylsiloxane) (PS-*b*-PDMS) (Figure 2.22). Our approach allows the rapid formation of cylindrical structures of BCPs and its applications may have potential use in chip manufacturing when combined with lithographic methods.

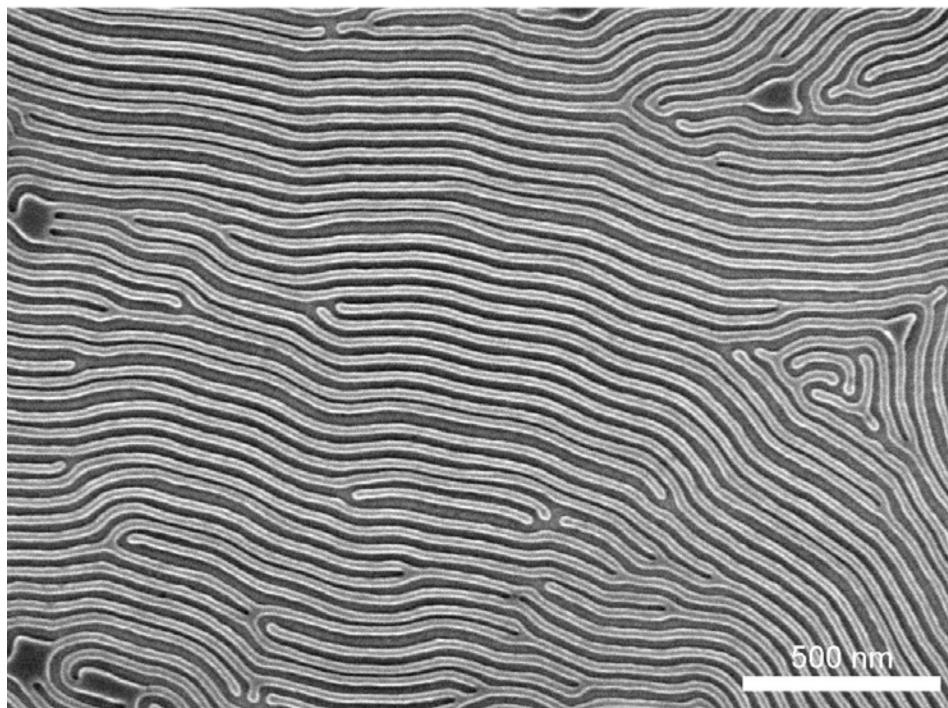

Figure 2.22. SEM of silica nanostructures templated by microwave annealed PS-*b*-PDMS. The annealing was preformed at 140 ^{o}C for 180 s.

2.4. Experimental Section

Generalities

All chemicals and solvents were used as received without further purification and all the experiments were performed under ambient conditions. Teflon beakers and tweezers were used during the wafer cleaning procedures; glass beakers and plastic tweezers were used during the metallization process. PS-*b*-P2VP BCPs with molecular weights (g/mol) of 23600-*b*-10400, 32500-*b*-12000, 44000-*b*-18500, and 50000-*b*-16500 and PS-*b*-PMMA BCP with molecular weight (g/mol) of 45000-*b*-20000 were obtained from Polymer Source Inc.. Aqueous hydrogen peroxide (Fisher, 30%), ammonium hydroxide (J. T. Baker,

30%), hydrochloric acid (J. T. Baker, 36.5%), methanol (Fisher, 99.8%), ethanol (Fisher, 99.8%), acetone (Fisher, 99.6%), benzene (Sigma Aldrich, 99.8%), dimethylformamide (DMF) (Sigma Aldrich, 99.8%), tetrahydrofuran (THF) (Sigma Aldrich, 99.9%), and toluene (Sigma Aldrich, 99.8%) were used in the preparations. High purity water was obtained from a Millipore system (18 MΩ•cm, Barnstead Nanopure water) and used throughout all experiments.

Wafer cleaning procedure

Pieces of approximately 9 mm by 9 mm prime-grade 100 mm Si (100) substrates were first degreased in an ultrasonic bath of methanol for 20 minutes. After removal from the ultrasonic bath, they were rinsed in acetone and ethanol, and dried with a stream of nitrogen gas. Standard RCA procedures were then conducted to clean the substrates: first, the silicon wafers were immersed in a hot solution of 30% NH_4OH (aq), 30% H_2O_2 (aq) and Millipore water in a ratio of 1:1:5, and heated at 85 °C for 20 minutes. The wafers were removed, rinsed with excess water, and immersed in another hot solution of 38% HCl (aq), 30% H_2O_2 (aq) and Millipore water in a ratio of 1:1:5 at 85 °C for 20 min. The wafers were again rinsed with excess water and dried under a nitrogen gas flow.

Formation of graphoepitaxial features

EBL was used to create wall-like features on silicon substrates. The silicon substrates were first cleaned via a piranha cleaning procedure: the substrates were immersed in a hot piranha solution [3:1 (v/v) mixture of conc. H_2SO_4 and 30%

H_2O_2 (aq)] for 15 min; the substrates were then removed from the solution, rinsed in water, and dried with a nitrogen gas flow. To remove water from the surface, the silicon substrates were then baked at 150 °C for 15 min in air. Hydrogen silsesquioxane (HSQ) was dissolved in methyl isobutyl ketone (MIBK) solvent to make a 1% solution, spin-coated onto the substrates via a two-speed process: first the sample was spread at 1000 rpm for 10 s, then spun at 3000 rpm for 30 s. The substrates were then baked at 100 °C for 15 min in air, and subsequently loaded into a RAITH 150-TWO e-beam lithography system for pattern writing. To remove the unexposed HSQ, the substrates were immersed in a 25% solution of tetramethylammonium hydroxide (TMAH) for 30 s. Wall-like SiO_2 features were left on the substrates. All graphoepitaxial samples were fabricated by Nathanael L. Y. Wu in the clean room, University of Alberta Centre for Nanofabrication.

BCP Thin Film Fabrication

PS-*b*-P2VP and PS-*b*-PMMA BCPs were weighed and dissolved in neat toluene at room temperature by stirring for 12 hours to make an ~1% w/w solution of BCP micelles. 16 μL of the BCP solution was then spin-cast on the cleaned silicon substrates at 4200 rpm for 50 s under an argon environment to form a polymer thin film. The film thickness was then measured by ellipsometry.

Microwave Annealing

A Biotage Initiator 2.5 system was used as the research grade microwave oven to anneal BCPs. To fit into the Biotage-compatible reaction tubes, the BCP-

coated silicon substrates were cut into 4.5 mm × 9 mm pieces. A custom-made microwave-transparent glass support was placed inside the reaction tube to hold the sample above 1.5 mL of solvent (most commonly THF or toluene). The reaction tube was then sealed, automatically placed inside the microwave chamber by the Biotage system, and irradiated with 2.45 GHz microwave energy. For safety reasons, the Biotage system is designed to increase microwave power incrementally until a pre-selected temperature is measured at the glass sample tube. The pre-heating process required roughly 15-90 s in most cases and it was only once this temperature was achieved that the pre-set annealing time began. The input power was recorded and a built-in infrared sensor monitored the temperature of the reaction tube during the heating process. The pressure inside the reaction vessel during the process was also recorded by the Biotage system and found to vary strongly with temperature and solvent.

Fabrication of Pt Nanolines Using Self-Assembled BCP Thin Films as Templates

To improve the visualization in SEM, the microwave annealed PS-*b*-P2VP samples were metallized. The samples were immersed in a Na_2PtCl_4 solution (20 mM) with HCl (aq) (1.6%, v/v) for 3 h. The metallization process was performed in a glass beaker. The samples were then rinsed thoroughly with Millipore water and dried with a nitrogen gas flow. An oxygen plasma cleaner (Harrick Plasma Cleaner/Sterilizer PDC-32G) was used to reduce the ion-loaded BCP thin films to platinum metal and remove the polymer at 0.12 Torr for 60 s.

Automated Defect Quantification

The defect quantification work was done by Jeffrey Murphy. Image analysis software (ImageJ) that minimized subjectivity and human error in the pattern analysis was used to measure the defect density and provide a quantitative means of describing order in BCP thin films. In this thesis work, the as-cast BCP thin films formed quasi-hexagonal arrays, and the microwave-annealed BCP thin films were transformed into aligned cylindrical structures. "Perfect" striped patterns only have parallel linear structures. Thus we defined defects as pairs of positive and negative disclinations, including dots, terminal points, and junctions. Examples of these three basic defect components (dots, termini and junctions) for the metalized PS-*b*-P2VP BCP are shown in Figure 2.23. The total number of disclination pairs is given by the following equation:

$$N = \frac{2n_{dots} + n_{terminal-points} + n_{Y-junctions} + 2n_{X-junctions}}{2}$$

Figure 2.23. Component structures for all defects observed in the experiments.

Characterization

The samples obtained in this study were characterized by scanning electron microscopy (SEM). SEM was performed with a Hitachi S-4800 FE-SEM using an electron energy of 15 keV under high vacuum conditions (<10^{-8} Torr).

2.5. References

(1) Zhang, X.; Harris, K. D.; Wu, N. L. Y.; Murphy, J. N.; Buriak, J. M. *ACS Nano* **2010**, *4*, 7021-7029.

(2) Chai, J.; Buriak, J. M. *ACS Nano* **2008**, *2*, 489-501.

(3) Harrison, C.; Adamson, D. H.; Cheng, Z.; Sebastian, J. M.; Sethuraman, S.; Huse, D. A.; Register, R. A.; Chaikin, P. M. *Science* **2000**, *290*, 1558-1560.

(4) Jo, A.; Joo, W.; Jin, W.-H.; Nam, H.; Kim, J. K. *Nature Nanotech.* **2009**, *4*, 727-731.

(5) Tang, C.; Lennon, E. M.; Fredrickson, G. H.; Kramer, E. J.; Hawker, C. J. *Science* **2008**, *322*, 429-432.

(6) Jenekhe, S. A.; Chen, X. L. *Science* **1999**, *283*, 372-375.

(7) Pochan, D. J.; Chen, Z.; Cui, H.; Hales, K.; Qi, K.; Wooley, K. L. *Science* **2004**, *306*, 94-97.

(8) Warren, S. C.; Messina, L. C.; Slaughter, L. S.; Kamperman, M.; Zhou, Q.; Gruner, S. M.; DiSalvo, F. J.; Wiesner, U. *Science* **2008**, *320*, 1748-1752.

(9) Mansky, P.; Liu, Y.; Huang, E.; Russell, T. P.; Hawker, C. *Science* **1997**, *275*, 1458-1460.

(10) Stoykovich, M. P.; Kang, H.; Daoulas, K. C.; Liu, G.; Liu, C.-C.; de Pablo, J. J.; Müller, M.; Nealey, P. F. *ACS Nano* **2007**, *1*, 168-175.

(11) Bosworth, J. K.; Paik, M. Y.; Ruiz, R.; Schwartz, E. L.; Huang, J. Q.; Ko, A. W.; Smilgies, D.-M.; Black, C. T.; Ober, C. K. *ACS Nano* **2008**, *2*, 1396-1402.

(12) Park, C.; Cheng, J. Y.; Fasolka, M. J.; Mayes, A. M.; Ross, C. A.; Thomas, E. L.; De Rosa, C. *Appl. Phys. Lett.* **2001**, *79*, 848-850.

(13) Bosworth, J. K.; Black, C. T.; Ober, C. K. *ACS Nano* **2009**, *3*, 1761-1766.

(14) Bai, J.; Zhong, X.; Jiang, S.; Huang, Y.; Duan, X. *Nature Nanotech.* **2010**, *5*, 190-194.

(15) Lyuksyutov, S. F.; Vaia, R. A.; Paramonov, P. B.; Juhl, S.; Waterhouse, L.; Ralich, R. M.; Sigalov, G.; Sancaktar, E. *Nature Mater.* **2003**, *2*, 468-472.

(16) Cheng, J. Y.; Mayes, A. M.; Ross, C. A. *Nature Mater.* **2004**, *3*, 823-828.

(17) Thurn-Albrecht, T.; Schotter, J.; Kastle, G. A.; Emley, N.; Shibauchi, T.; Krusin-Elbaum, L.; Guarini, K.; Black, C. T.; Tuominen, M. T.; Russell, T. P. *Science* **2000**, *290*, 2126-2129.

(18) Harant, A. W.; Bowman, C. N. *J. Vac. Sci. Technol. B* **2005**, *23*, 1615-1621.

(19) Park, S.; Lee, D. H.; Xu, J.; Kim, B.; Hong, S. W.; Jeong, U.; Xu, T.; Russell, T. P. *Science* **2009**, *323*, 1030 -1033.

(20) Stoykovich, M. P.; Muller, M.; Kim, S. O.; Solak, H. H.; Edwards, E. W.; de Pablo, J. J.; Nealey, P. F. *Science* **2005**, *308*, 1442-1446.

(21) Bita, I.; Yang, J. K. W.; Jung, Y. S.; Ross, C. A.; Thomas, E. L.; Berggren, K. K. *Science* **2008**, *321*, 939-943.

(22) Ruiz, R.; Kang, H.; Detcheverry, F. A.; Dobisz, E.; Kercher, D. S.; Albrecht, T. R.; de Pablo, J. J.; Nealey, P. F. *Science* **2008**, *321*, 936-939.

(23) Segalman, R. A. *Science* **2008**, *321*, 919-920.

(24) *International Technology Roadmap for Semiconductors, 2009 Edition*; Semiconductor Industry Association: San Jose, CA, 2009.

(25) Welander, A. M.; Kang, H.; Stuen, K. O.; Solak, H. H.; Müller, M.; de Pablo, J. J.; Nealey, P. F. *Macromolecules* **2008**, *41*, 2759-2761.

(27) Kappe, C. O. *Angew. Chem. Int. Ed.* **2004**, *43*, 6250-6284.

(28) Obermayer, D.; Gutmann, B.; Kappe, C. O. *Angew. Chem. Int. Ed.* **2009**, *48*, 8321-8324.

(29) Sameshima, T.; Hayasaka, H.; Haba, T. *Jpn. J. Appl. Phys.* **2009**, *48*, 021204.

(30) Ko, C.-J.; Lin, Y.-K.; Chen, F.-C. *Adv. Mater.* **2007**, *19*, 3520-3523.

(31) Zohm, H.; Kasper, E.; Mehringer, P.; Müller, G. A. *Microelectron. Eng.* **2000**, *54*, 247-253.

(32) Chai, J.; Wang, D.; Fan, X.; Buriak, J. M. *Nature Nanotech.* **2007**, *2*, 500-506.

(33) Ouk Kim, S.; Solak, H. H.; Stoykovich, M. P.; Ferrier, N. J.; de Pablo, J. J.; Nealey, P. F. *Nature* **2003**, *424*, 411-414.

(34) Muthukumar, M.; Ober, C. K.; Thomas, E. L. *Science* **1997**, *277*, 1225 -1232.

(35) Kang, H.; Kim, Y. J.; Gopalan, P.; Nealey, P. F. *J. Vac. Sci. Technol. B* **2009**, *27*, 2993-2297.

(36) Daoulas, K. C.; Muller, M.; Stoykovich, M. P.; Kang, H.; de Pablo, J. J.; Nealey, P. F. *Langmuir* **2007**, *24*, 1284-1295.

(37) Stein, G. E.; Liddle, J. A.; Aquila, A. L.; Gullikson, E. M. *Macromolecules* **2009**, *43*, 433-441.

(38) Yasin, S.; Khalid, M. N.; Hasko, D. G. *Jpn. J. Appl. Phys.* **2004**, *43*, 6984-6987.

(39) Stoykovich, M. P.; Daoulas, K. C.; Müller, M.; Kang, H.; de Pablo, J. J.; Nealey, P. F. *Macromolecules* **2010**, *43*, 2334-2342.

(40) Bang, J.; Jeong, U.; Ryu, D. Y.; Russell, T. P.; Hawker, C. J. *Adv. Mater.* **2009**, *21*, 4769-4792.

(41) Park, S.; Kim, B.; Yavuzcetin, O.; Tuominen, M. T.; Russell, T. P. *ACS Nano* **2008**, *2*, 1363-1370.

(42) Jung, Y. S.; Ross, C. A. *Nano Lett.* **2007**, *7*, 2046-2050.

Chapter 3
Control of Spacing of Metal and Hybrid Nanostructures Templated by Rapidly Self-assembled Binary BCP Blends Using Microwave Heating

3.1. Introduction

This work was carried out within the auspices of our block copolymer subgroup. Here I would like to gratefully acknowledge the important contributions of the other team members. In this work, all the e-beam lithographical features were fabricated by Nathanael Wu. The wax melting experiment (Figure 3.4) and thermal annealing of blend BC 5:5 [see Figure 3.1 (f)] were both done by Jeffrey Murphy. Jeffrey also carried out all the defect density quantification and feature spacing measurement work using the software tool he developed. Figures 3.5 (a) was drawn by Dr. Kenneth Harris, who helped me and guided all the way through this work. Pictures used in Figures 3.4 and 3.18 were taken by Jeffrey Murphy. Dr. Kenneth Harris, Jeffrey Murphy, and Nathanael Wu all contributed to useful discussions around this work, and their contributions need to be acknowledged.

The applications of BCP self-assembly include advanced nanolithography and nanostructure templating. In the International Technology Roadmap for Semiconductors (ITRS-2009), the self-assembly of BCPs is described as an innovative, emerging technology that provides new strategies to generate high-resolution patterns with nanoscale precision, and is considered to be a viable

extension of conventional lithography when combined with lithographically generated physical and chemical patterns.[1–7] In terms of applications, to be compatible with current manufacturing conditions, BCP self-assembly faces several important challenges: (1) the time required to achieve spontaneously self-assembled patterns over large areas needs to be reduced; (2) reducing the number of pattern defects; and (3) improving alignment. Chapter 2 addresses the alignment of BCP patterns via solvothermal annealing. This process is a simple microwave-based technique that is capable of generating ordered BCP patterns with very low defect density in minutes using a research-grade microwave reactor.[8] We have shown that factors such as the choice of solvent, annealing time, annealing temperature, and substrate resistivity were critical for controlling the BCP self-assembly. In this chapter, to increase the accessibility of the microwave annealing technique, we introduced an inexpensive household microwave oven to achieve rapid ordering of BCPs. Furthermore, using binary PS-P2VP BCP blends, we attained fine control over linear feature spacing (25 nm to 55 nm) in 60 seconds. In addition to this work, the fabrication of hybrid dot and line nanostructures using binary PS-P2VP/PS-P4VP blends was demonstrated.

Control of Spacing Using BCP Blends

The domain size and the spacing can be modified by varying the BCP molecular weight.[9,10] Conventionally, this requires a new BCP for each desired domain size and spacing. Blending BCPs with homopolymers is a widely used method to control the domain size and spacing in vertically-aligned cylinders and

lamellae.[11–15] For example, good control over the domain size and spacing in vertically aligned PS-PMMA cylindrical structures was demonstrated by Nealey and coworkers. The dimensions of the cylindrical structures of a ternary PS/PMMA/PS-PMMA blend can increase up to 50% compared to the dimensions of the neat BCP.[11] The problem is that BCPs eventually lose phase segregation if a large amount of homopolymer is added to the blends (Figure 3.1). The other way to control the feature spacings for lamellar structures is to use binary BCP blends.[16,17]

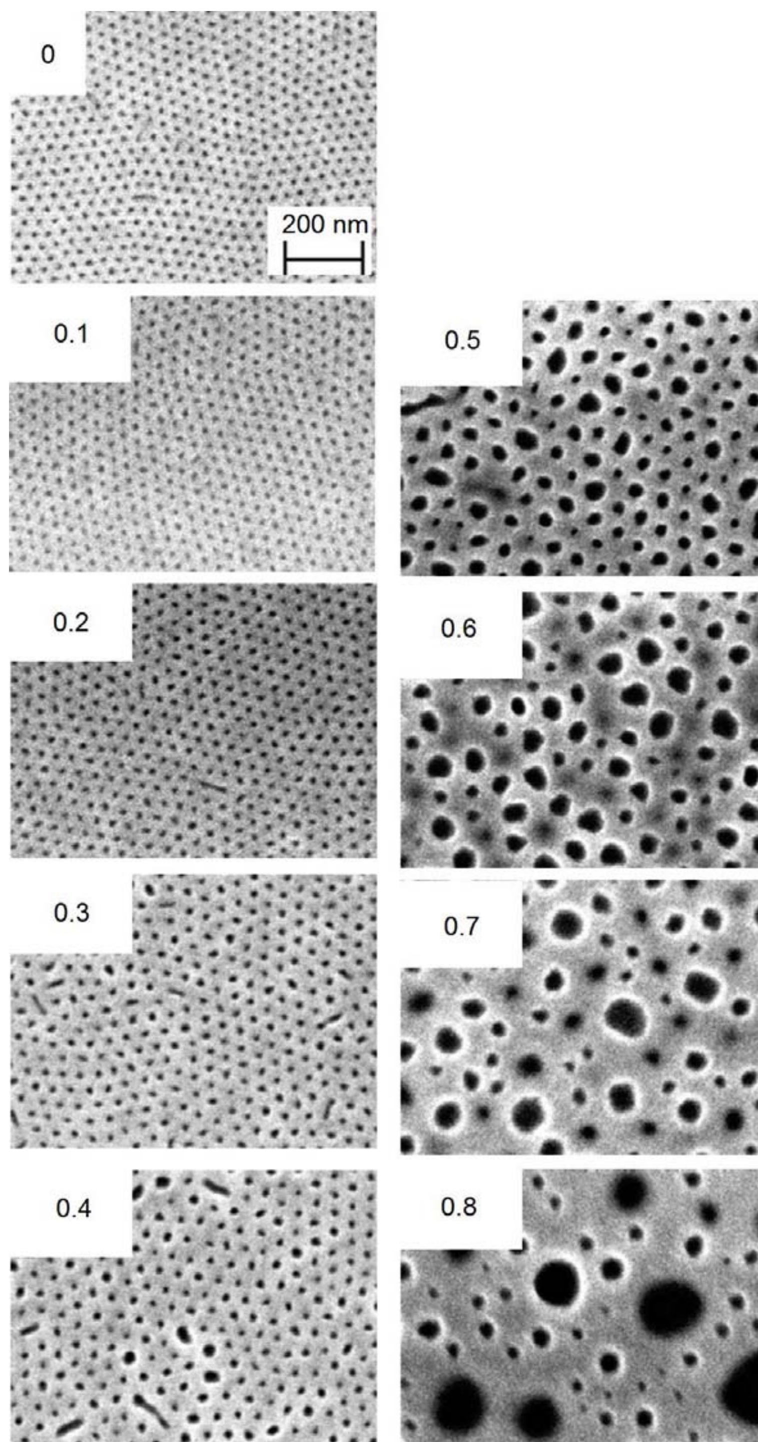

Figure 3.1. SEM images of PS-*b*-PMMA (46k-*b*-21k)/PS (21k)/PMMA (21k) blends. The volume fraction of homopolymer [PS (21k)/PMMA (21k)] in the blends is shown in the upper left corner of each SEM image. Reprinted with permission from ref. 11. Copyright © 2009 American Chemical Society.

Novel Morphologies Obtained Using BCP Blends

The phase-segregation behavior of diblock copolymers can be controlled by tuning the volume fraction of the blocks of the BCP. As illustrated in Figure 3.2, the morphology of an A-B diblock copolymer changes from spheres, cylinders to lamellar structures as the volume fraction of block A increases.

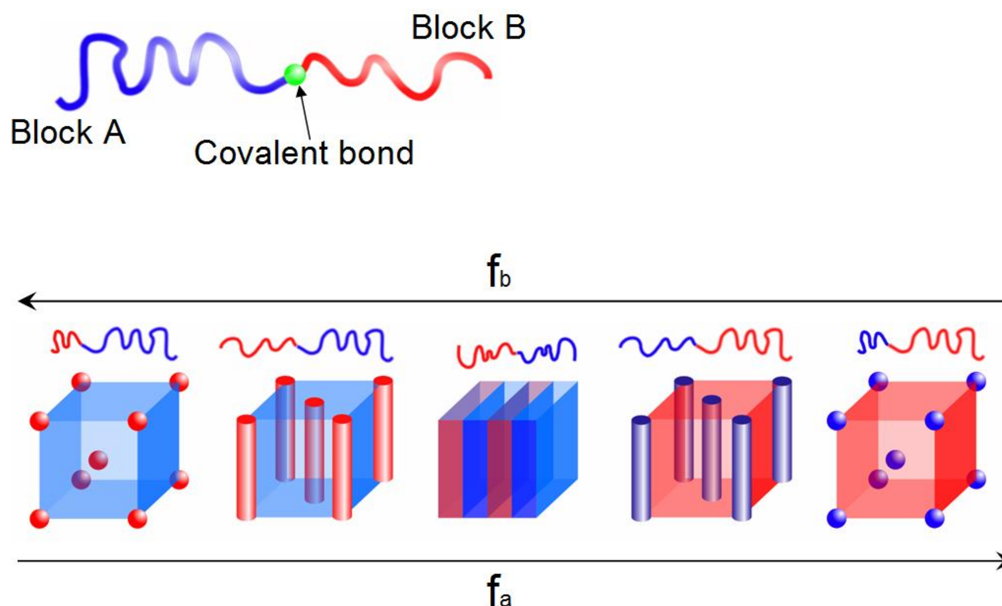

Figure 3.2. Typical morphologies of A-B diblock copolymer. (Inspired by BCP self-assembly picture from IBM: http://www.almaden.ibm.com/st/chemistry/ps/self_assembly/block_copolymer/)

BCP blending is another route to control the BCP morphologies.[18–27] Usually, two or more BCPs with different morphologies are blended together in order to get a desired morphology, to control the morphology of BCPs, or even create new morphologies that may not be found in homologous BCPs. He *et al.* reported the morphology and phase behaviors of binary PS-*b*-PMMA diblock copolymer

blends with different blending compositions.[27] The PS-*b*-PMMA blends were annealed with a selective solvent for the PMMA block, and by tuning blended components, new morphologies such as inverted phase or multilayer structures were observed in the blend thin films (Figure 3.3).

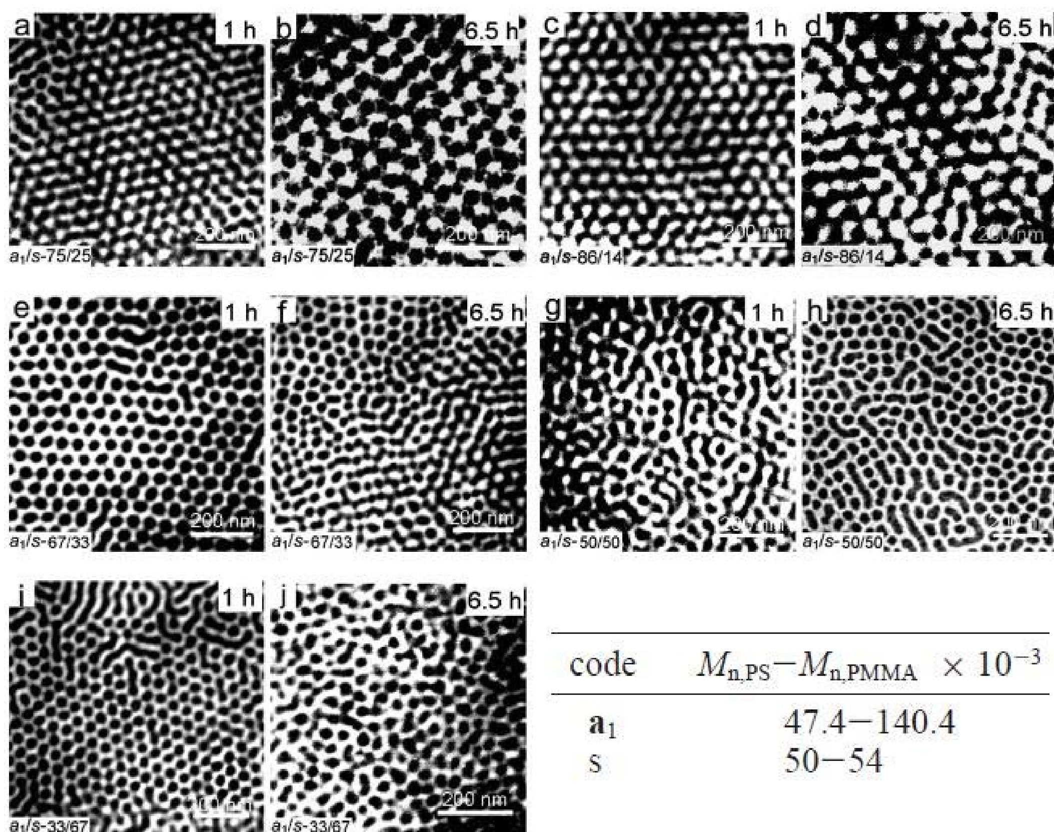

code	$M_{n,PS}-M_{n,PMMA}$ $\times 10^{-3}$
$\mathbf{a}_1$	47.4−140.4
s	50−54

Figure 3.3. TEM images of binary PS-*b*-PMMA blend thin films annealed in acetone vapor. Different morphologies were obtained as the ratio of the two components in the blends changed. The ratio of the two components is given in the left bottom of each image. Reprinted with permission from ref. 27. Copyright © 2005 American Chemical Society.

3.2. Results and Discussion

Choosing Appropriate Silicon Substrate

Because microwave annealing is a solvothermal process, the microwave absorptivity of the substrate is critical to producing linear BCP patterns. It would be ideal to measure and monitor the temperature of the doped silicon substrate during the annealing. It is not, however, feasible for us to do so at this point. In lieu of measuring the temperature directly, we indirectly tested the microwave absorptivity by melting a non-absorbing solid (paraffin wax) on doped silicon to choose the appropriate substrate for our experiments. Paraffin wax (melting point = 53-57 ℃; Sigma-Aldrich) was chosen to determine which silicon substrates were suitable because wax is a poor microwave absorber due to the lack of free charge carriers and low dipole moment, its high heat capacity (2.14 - 2.9 J g^{-1} K^{-1}), and the visible deformation when melted. In the melting test, we fixed the microwave irradiation power and time. Thus if the silicon substrate reached a sufficient temperature to melt the non-absorbing wax in a given time, it was deemed a candidate for further annealing experiments.

Paraffin wax squares were prepared by first melting and then coating an aluminum foil sheet and then left to cool down. It was then cut into small pieces with dimensions of approximately 7 mm × 7 mm × 0.5 mm. Each piece weighed roughly 24 mg and was placed on a 1.0 cm × 1.0 cm silicon substrate. Substrates with four different resistivities were tested: (1) 4-7 Ω·cm (Si(110), N-type), (2) 0.5-0.75 Ω·cm (Si(100), P-type), (3) <0.005 Ω·cm, (Si(100), P-type), and (4) 10-20 Ω·cm, (Si(100), P-type). The test was carried out by irradiating the wax-loaded

substrates simultaneously with microwaves for 30 seconds at maximum power. Samples were photographed immediately after removal from the oven to record their state (Table 3.1.).

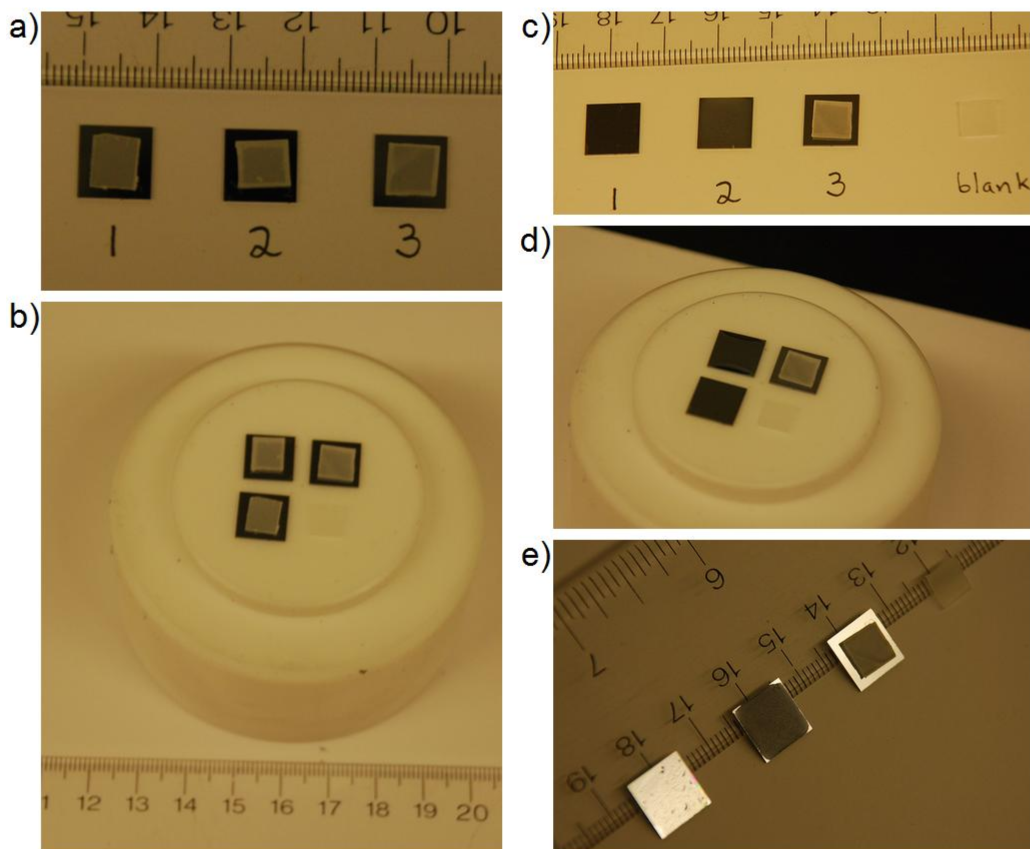

Figure 3.4. Images of wax samples on silicon substrates. (a) and (b): before microwave irradiation; (c), (d), and (e): after microwave irradiation. It can be seen that nearly all of the wax on substrate 1 is gone, due to a combination of vaporization and run-off; sample 2 was completely melted; both samples 3 and the wax sample without a silicon substrate were unchanged. Numbers correspond to those in the experiment. Experiment was done by Jeffrey Murphy and Xiaojiang Zhang; photographs by Jeffrey Murphy, licensed under the Creative Commons Attribution 3.0 Unported (CC BY 3.0) license.[28]

Sample	1	2	3	4	5
Weight of Wax (mg)	24.1	24	24.5	24.2	24.8
Weight of Substrate (mg)	117.4	119.3	121.6	121.1	0
Weight of Wax (mg), Final	2.1	23.3	24.2	13.2	24.8
% of Wax Loss	91%	3%	1%	45%	0%
Observation	Vaporized	Melted	No Change	Melted and Vaporized	No Change

Table 3.1. Wax melting test. Five small squares of wax were simultaneously tested: four squares on the four different silicon substrates (samples 1-4) and one square on the Teflon (PTFE) holder (sample 5).

Annealing in a Conventional Microwave Oven

The equipment and processes that were used to achieve rapid BCP self-assembly in a conventional household microwave oven and visualization of the resulting self-assembled patterns are briefly outlined in Figure 3.5. Cleaned silicon substrates were first spin-coated with neat BCPs or binary BCP blends to form polymer thin films roughly 40 nm thick (measured by ellipsometry). More specifically, the polymer solutions used for spin-coating were prepared as follows: neat PS-*b*-P2VPs BCPs were carefully weighed and dissolved in toluene to make 1.0 % (w/w) solutions; for the PS-*b*-P2VP / PS-*b*-P4VP and PS-*b*-P2VP / PS-*b*-P2VP blends, two pure BCP toluene solutions were mixed with a given ratio. In most cases, the spin-coated polymer films formed quasi-ordered hexagonal patterns on the silicon surfaces.

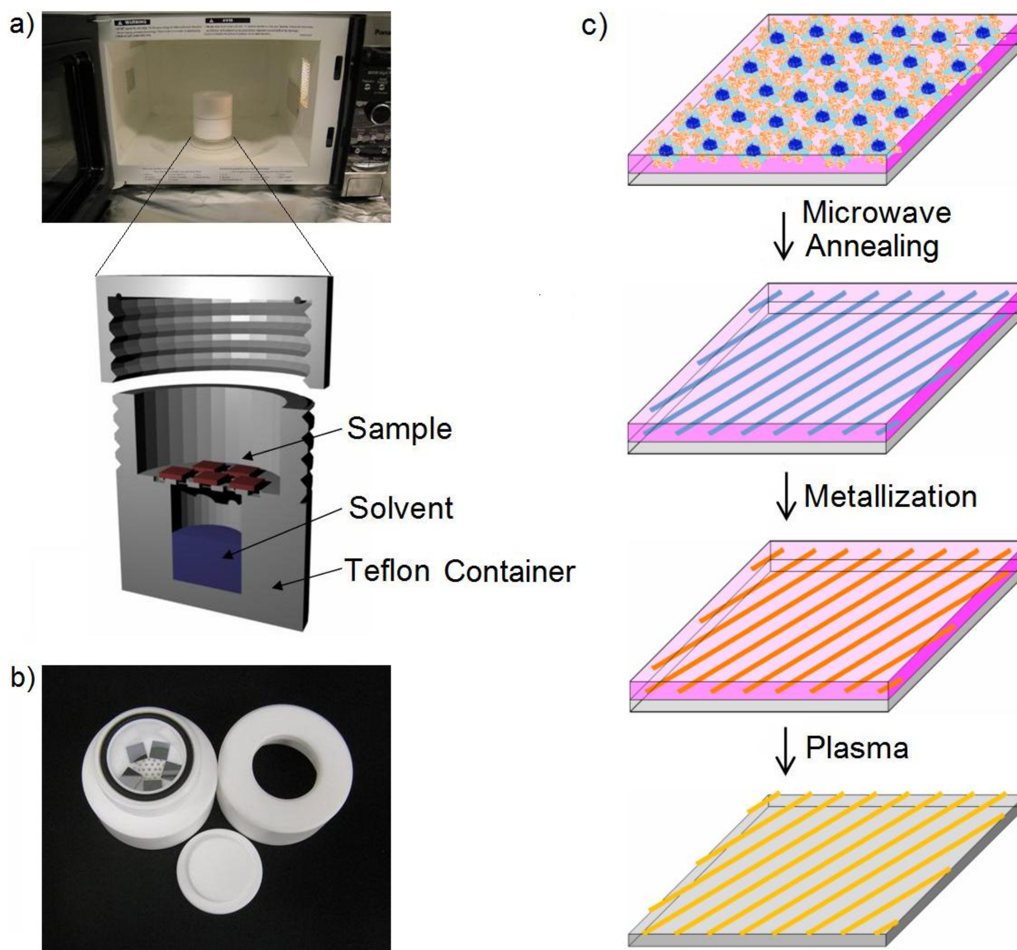

Figure 3.5. (a) Picture of sealed Teflon annealing chamber inside a household conventional microwave oven. (b) Picture of the disassembled Teflon annealing chamber. (c) Schematic outline of fabrication of ordered metallic nanowires using microwave annealing.

As demonstrated in Figure 3.6, these samples were sealed and annealed in a custom-made Teflon microwave annealing chamber with the presence of a solvent that, in all cases, was tetrahydrofuran (THF). A conventional microwave oven (Panasonic NN-SD377S) with a maximum power of 800 W was employed to irradiate microwave energy to the samples to increase the rate of organization (for

linear structures or hexagonally packed dot structures). The annealing chamber was always placed in the centre of the microwave oven to limit any effects due to anisotropy in the electromagnetic field. After microwave annealing, all samples were taken out of the annealing chamber immediately and metallization/plasma processes, described previously, were then undertaken to make the patterns visible by SEM.[8] A subsequent metallic pattern of a 60 second-microwave-annealed binary PS-*b*-P2VP/PS-*b*-P2VP blend is shown in Figure 3.7.

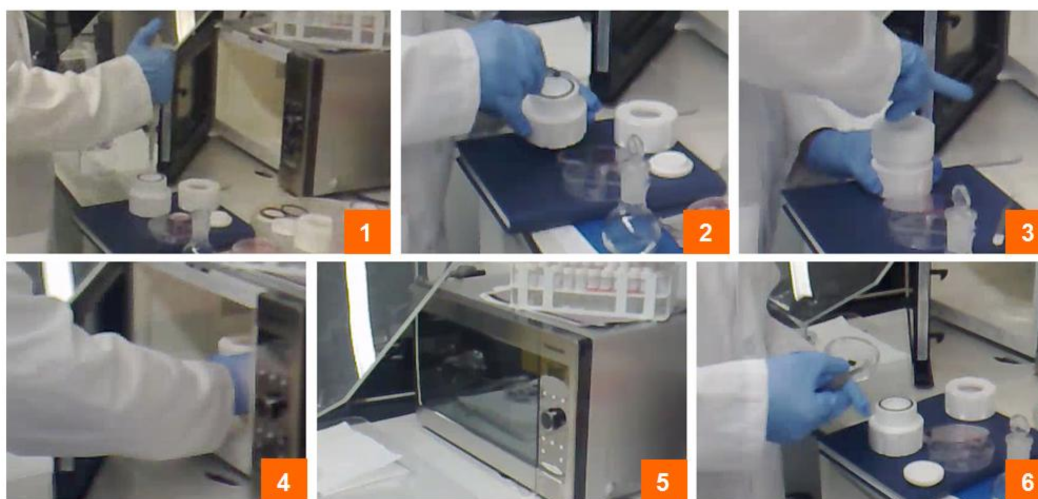

Figure 3.6. BCP annealing in a conventional microwave oven. (1) Adding solvent to the container. (2) Adding sample to the container. (3) Sealing the container. (4) Microwave annealing. (5) Sample removal.

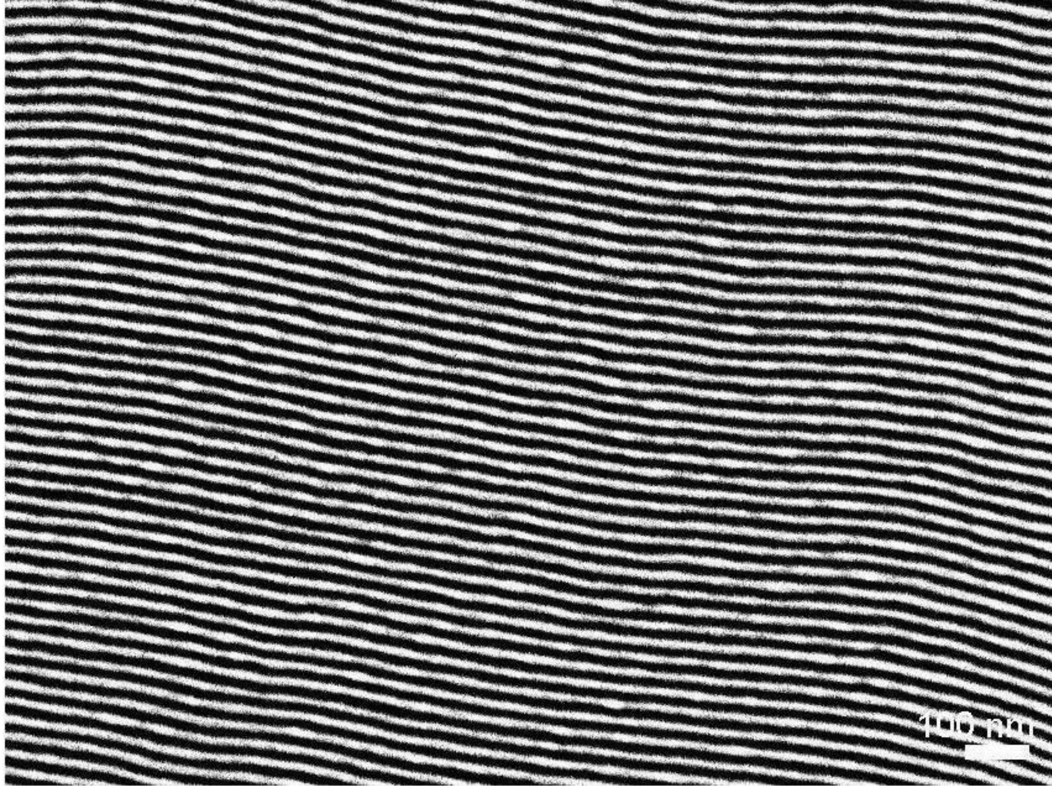

Pt features templated from PS-*b*-P2VP/PS-*b*-P2VP binary blend
Solvent: THF
Anneal time: 60 s

Figure 3.7. SEM image of Pt nanopatterns templated from a microwave annealed binary PS-*b*-P2VP (23.6k-*b*-10.4k)/PS-*b*-P2VP (50.0k-*b*-16.5k) blend [blending ratio = 7/3 (w/w)].

Binary BCP Blends: PS-b-P2VP / PS-b-P2VP

The general idea of feature spacing control is shown in Figure 3.8. In order to control the linear feature spacing, binary PS-*b*-P2VP blends were used. To make the binary blends, we employed six homologous BCPs (listed in table 3.2): (A) PS-*b*-P2VP (17.0k-*b*-9.8k), (B) PS-*b*-P2VP (23.6k-*b*-10.4k), (C) PS-*b*-P2VP (50.0k-*b*-16.5k), (D) PS-*b*-P2VP (125.0k-*b*-58.5k), (E) PS-*b*-P2VP (32.5k-*b*-12.0k), and (F) PS-*b*-P2VP (44.0k-*b*-18.5k).

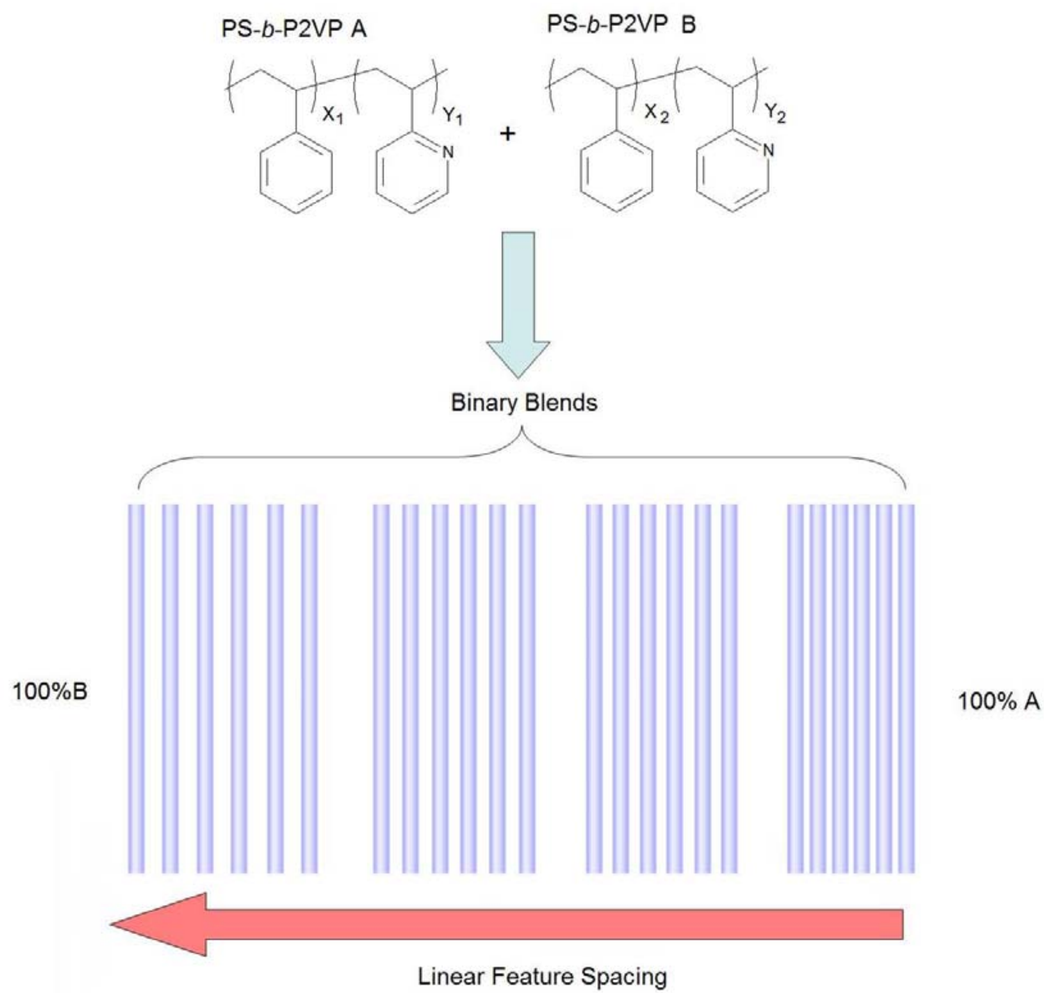

Figure 3.8. Outline for spacing control using binary PS-*b*-P2VP BCP blends.

BCP	PS (M_n)	P2VP (M_n)	PDI
A	17.0k	9.8k	1.06
B	23.6k	10.4k	1.04
C	50.0k	16.5k	1.09
D	125.0k	58.5k	1.05
E	32.5k	12.0k	1.05
F	44.0k	18.5k	1.05

Table 3.2. Table of commercially available PS-*b*-P2VP BCPs used in this work, identified in the text by the letter given. Number averaged molecular weights of each block and overall polydispersity indices are listed.

The BCPs were initially weighed and dissolved in neat toluene to form 1.5 % (w/w) solutions. Binary blends were prepared by mixing two of the BCP solutions with a chosen volume ratio (e.g. 900 µL of solution A were mixed with 100 µL of solution B to make blend AB 9:1). All the solutions were stirred for 12 hours at room temperature after mixing and prior to use. For the annealing, 60 s microwave irradiation was applied to BCP blends AC, BC, AD, and BD (Table 3.2). Figure 3.9 shows the SEM images of the Pt nanostructures templated from 60 s microwave-annealed BCP blends, together with the measured feature spacings and defect densities. The error bars for measured feature spacings and defect density indicate the standard deviation for at least 3 separate samples. From the measured spacings (Figure 3.9) one can notice that when two homologous BCPs were blended, the spacing of one neat BCP to that of the second neat BCP has a roughly linear progression. This property of the binary

blends should be useful to allow the assembly of any desired spacing within the dynamic range of the two BCPs.

Another interesting property of the blends is that for any given pair of PS-*b*-P2VP BCPs, the defect density minimum is generally achieved by using one of the blends rather than either of the two homologous BCPs. For example, for blend AD 5:5, the calculated polydispersity of the blend is 2.36 which is the largest in the entire AD blend series studied in this work. Blend AD 5:5, however, has the lowest defect density. This could be explained by the smaller component functioning as a plasticizer in the blend, resulting in greater polydispersity and more efficient annealing. To be clear, the defect density here is calculated relative to a perfectly aligned linear pattern without any dots, junctions, or terminal points. Defect densities were measured by Jeffrey N. Murphy using a computer-assisted counting algorithm.[8]

We found that even in the case where neither BCP naturally forms cylindrical structures, horizontal cylinders could be created by blending. For example, in blend AD, BCP A forms array hexagonally packed dots within a PVP matrix, while BCP D forms an array of hexagonally packed PVP dots in a PS matrix; however, when A and D were blended in suitable ratios, cylindrical structures were obtained.

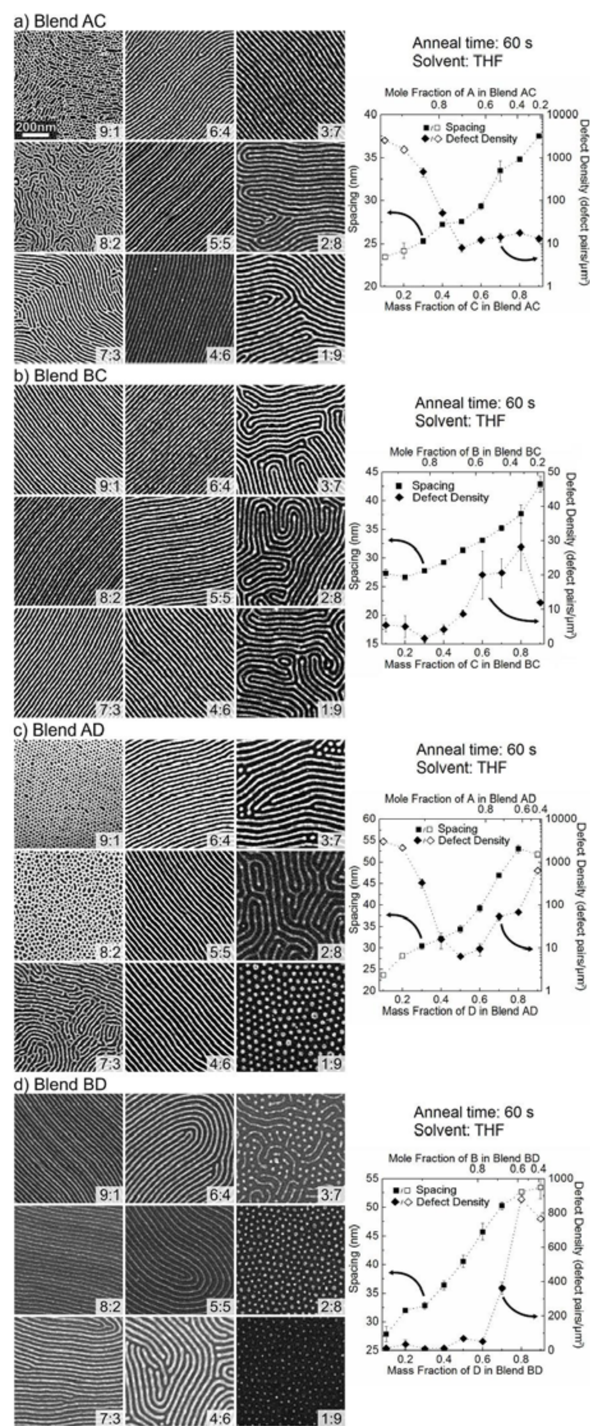

Figure 3.9. SEM images of Pt nanopatterns templated from PS-*b*-P2VP/PS-*b*-P2VP binary blends that were microwave annealed for 60 s and feature spacing and defect density as functions of the mass fraction of X in X/Y blend. *Macromolecules* **2011**, accepted. Copyright © 2011 American Chemical Society.

For blends AC 3:7 to 9:1, linear feature spacings ranging from 24.8 nm to 37.5 nm were obtained. Good control over spacing from 26.8 nm to 30.8 nm was obtained for blends AC 6:4 to 3:7, and the lowest defect density was achieved when blend AC 5:5 was used. Cylindrical nanostructures were attained when pure BCP B and pure BCP C thin films were annealed by microwaving for 60 seconds. Blend BC, which is a blend of these two BCPs, provided good control over linear feature spacing. The entire blend series produced line structures with spacing from 26.4 nm to 40.9 nm (Figure 3.9). For this series, the lowest defect density was achieved when blend BC 7:3 was used [Figure 3.9 (b)]. The lowest defect densities were attained when mass fractions of 5:5 and 7:3 were used for blend AD and BD, as shown in Figure 3.9 (c) and (d). Linear feature spacing of 32.5 nm to 38.4 nm and 29.3 nm to 42.5 nm were achieved by using blends AD 6:4 to 4:6 and blends BD 9:1 to 5:5, respectively [Figure 3.9 (c) and (d)]. Other PS-*b*-P2VP / PS-*b*-P2VP blends also provide the means to control the feature spacing. Examples of blend BF and AB are shown in Figure 3.10. In BCP / homopolymer binary blends, adding the homopolymer will offer control over the domain size and the feature spacing but large additions of the homopolymer may lead to nonuniform microstructures.[11] The PS-*b*-P2VP/PS-*b*-P2VP binary blends provide control over the linear feature spacing without disrupting the microphase-separated morphology of BCPs.

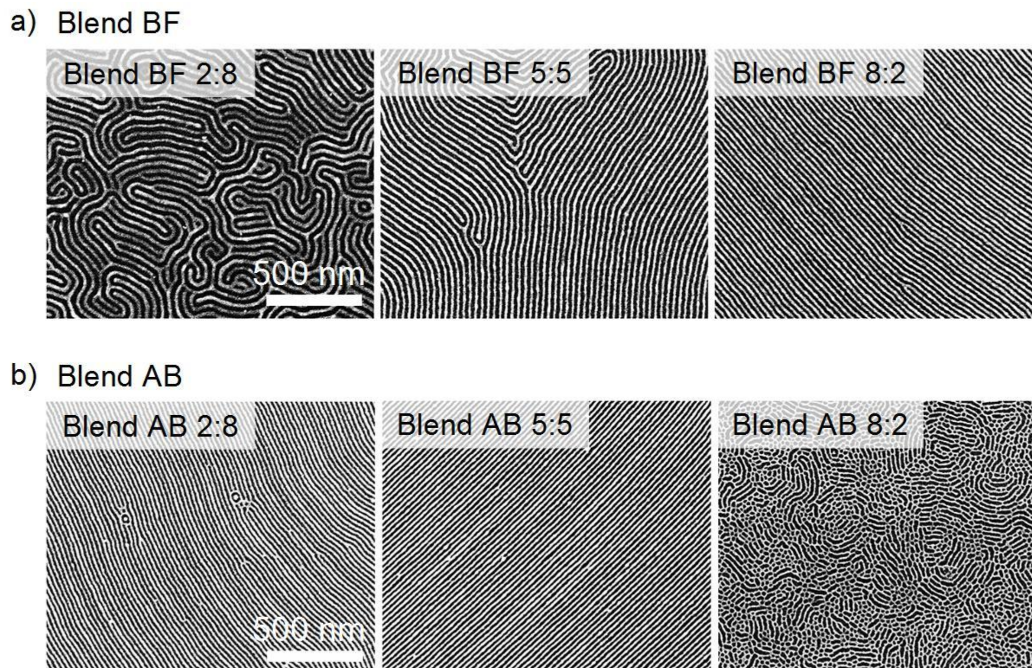

Figure 3.10. SEM images of Pt nanopatterns templated from binary blends BF and AB that were microwave annealed for 60 s. *Macromolecules* **2011**, accepted. Copyright © 2011 American Chemical Society.

Graphoepitaxially Directed Self-Assembly of Binary BCP Blends

Wall-like 2-D silica topographical features created by EBL were used to control the orientation and position of the Pt nanostructures templated by neat and blended BCPs annealed by microwaving for 80 s. As shown in Figure 3.11, a series of neat and BCP blended BCPs were chosen to achieve different spacings between the parallel silica lines with a half-pitch of 250 nm. The number of the lines can be controlled exactly: 19, 17, 16, 15, 13, and 12 lines were patterned between two silica lines by using BCP B, blend BC 7:3, BCP E, blend BC 4:6, blend AD 5:5, and blend AD 4:6, respectively.

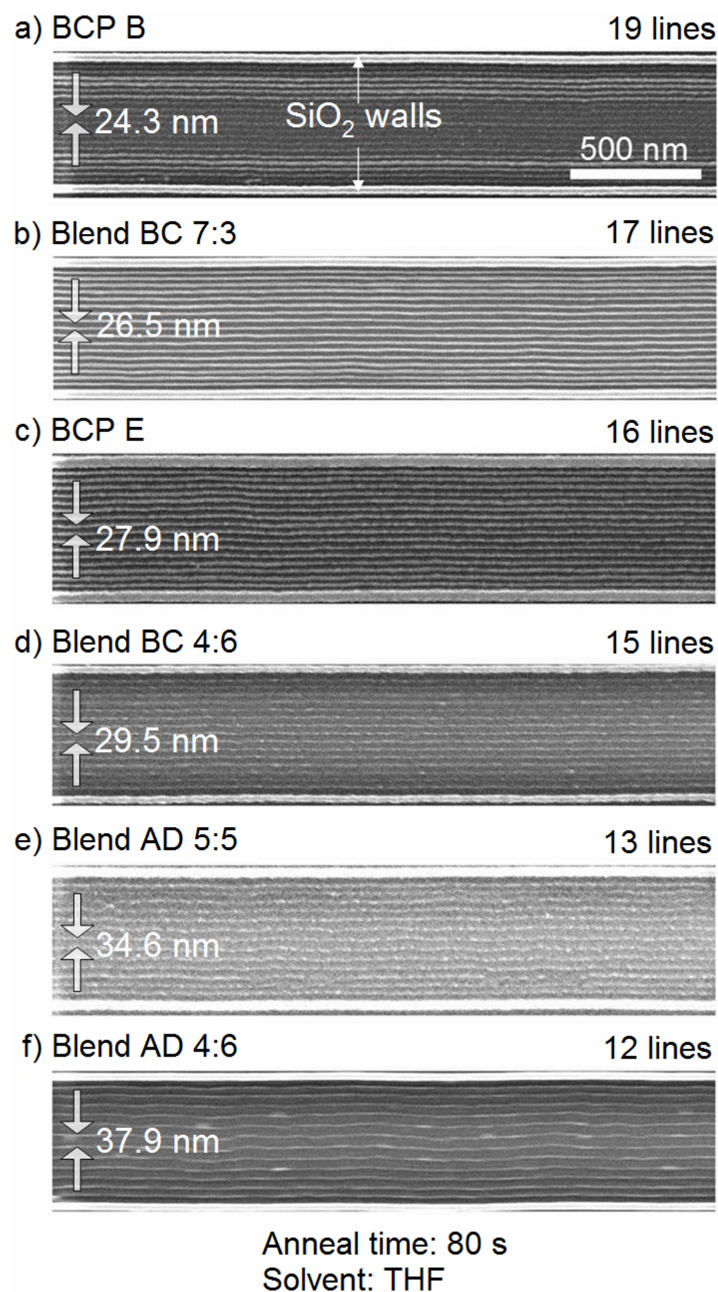

Figure 3.11. Linear feature spacing control along graphoepitaxially created silica wall-like strictures spaced 500 nm apart. SEM images of Pt nanostructures with six different spacings, templated by two neat BCPs and four blends: (a) BCP B, (b) blend BC 7:3, (c) BPC C, (d) blend BC 4:6, (e) blend AD 5:5, and (f) blend AD 4:6. In all cases, the microwave annealing time was 80 seconds. *Macromolecules* **2011**, accepted. Copyright © 2011 American Chemical Society.

Annealing in Conventional Microwave Oven: Time Evolution of BCP Self-Assembly

With a series of PS-*b*-P2VP BCPs and binary BCP blends, samples were microwave annealed for 10 to 120 seconds to investigate the importance of time of BCP self-assembly. Figure 3.12 shows SEM images of Pt nanostructures templated from microwave annealed BCP B, BCP C, and two binary BCP blends, BC 7:3 and BC 5:5. The results show that the measured defect densities were reduced more than one order of magnitude after only 10 seconds. Nearly parallel cylindrical nanostructures of P2VP were achieved after 60 seconds. Blend BC 7:3 had the lowest defect density, measured to be 1.4 defect pairs/μm^2 after 60 s annealing. It is known that larger BCPs require longer reorganization time.[29] However, blending a relatively small BCP [PS-*b*-P2VP (23.6k-*b*-10.4k)] with a larger BCP [PS-*b*-P2VP (50k-*b*-16.5k)] may reduce the reorganization time. The PS-*b*-P2VP/PS-*b*-P2VP blends offer an easy way to form parallel linear nanostructures. Furthermore, to compare the ordering speed in microwave annealing with the ordering speed in conventional thermal annealing, blend BC 5:5, which has the largest dynamic range of the four examples mentioned above was annealed in vacuum at 200 °C for given times ranging from 1 hour to 30 hours [Figure 3.12 (f)]. The results show that in thermal annealing, the defect density decreases with increasing annealing time but even after 30 hours annealing in vacuum, the subsequent defect density was still much higher than those samples which were microwave annealed for 60 seconds.

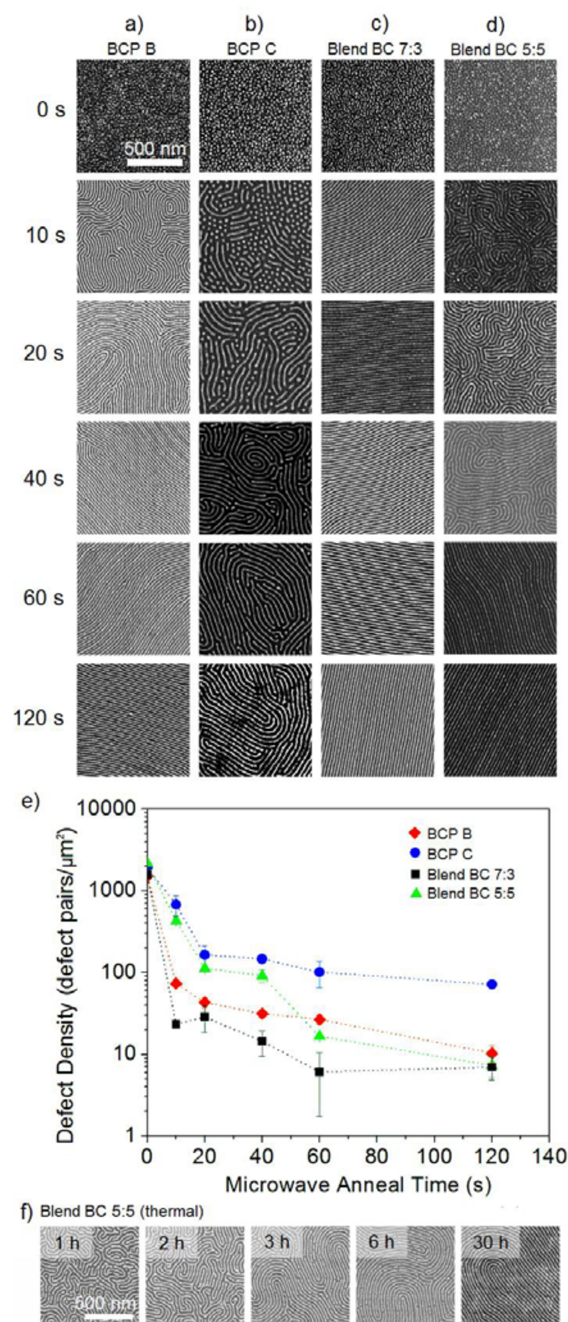

Figure 3.12. Influence of annealing time on the BCP pattern organization. (a) - (d) SEM images of Pt nanostructures templated by microwave annealed neat BCP and BCP blends. (e) Plots of the evolution of defect density for BCPs and binary BCP blends microwave annealed for 0 second to 120 seconds. (f) SEM images of Pt nanostructures templated by thermally annealed blend BC 5:5. *Macromolecules* **2011**, accepted. Copyright © 2011 American Chemical Society.

Binary BCP Blends: PS-b-P2VP / PS-b-P4VP

Binary mixtures of PS-*b*-P2VP and PS-*b*-P4VP were used to obtain hybrid nanostructures of dots and lines. The PS-*b*-P2VP / PS-*b*-P4VP blends used in this study are listed in Table 3.3. To prepare the blend solutions, PS-*b*-P2VP and PS-*b*-P4VP BCPs were weighed and dissolved in neat toluene with a given ratio and stirred overnight at room temperature. The polymer thin films of PS-*b*-P2VP / PS-*b*-P4VP blends were prepared on silicon substrates by spin-coating the blend solutions at 4800 rpm for 15 seconds. As summarized in Figure 3.13, the self-assembly of BCP blends led to hybrid nanostructures. For example, when blend IV (microwave annealed for 60 s) was used as the template to deposit Pt, a hybrid nanopattern of Pt nanodots and Pt nanolines was obtained as shown in the SEM image in Figure 3.13.

Blend	PS-*b*-P2VP	PS-*b*-P4VP	Mass Fraction of PS-*b*-P2VP
I	17.0k-*b*-9.8k	12.0k-*b*-3.2k	0.55
II	23.6k-*b*-10.4k	31.9k-*b*-13.2k	0.60
III	32.5k-*b*-12.0k	12.0k-*b*-3.2k	0.46
IV	32.5k-*b*-12.0k	31.9k-*b*-13.2k	0.72
V	32.5k-*b*-12.0k	47.6k-*b*-20.9k	0.60
VI	32.5k-*b*-12.0k	47.6k-*b*-20.9k	0.62

Table 3.3. Table of the PS-*b*-P2VP / PS-*b*-P4VP blends used in this study. All BCPs are commercially available.

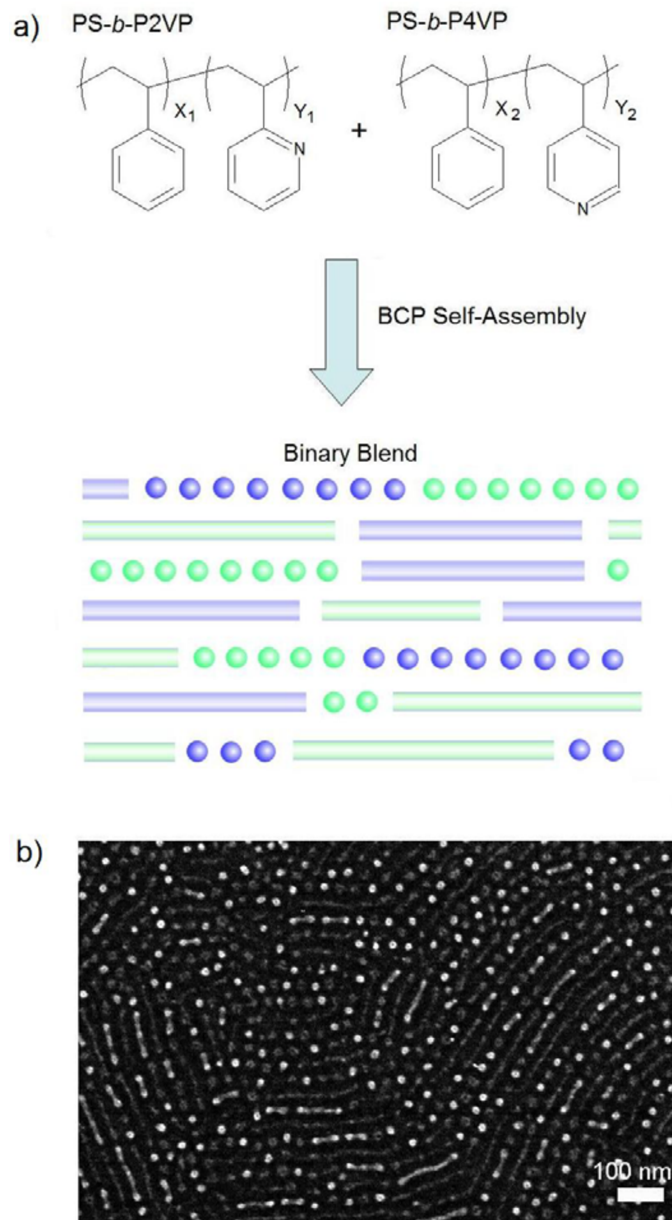

Figure 3.13. (a) Outline for using binary PS-*b*-P2VP / PS-*b*-P4VP blends to produce hybrid nanostructures. (b) SEM image of Pt nanostructures templated by 60 s microwave annealed blend IV.

Due to the similarity in chemical structures, it is difficult to directly distinguish PS-*b*-P2VP and PS-*b*-P4VP in the blending system; indirect evidence

was used instead. In the first experiment, blend V was spin-coated on a flat silicon substrate and annealed with neat THF for 24 hours at room temperature. After removal from the solvent annealing system, the BCP film was metallized with Pt and oxygen plasma was used to remove the polymer. Figure 3.14 shows the hybrid Pt nanostructures templated by the binary blend. The two constituents of blend V, PS-*b*-P2VP (32.5k-*b*-12.0k) and PS-*b*-P4VP (47.6k-*b*-27.9k), have PVP blocks with different molecular sizes. From the SEM image, dot structures with two distinct domain sizes and line structures with two distinct widths are observed. Logically, one could conclude that the thinner Pt dots and lines were templated by self-assembled PS-*b*-P2VP and the thicker were templated by self-assembled PS-*b*-P4VP, but this remains to be determined.

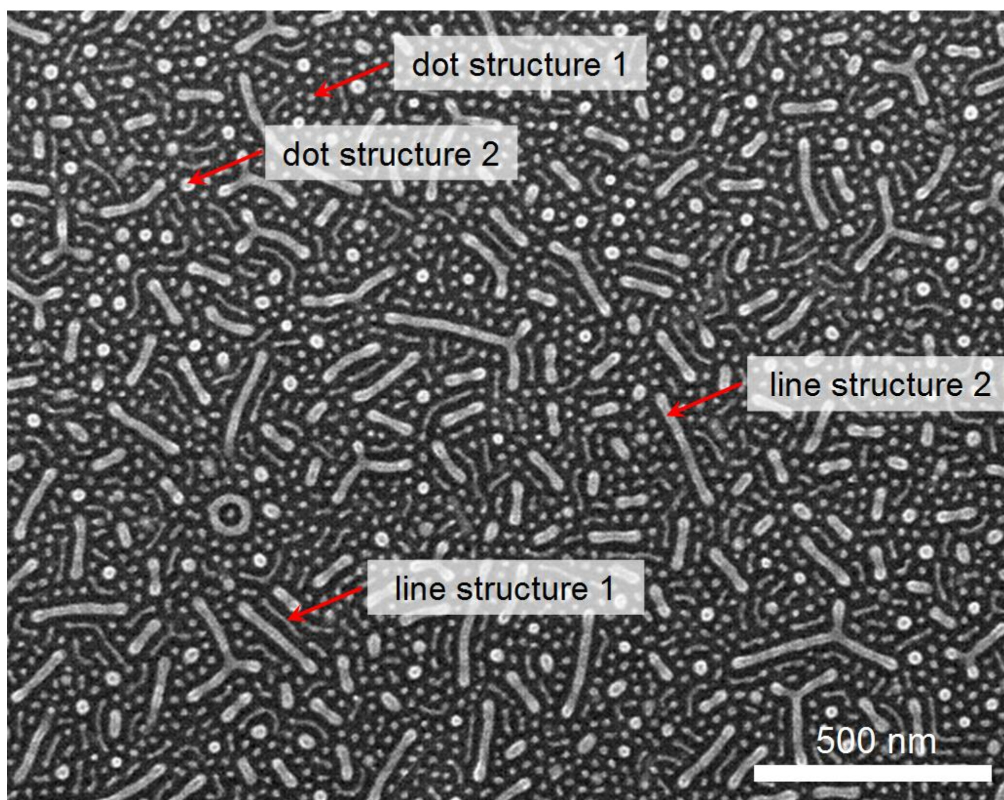

Figure 3.14. SEM image of Pt nanostructures templated by 24 hours solvent annealed blend V.

In the second experiment, two binary blends (blend III and IV) that both have PS-*b*-P2VP (32.5k-*b*-12k) components were compared. Blend III and IV were spin-coated on silicon substrates, microwave annealed for 60 seconds, and metallized separately. The Pt nanostructures templated by self-assembled blends III and IV are shown in Figure 3.15. For blend IV, the Pt dot and line nanostructures are similar in size; however, for blend III, the nanostructures vary. Furthermore, the dot and line nanostructures in Figure 3.15 (b) are different in contrast: one is brighter than the other. This could be because P4VP combined

with metal ions more strongly than P2VP. Still, no direct characterization was able to distinguish PS-*b*-P2VP and PS-*b*-P4VP in the blends.

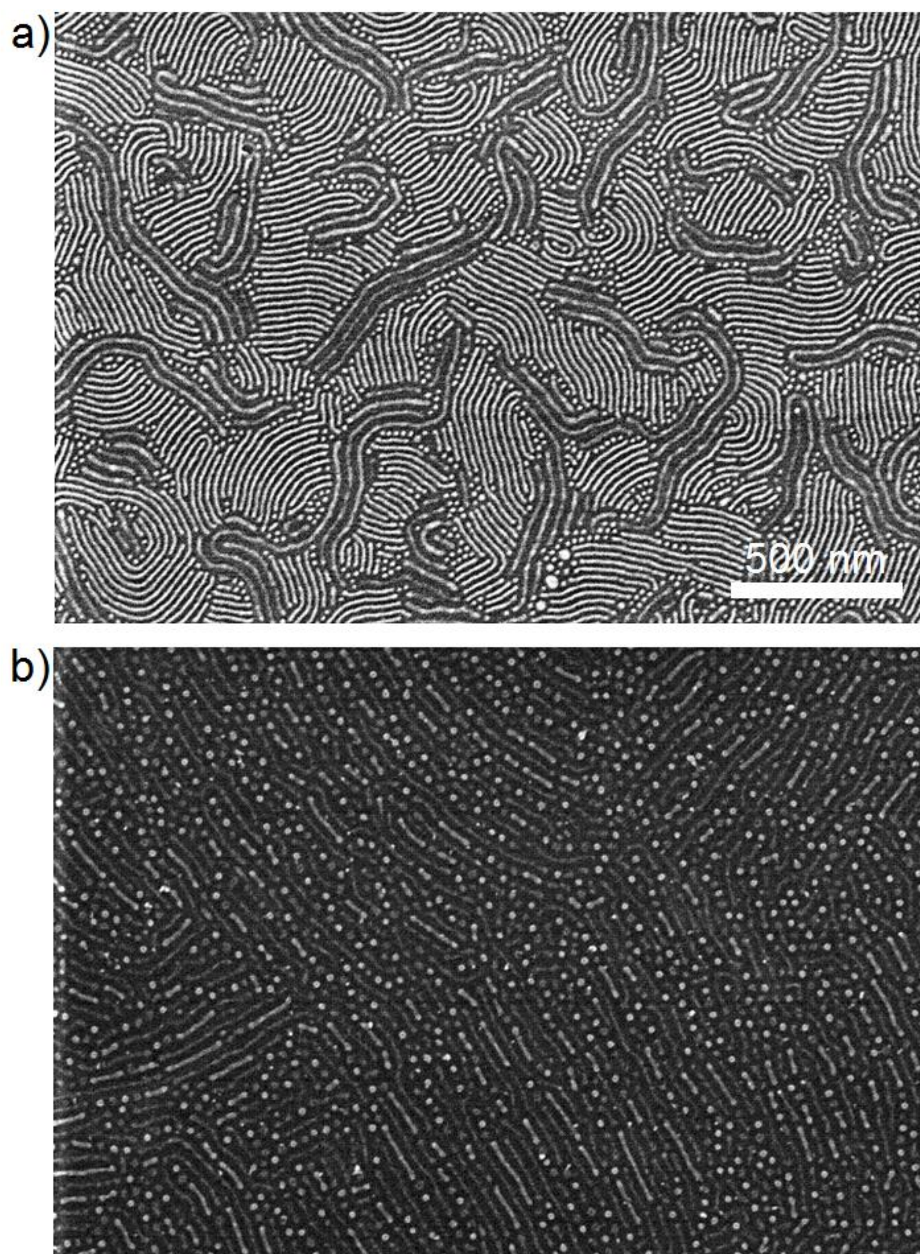

Figure 3.15. SEM images of Pt nanostructures templated by 60 s microwave annealing. (a) Blend III and (b) blend IV.

For the same binary blend, different ordering stages could be achieved by altering the microwave annealing conditions. As shown in Figure 3.16, blend VI was annealed by different microwave power levels over different annealing times. It is clear that more uniform hybrid nanostructures could be achieved with a longer annealing time and higher microwave power.

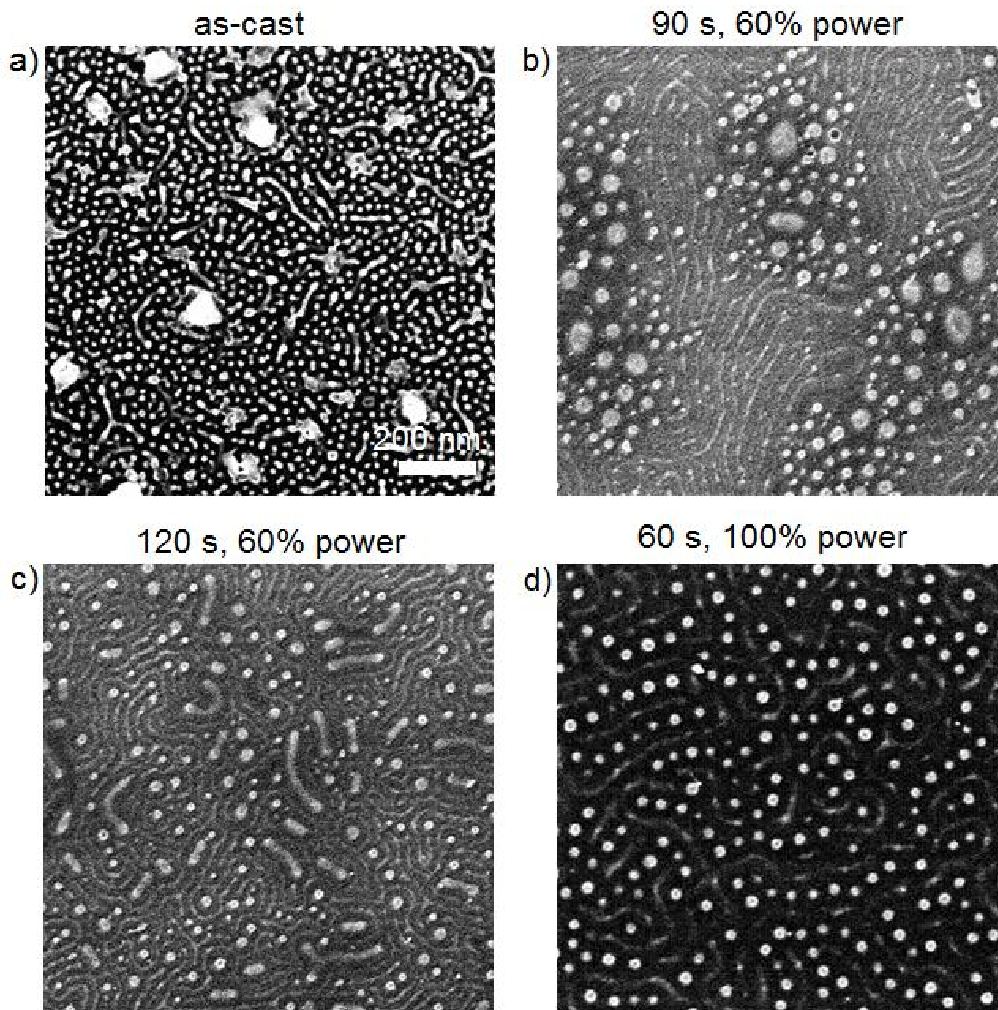

Figure 3.16. SEM images of Pt nanostructures templated by blend VI. (a) As-cast, (b) 90 seconds microwave annealed at 60 % power, (c) 120 seconds microwave annealed at 60 % power, and (d) 60 seconds microwave annealed at maximum power.

Generally, when the two components in the blend naturally form dot or line structures, the hybrid structure is a combination of dots and lines. Other structures besides dots or lines can also be created. For example, in blend I, the PS-*b*-P2VP (17.0k-*b*-9.8k), by itself, formed an inverted array with PS dots in a P2VP matrix when annealed. As a result, the Pt nanostructure templated by the blend had dot/line structures contributed by the P4VP and inverted dots pattern contributed by the P2VP (Figure 3.17).

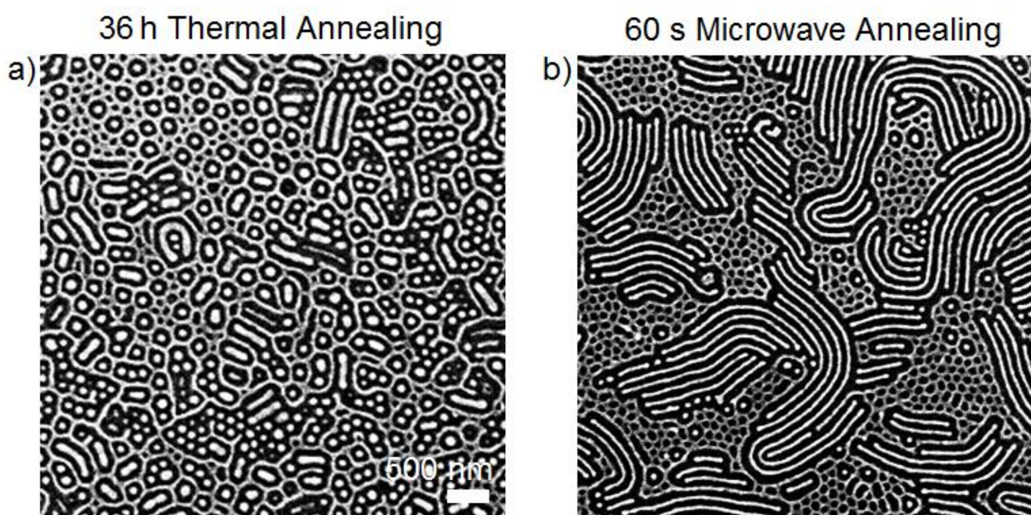

Figure 3.17. SEM images of Pt nanostructures templated by blend I. (a) Thermally annealed for 36 hours; (b) microwave annealed for 60 seconds.

3.3. Conclusions

In this chapter, the strategies for the precise control over linear feature spacing and fabrication of hybrid dot/line nanostructures using binary BCP blends have been discussed. In order to achieve fast assembly of BCPs, an inexpensive household microwave oven was employed. The PS-*b*-P2VP / PS-*b*-P2VP binary

blends provide the ability to control precisely the line feature spacing with relative ease; highly ordered line structures were obtained within 60 seconds in most cases. By changing the ratio of the two components in the blends, feature spacings ranging from 24.8 nm to 42.6 nm were obtained. When PS-*b*-P2VP / PS-*b*-P4VP binary blends were used, hybrid dot and line nanostructures could be achieved on the substrate surface. Although we could not chemically identify the P2VP and P4VP in the annealed blend films at this point, the observation of differences in contrast in the SEM provided important evidence on the identification of the two polymer blocks.

3.4. Experimental Section

Generalities

PS-*b*-P2VP BCPs with molecular weights (g/mol) of 17000-*b*-9800, 23600-*b*-10400, 32500-*b*-12000, 44000-*b*-18500, 50000-*b*-16500, and 125000-*b*-58500 and PS-*b*-P4VP BCPs with molecular weights (g/mol) of 12000-*b*-3200, 31900-*b*-13200, and 47600-*b*-20900 were obtained from Polymer Source, Inc.. Hydrogen peroxide (Fisher, 30%), Sulfuric acid (J. T. Baker, 96.1%), ammonium hydroxide (J. T. Baker, 30%), hydrochloric acid (J. T. Baker, 36.5%), methanol (Fisher, 99.8%), ethanol (Fisher, 99.8%), acetone (Fisher, 99.6%), and toluene (Sigma Aldrich, 99.8%) were used in the preparations. All chemicals and solvents were used as received without further purification. High purity water (18 MΩ·cm, Barnstead Nanopure water) was used throughout all experiments. Silicon wafers were obtained from University Wafer. Unless otherwise noted, all chemicals

were used as received and all the experiments were performed under ambient conditions. Teflon beakers and tweezers were used during the wafer cleaning procedures; glass beakers and plastic tweezers were used during the metallization process.

Silicon Wafer Cleaning

For silicon cleaning, the Prime-grade 4-inch Si (100) wafers (P-type, 10-20 Ω·cm) were first cut into 1 cm by 1 cm pieces then degreased in methanol using an ultrasonic bath. After removal from the ultrasonic bath, the silicon pieces were rinsed in acetone and ethanol, and dried under a nitrogen gas flow. Standard piranha and RCA II procedures were employed to clean the silicon pieces: the pieces were first immersed in a hot piranha solution (H_2SO_4:H_2O_2=3:1, v/v) at 80 °C for 20 minutes; the pieces were removed form the solution, rinsed with water, dried with a stream of nitrogen gas and immersed in an RCA II hot solution which contained 38% HCl, 30% H_2O_2 and Millipore water in a ratio of 1:1:5 at 80 °C for 20 min. After removal from the hot solution, the pieces were again rinsed with excess Millipore water and dried with a stream of nitrogen gas.

Preparation of BCP and Blend Solutions

For homologous BCP solution preparation, the PS-*b*-P2VP BCPs were carefully weighed and dissolved in neat toluene and stirred overnight at room temperature to make 1% w/w and 1.5% w/w solutions. For binary PS-*b*-P2VP / PS-*b*-P2VP blend solution preparation, two 1.5% w/w homologous BCP solutions

were mixed in a ratio of 1:9 to 9:1 and stirred overnight at room temperature. For binary PS-*b*-P2VP / PS-*b*-P4VP blend solution preparation, the PS-*b*-P2VP and PS-*b*-P4VP BCPs were weighed and dissolved in neat toluene and stirred overnight at room temperature.

BCP Self-Assembly on Silicon Substrates

1.5 μL of the BCP or blend solution was dropped onto the cleaned silicon substrates and spin-cast at 4200 rpm for 15 s under an argon environment to form a thin film. For self-assembly of BCPs and binary BCP blends in microwaves, the polymer coated silicon substrates were sealed in a custom made Teflon container with 1 mL THF. The Teflon container was placed in a conventional, household microwave oven (Panasonic Compact Stainless Steel Microwave Oven, NNSD377S, maximum output = 800 W), and heated with the maximum power. The samples were then removed form the Teflon container and cooled in air. **CAUTION:** First, to prevent overheating and damage to either the annealing chamber or microwave oven, annealing times must be limited. This is particularly important for strongly absorbing substrates. Second, in the presence of microwave radiation, electrical arcing and plasma discharge may result from concentrated electric field lines at sharply pointed vertices of silicon substrates or the junction between two substrates, hence substrates with sharp points should be avoided, and multiple substrates must not be placed in close proximity. One incident in our laboratory resulted in damage to the annealing chamber when two substrates were in contact during a 3-minute annealing.

Figure 3.18. Damaged Teflon container. Photograph by Jeffrey N. Murphy, licensed under the Creative Commons Attribution 3.0 Unported (CC BY 3.0) license. [28]

Preparation of Pt Nanostructures Using Annealed BCP Templates

For the fabrication of platinum nanowires, the annealed BCP templates were first immersed in a solution of Na_2PtCl_4 (20 mM) with HCl (1.6%) for 3 hours in a glass vial, removed form the solution, rinsed thoroughly with Millipore water and dried with a stream of nitrogen gas. Oxygen plasma (Harrick Plasma Cleaner/Sterilizer PDC-32G) was applied to the metal salt-loaded samples to reduce $PtCl_4^{2-}$ to Pt (0) and to remove the BCP templates at 0.12 Torr for 1 min.

Formation of Graphoepitaxial Features

See Chapter 2.

Automated Defect Quantification

See Chapter 2.

Feature Spacing Measurement

The linear feature spacing measurement was carried out by Jeffrey Murphy. Image analysis software (ImageJ) was used to automatically measure the spacings. Multiple samples were used for spacing measurement to obtain the average spacings.

3.4. References

(1) Cheng, J.; Ross, C.; Thomas, E.; Smith, H.; Vancso, G. *Appl. Phys. lett.* **2002**, *81*, 3657-3659.

(2) Cheng, J. Y.; Mayes, A. M.; Ross, C. A. *Nat. Mater.* **2004**, *3*, 823-828.

(3) Cheng, J.; Ross, C.; Thomas, E.; Smith, H.; Vancso, G. *Adv. Mater.* **2003**, *15*, 1599-1602.

(4) Bita, I.; Yang, J. K. W.; Jung, Y. S.; Ross, C. A.; Thomas, E. L.; Berggren, K. K. *Science* **2008**, *321*, 939 -943.

(5) Ouk Kim, S.; Solak, H. H.; Stoykovich, M. P.; Ferrier, N. J.; de Pablo, J. J.; Nealey, P. F. *Nature* **2003**, *424*, 411-414.

(6) Ruiz, R.; Kang, H.; Detcheverry, F.; Dobisz, E.; Kercher, D.; Albrecht, T.; de Pablo, J.; Nealey, P. *Science* **2008**, *321*, 936-939.

(7) Yang, X.; Peters, R.; Nealey, P.; Solak, H.; Cerrina, F. *Macromolecules* **2000**, *33*, 9575-9582.

(8) Zhang, X.; Harris, K. D.; Wu, N. L. Y.; Murphy, J. N.; Buriak, J. M. *ACS Nano* **2010**, *4*, 7021-7029.

(9) Hashimoto, T.; Shibayama, M.; Kawai, H. *Macromolecules* **1983**, *16*, 1093-1101.

(10) Kim, H.-C.; Park, S.-M.; Hinsberg, W. D. *Chem. Rev.* **2010**, *110*, 146-177.

(11) Stuen, K. O.; Thomas, C. S.; Liu, G.; Ferrier, N.; Nealey, P. F. *Macromolecules* **2009**, *42*, 5139-5145.

(12) Winey, K. I.; Thomas, E. L.; Fetters, L. J. *Macromolecules* **1991**, *24*, 6182-6188.

(13) Jeong, U.; Ryu, D. Y.; Kim, J. K.; Kim, D. H.; Wu, X.; Russell, T. P. *Macromolecules* **2003**, *36*, 10126-10129.

(14) Peng, J.; Gao, X.; Wei, Y.; Wang, H.; Li, B.; Han, Y. *J. Chem. Phys.* **2005**, *122*, 114706.

(15) Jeong, U.; Kim, H. ‐ C; Rodriguez, R. L.; Tsai, I. Y.; Stafford, C. M.; Kim, J. K.; Hawker, C. J.; Russell, T. P. *Adv. Mater.* **2002**, *14*, 274-276.

(16) Hadziioannou, G.; Skoulios, A. *Macromolecules* **1982**, *15*, 267-271.

(17) Parnell, A. J.; Pryke, A.; Mykhaylyk, O. O.; Howse, J. R.; Adawi, A. M.; Terrill, N. J.; Fairclough, J. P. A. *Soft Matter* **2011**, *7*, 3721-3725.

(18) Pu, G.; Luo, Y.; Wang, A.; Li, B. *Macromolecules* **2011**, *44*, 2934-2943.

(19) Mickiewicz, R. A.; Ntoukas, E.; Avgeropoulos, A.; Thomas, E. L. *Macromolecules* **2008**, *41*, 5785-5792.

(20) Hsu, C.-H.; Kuo, S.-W.; Chen, J.-K.; Ko, F.-H.; Liao, C.-S.; Chang, F.-C. *Langmuir* **2008**, *24*, 7727-7734.

(21) Yamaguchi, D.; Hashimoto, T. *Macromolecules* **2001**, *34*, 6495-6505.

(22) Court, F.; Hashimoto, T. *Macromolecules* **2001**, *34*, 2536-2545.

(23) Jeon, H. G.; Hudson, S. D.; Ishida, H.; Smith, S. D. *Macromolecules* **1999**, *32*, 1803-1808.

(24) Sakurai, S.; Irie, H.; Umeda, H.; Nomura, S.; Lee, H. H.; Kim, J. K. *Macromolecules* **1998**, *31*, 336-343.

(25) Kane, L.; Satkowski, M. M.; Smith, S. D.; Spontak, R. J. *Macromolecules* **1996**, *29*, 8862-8870.

(26) Spontak, R. J.; Fung, J. C.; Braunfeld, M. B.; Sedat, J. W.; Agard, D. A.; Kane, L.; Smith, S. D.; Satkowski, M. M.; Ashraf, A.; Hajduk, D. A.; Gruner, S. M. *Macromolecules* **1996**, *29*, 4494-4507.

(27) Chen, Y.; Wang, Z.; Gong, Y.; Huang, H.; He, T. *J. Phys. Chem. B* **2006**, *110*, 1647-1655.

(28) http://creativecommons.org/licenses/by/3.0/.

(29) Bang, J.; Jeong, U.; Ryu, D. Y.; Russell, T. P.; Hawker, C. J. *Adv. Mater.* **2009**, *21*, 4769-4792.

Chapter 4
Selective Fabrication of Ordered Titania Nanostructures on Etched Silicon Surfaces Using BCP Thin Films as Templates

4.1. Introduction

In this work, Dr. Yinghong Qiao shared her knowledge of silicon etching using BCP thin films as masks and galvanic displacement on etching silicon surfaces. Dr. Lina Xu contributed to discussions about gold deposition on titania.

In BCP nanolithography, the domain structures in BCP thin films provide a variety of templates for pattern transfer operations, either additive or subtractive.[1–3] Ordered metal nanostructure patterns templated by BCPs were described in Chapters 2 and 3. This chapter focuses on constructing quasi-hexagonally packed metal-based nanostructures on silicon surfaces where highly ordered etched pits were obtained by using BCP thin films as masks.[4]

The fabrication of three-dimensional nanoscale pits on silicon surfaces based on an etching technique developed in the Buriak Group is described in the first part of this chapter. In brief, nanoscale pit arrays were achieved by etching BCP PS-*b*-P4VP (109k-*b*-27k)-coated silicon substrates using aqueous based fluoride etchants. The latter part of this chapter then demonstrates the production of both titania and gold nanofeatures using the resulting etched pits. In the first approach, we demonstrated an efficient way to deposit titania exclusively inside pits etched into silicon wafers via the hydrolysis of $TiCl_4$. We chose titania because titania nanostructures are being explored actively for a great variety of applications,

including photocatalysis, solar cells, sensors, optical materials, superhydrophobic and superhydrophilic materials, and lithium-ion batteries.[5–13] In the second approach, gold nanoparticles were deposited on the titania nanobowls. The titania nanobowls could also be released from the surfaces by further HF etching.

Nanopatterning of Titania Using BCP Thin Films as Templates

Nanopatterning on semiconductor surfaces has been the focus of much attention due to its practical applications in sensors, catalysis, electronics, interfacing with objects of biological origin, and many others.[14–19] BCP thin films are ideal template materials for self-assembly-based nanopatterning for several reasons: (1) BCP lithography is considerably cheaper than EBL to fabricate nanoscale features; (2) the nanoscopic structures and domain sizes of BCPs are readily tunable; and (3) mass production is possible.[14,20,21] Many researchers have focused on developing new approaches to utilize BCP self-assembly for patterning semiconducting materials.[1,22–26]

One important semiconductor material in particular, titanium dioxide, has been used extensively due to its superb performance in photovoltaic and photocatalytic applications.[27,28] For these applications, the size, shape, phase, and arrangement of titanium dioxide nanostructures are critically important. Thus, it is desirable to pattern titanium dioxide on substrates in a relatively simple, efficient, and controllable process. For example, Shipp and coworkers demonstrated a convenient way of fabricating periodic titania nanostructures on silicon and ITO substrates using a PS-*b*-P4VP BCP as the template.[29] As shown

in Figure 4.1, first, the PS-*b*-P4VP BCP was spin-coated on the substrates and annealed to form a morphology that consisted of perpendicular P4VP cylinders to the substrates surrounded by PS matrix. The film was then exposed to diiodobutane (DIB) in order to cross-link the P4VP domains. Finally, a sol-gel titania precursor, titanium(IV) bis(ammonium lactate) dihydroxide (TALH), was used to form titania exclusively in the P4VP phase.

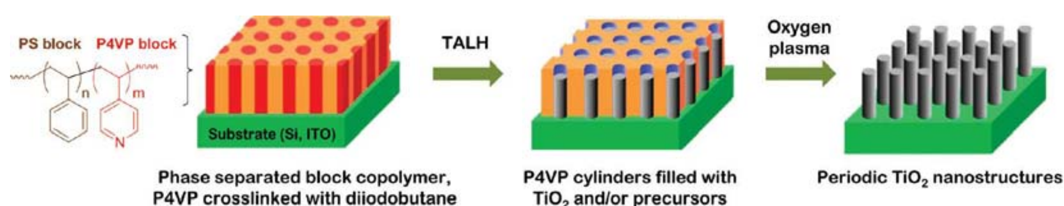

Figure 4.1. Outline of the preparation of titania nanostructures using PS-*b*-P4VP BCP templates. Reprinted with permission from ref. 29. Copyright © 2010 American Chemical Society

BCPs can be used to direct the formation of titania mesostructures. Chmelka and coworkers demonstrated the fabrication of well-ordered mesoporous titania films utilizing poly(ethylene oxide)-poly(propylene oxide)-poly(ethylene oxide) (PEO-PPO-PEO) triblock copolymer species as the templates (Figure 4.2).[30] Cubic and hexagonal structured titania thin films were obtained by tuning the volume ratio between the inorganic components of the precursor solution and BCP. Sanchez and coworkers showed another example of using BCP thin films as the templates to fabricate highly crystalline cubic mesoporous titania. In their work, the hydrolysis of titanium precursor, $TiCl_4$, was applied in the presence of BCP templates to deposit titania.[31]

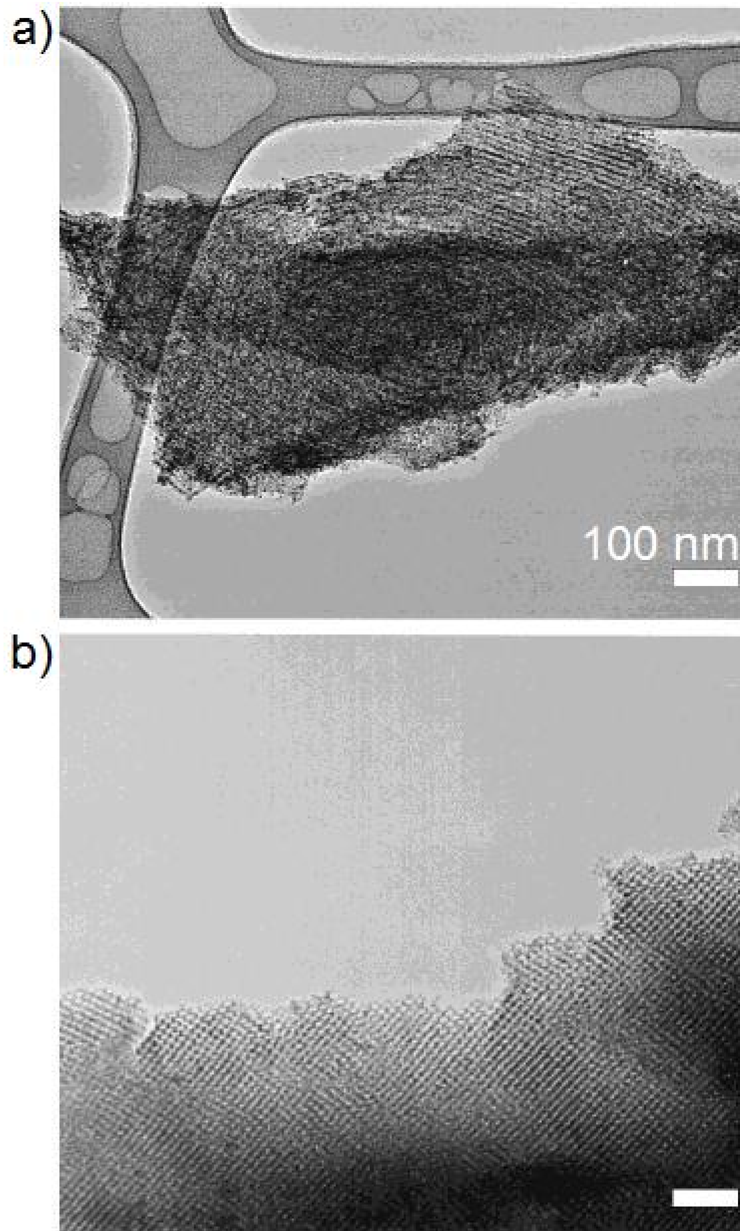

Figure 4.2. (a) Plan view TEM image of a hexagonal mesostructured titania film tempalted by BCPs. (b) Plan view image of a cubic mesostructured titania film. Reprinted with permission from ref. 30. Copyright © 2002 American Chemical Society.

4.2. Results and Discussion

Silicon Etching Using BCPs as Soft Masks

The commercially available amphiphilic diblock copolymer, polystyrene-*block*-poly(4-vinyl pyridine) (PS-*b*-P4VP) was used as a soft mask to generate nanoscale etching patterns on silicon substrates. PS-*b*-P4VP (M_n = 109k-*b*-27k) was used to form etch pits with an average diameter of 55 nm on silicon substrates. The BCP was transferred from a toluene solution onto the silicon surfaces by spin-coating (see Chapter 2) to form thin films of self-assembled quasi-hexagonally close-packed arrays of BCP micelles with PS shells and P4VP micellar cores (Figure 4.3).

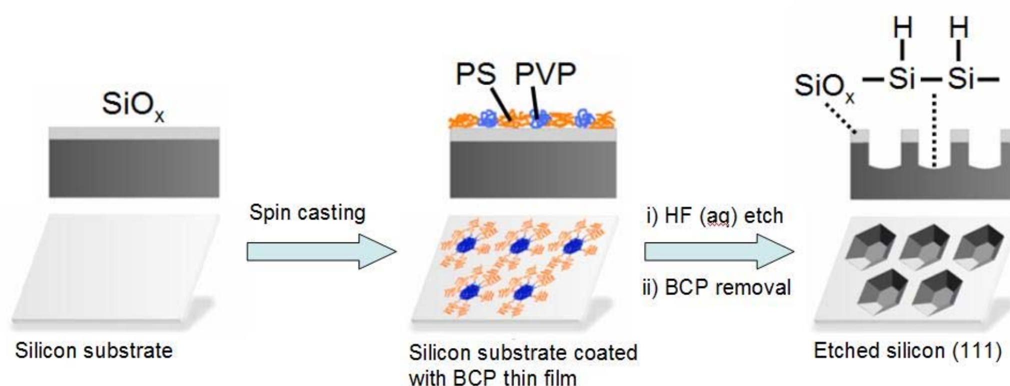

Figure 4.3. Outline of selective etching on Si(111) surface to produce a quasi-hexagonal pit array. Reprinted with permission from ref. 4. Copyright © 2011 American Chemical Society.

The BCP used in these experiments formed hexagonally packed micelles with a center-to-center spacing of 110 nm on the silicon surface. However, the spacing

could be easily adjustable from 16 to 290 nm by simply tuning the molecular weight of the BCP. [32–36] When immersed in a dilute aqueous HF solution (w/w=0.01 %) for a given time, the pyridyl groups in PS-*b*-P4VP become protonated by HF to form poly(pyridinium) fluoride, which selectively etches the silicon directly underneath the pyridyl cores.[37] The resulting etched pits are completely H-terminated while the region outside the pits remains unetched and covered with the native oxide layer which was protected from the HF etching solution by the PS matrix in the copolymer film.

According to previous work in the Buriak Group, the shape, size, and morphology of the etching pits can be well controlled by altering the etching conditions, such as etching time, type of BCP, and silicon wafer orientation.[37] Si (111) was chosen for forming hexagonal pits because of the short etching time to get uniformly sized and shaped pits on Si (111). The plan view and cross section SEM images of the freshly etched silicon surface are shown in Figure 4.4. that displays the hexagonally shaped pits on an Si (111) wafer surface with etch pit depths of ~45 nm and center-to-center pit separation of ~100 nm.

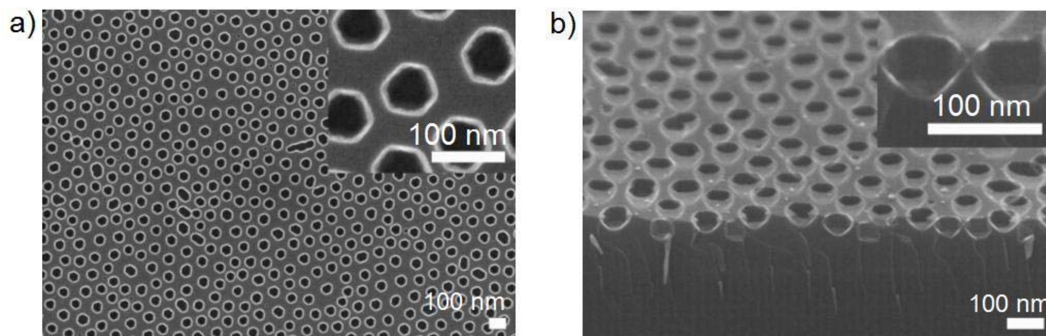

Figure 4.4. SEM images of etched Si(111) substrates. (a) Plan view and (b) tilted.

Formation of Titania Nanobowls

Self-assembling domain structures in BCP thin films have been the focus of much attention as a means to pattern oxide and semiconductor materials such as Al_2O_3, TiO_2, and SiO_2.[38–41] In the case of TiO_2, applications that include photovoltaics, sensors, catalysis,[5,42–45] biomedical applications of silicon/titania micro- and nanopatterns are of great interest.[46–49] Here the etched silicon surfaces were used as templates to fabricate periodic titania nanostructures.[50–54]

The deposition of titania was carried out with the use of liquid $TiCl_4$, a commonly used titanium precursor. The experimental setup is shown in Figure 4.5. A three-neck flask was used as the reaction container to grow titania on the etched silicon substrates. The flask was connected to a $TiCl_4$ source and a vacuum pump. After the sample was transferred into the flask, a rough vacuum was applied and the sample was then exposed to $TiCl_4$ vapor for a given time. The brief exposure of the etched silicon substrates to $TiCl_4$ (g) led to the formation of amorphous titania on the silicon surface.[55]

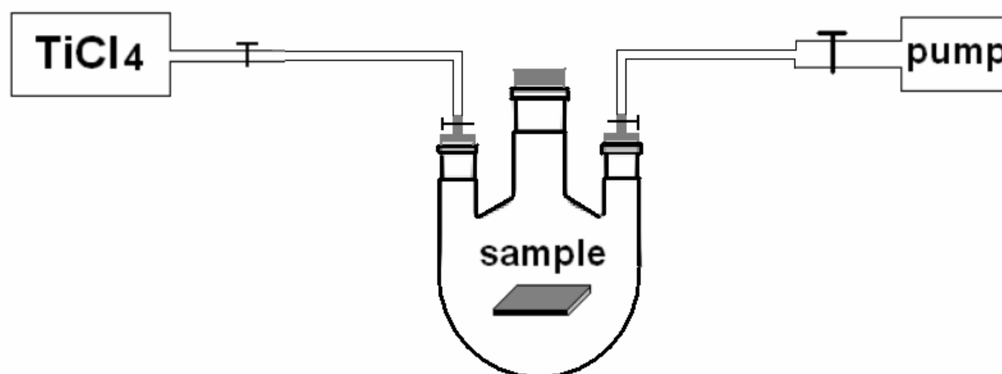

Figure 4.5. Scheme of experimental setup for titania deposition. The sample is placed in a three-neck flask which was connected to a $TiCl_4$ source and a vacuum pump.

To clarify, the pit interiors on the silicon surface after HF etching and removal of the PS-b-P4VP were terminated by Si-H_x groups, and the top face of the silicon shard remained capped by the native oxide, as illustrated schematically in Figure 4.3. To deposit titania exclusively inside the etched pits, the sample was first immersed in a 1.3 mM solution of octadecyltrichlorosilane (OTS) in dry hexanes for 30 minutes at room temperature, which resulted in selective silanization on the top native oxide region of the substrate and formed a hydrophobic monolayer on the surface (Figure 4.6).[56–59] The water contact angle was measured to be 110.5^o, which suggested that the substrate had a high surface hydrophobicity. As controls, the water angles for the cleaned Si(111) substrate and the as-etched silicon substrate were measured to be 17° and 50°, respectively. The silanized silicon substrate was then immersed in hydrogen peroxide (aq) [30% (w/w)] overnight to oxidize the Si-H_x terminated interfaces within the etched pit interiors, producing a measured water contact angle of ~90º. The significant decrease in contact angles after H_2O_2 oxidation suggests that the wafer surfaces were Si-OH rich.[60,61] According to the literature, we expected that the insulating organic monolayer formed in the previous silanization to be stable during this oxidation condition.[62,63] As water is required in the hydrolysis of $TiCl_4$, after removal from the H_2O_2 oxidation solution, the silicon substrates were dried in air, and no attempt was made to dry them further (e.g. under vacuum). Since the pits region was hydrophilic and H_2O was present, a Ti-O-Ti network formed on the silica surfaces when $TiCl_4$ vapor was added to the system.[64–67]

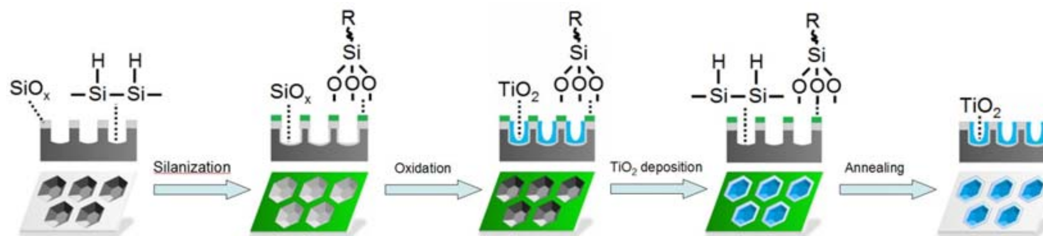

Figure 4.6. Outline for titania deposition exclusively in the etched pit regions. Etched silicon samples were first exposed to OTS to realize selective silanization of the native oxide. The samples were then immersed in a hydrogen peroxide solution to oxidize the Si-H_x-terminated interfaces within the pore interiors. Titania nanobowls were fabricated exclusively inside the etched pits after titania deposition. Reprinted with permission from ref. 4. Copyright © 2011 American Chemical Society.

Amorphous titania was obtained on the silicon surface after this deposition. An annealing procedure was then used to form anatase titania and to remove the residual carbon-based polymers and the alkyl chains on the substrate surface by rinsing with water, drying in nitrogen gas and annealing at 550 ºC in air for 3 hours.[68,69] The SEM and X-ray diffraction (XRD) patterns of the titania nanobowls on silicon surfaces before and after thermal annealing are presented in Figure 4.7. The XRD patterns confirmed the transformation of amorphous titania to anatase titania during calcination as diffraction peaks for anatase titania and silicon were detected on the calcined sample, whereas only the diffraction peaks for silicon were detected on the as-prepared sample.

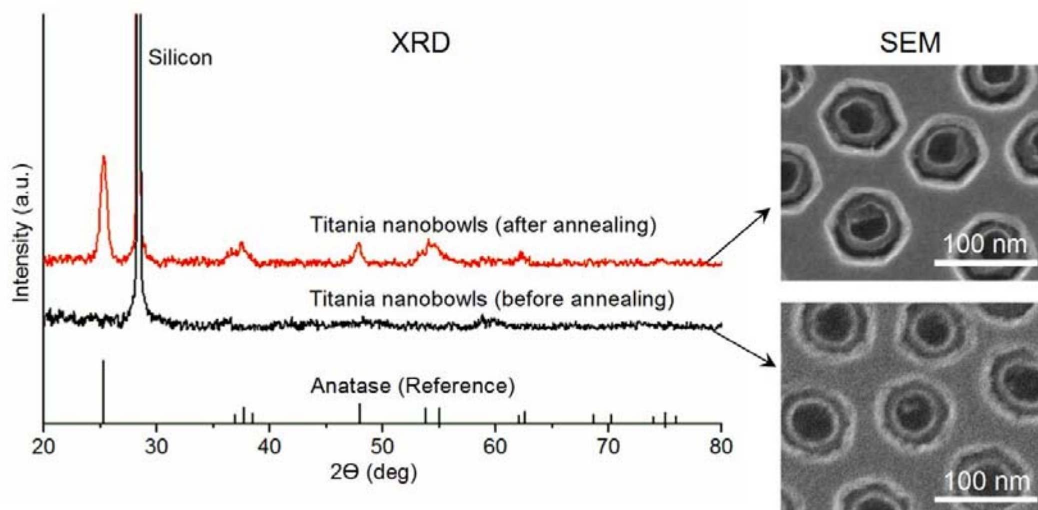

Figure 4.7. X-ray diffraction (XRD) patterns of titania nanobowls prepared by hydrolysis of $TiCl_4$ on silicon surfaces (black) and titania nanobowls annealed at 550 ºC in air for 3 hours (red). According to the XRD pattern, the titania nanobowls on etched silicon surfaces before annealing in air are amorphous. The peaks on the pattern of the annealed titania nanobowls correspond to anatase. Reprinted with permission from ref. 4. Copyright © 2011 American Chemical Society.

The SEM images shown in Figure 4.8. reveal the structures of the titania nanobowls formed on etched silicon surfaces. Figure 4.8 shows typical plan views (a and b) and side views (c-f) of titania nanobowls with typical dimensions averaging 55 ± 5 nm for the outer diameter (average of 40 measurements), and ~40 nm for the inner diameter, and ~40 nm for the height. An average diameter of the inner hole and of the height could not be determined as these dimensions were subject to a certain degree of irregularity. We noticed that the tops of these titania nanobowls were several nanometers lower than the level of the silicon surface, as shown in the side view SEM images.

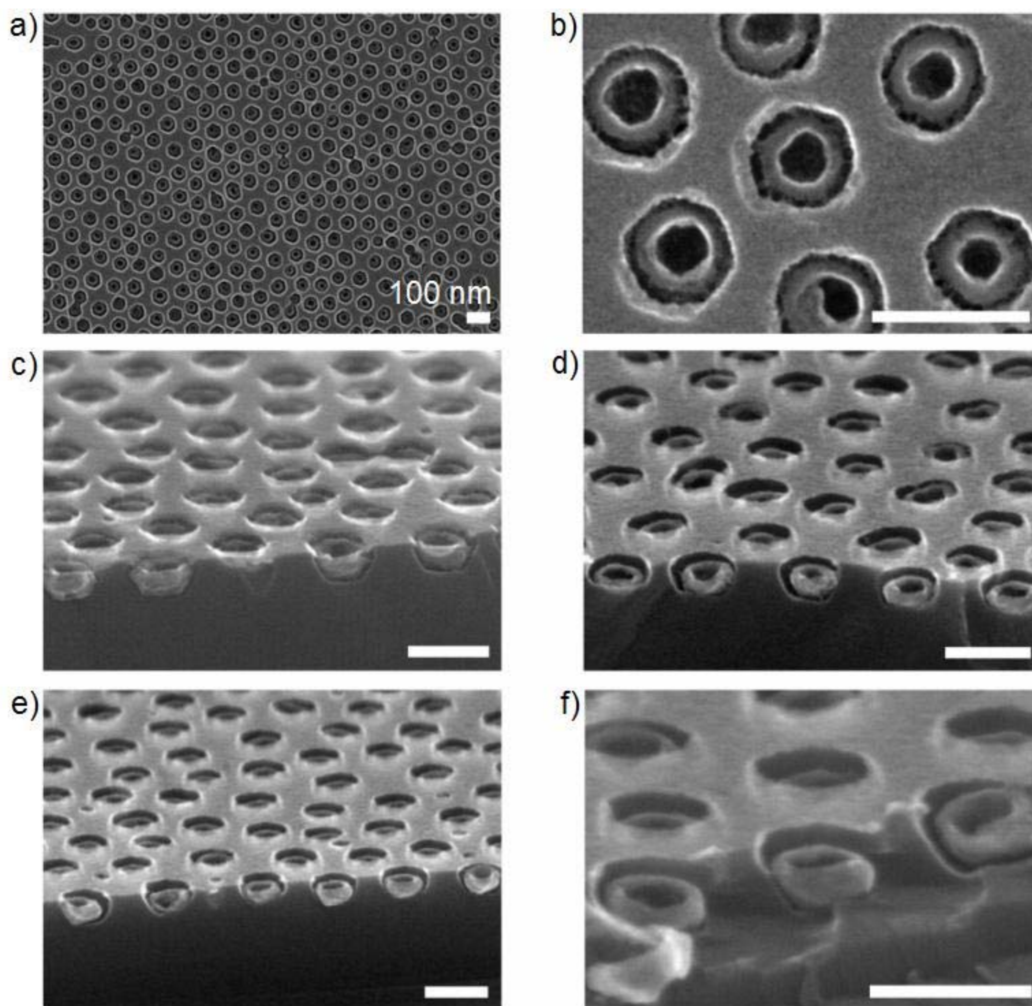

Figure 4.8. SEM images of titania nanobowls formed on etched silicon surfaces. (a) and (b) plan view, (c)-(f) side view.

Furthermore, to confirm the success of titania loading, ~10 nm resolution scanning Auger microscopy (SAM) was used to identify the elements of the titania-loaded silicon substrates. The Ti LMM and Si KLL SAM images of the sample are shown in Figure 4.9 (b) and (c), respectively.

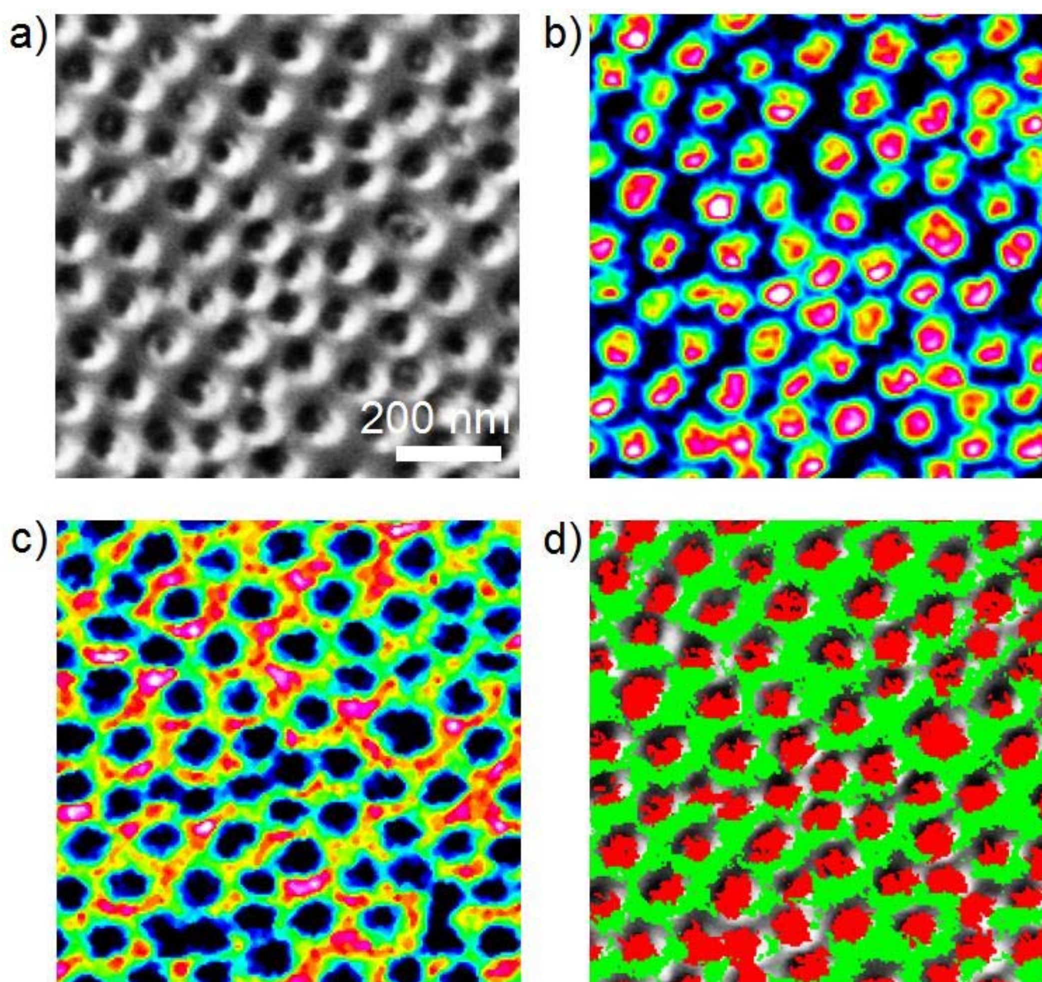

Figure 4.9. Scanning Auger microscopy (SAM) mapping of titania nanobowls on silicon, (a) SEM image, (b) Ti LMM SAM, (c) Si KLL SAM, and (d) Ti LMM (red) and Si KLL (green) intensities overlaid on (a). Reprinted with permission from ref. 4. Copyright © 2011 American Chemical Society.

The shape of the titania nanobowls was controlled by altering the deposition time. Longer deposition times led to thicker titania nanostructures. As shown in the SEM images of Figure 4.10 and 4.11, the deposition time was 120 s and 1200 s, respectively. The SAM images show that titania was deposited inside the pit interiors in both cases.

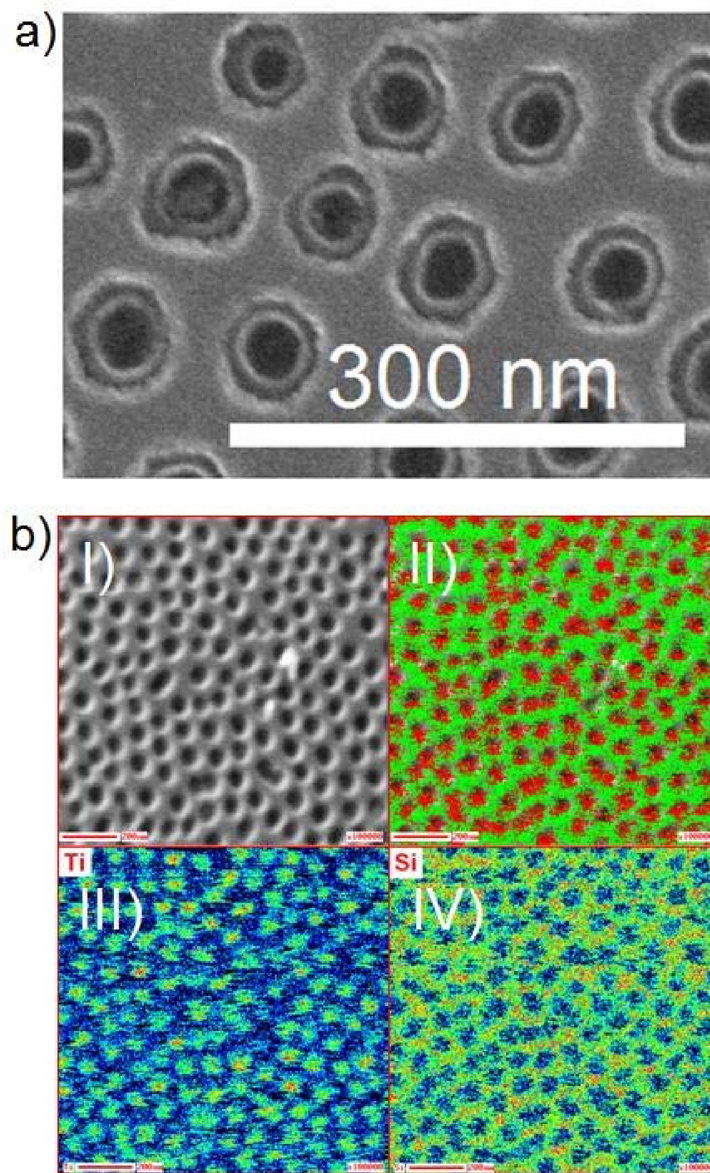

Figure 4.10. (a) SEM images and (b) scanning Auger microscopy (SAM) of titania nanobowls on etched silicon surfaces: (I) SEM, (II) Ti LMM (red) and Si KLL (green) intensities overlaid on (I), (III) Ti LMM SAM, and (IV) Si KLL SAM. The titania deposition lasted for 120 s.

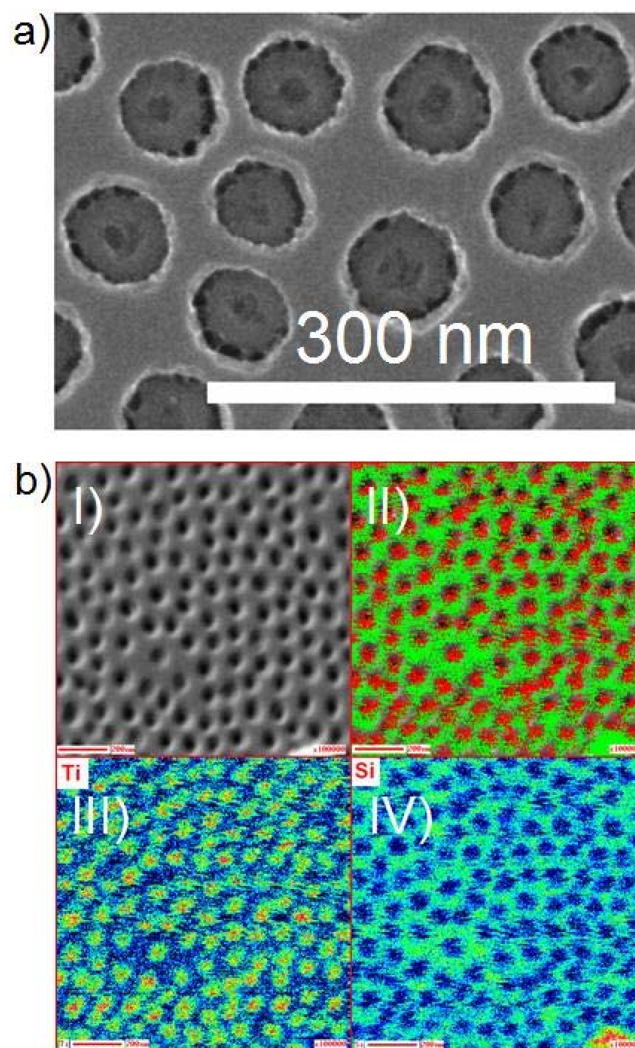

Figure 4.11. (a) SEM images and (b) scanning Auger microscopy (SAM) of titania nanobowls on etched silicon surfaces: (I) SEM, (II) Ti LMM (red) and Si KLL (green) intensities overlaid on (I), (III) Ti LMM SAM, and (IV) Si KLL SAM. The titania deposition lasted for 1200 s.

The Role of H_2O_2 Oxidation Step in the Deposition of Titania

In addition, to better understand the surface chemistry of the pore interiors, we studied the H_2O_2 oxidation step, but reduced the exposure time. The silanized silicon (111) substrate was oxidized in 30% (w/w) H_2O_2 solution for only 20

minutes instead of 12 hours at room temperature before being used in the titania deposition. The surface of the sample was further characterized by SEM and SAM. Figure 4.12 (a) shows the SEM image of the sample; no titania nanobowls were observed inside the pits. Figure 4.12 (b) shows the Auger maps of silicon and titania on the sample. These results point to a poor deposition of titania because the conversion of the Si-H_x pit interiors to a more hydrophilic Si-OH termination would not be expected to be completed due to the reduced H_2O_2 exposure time.

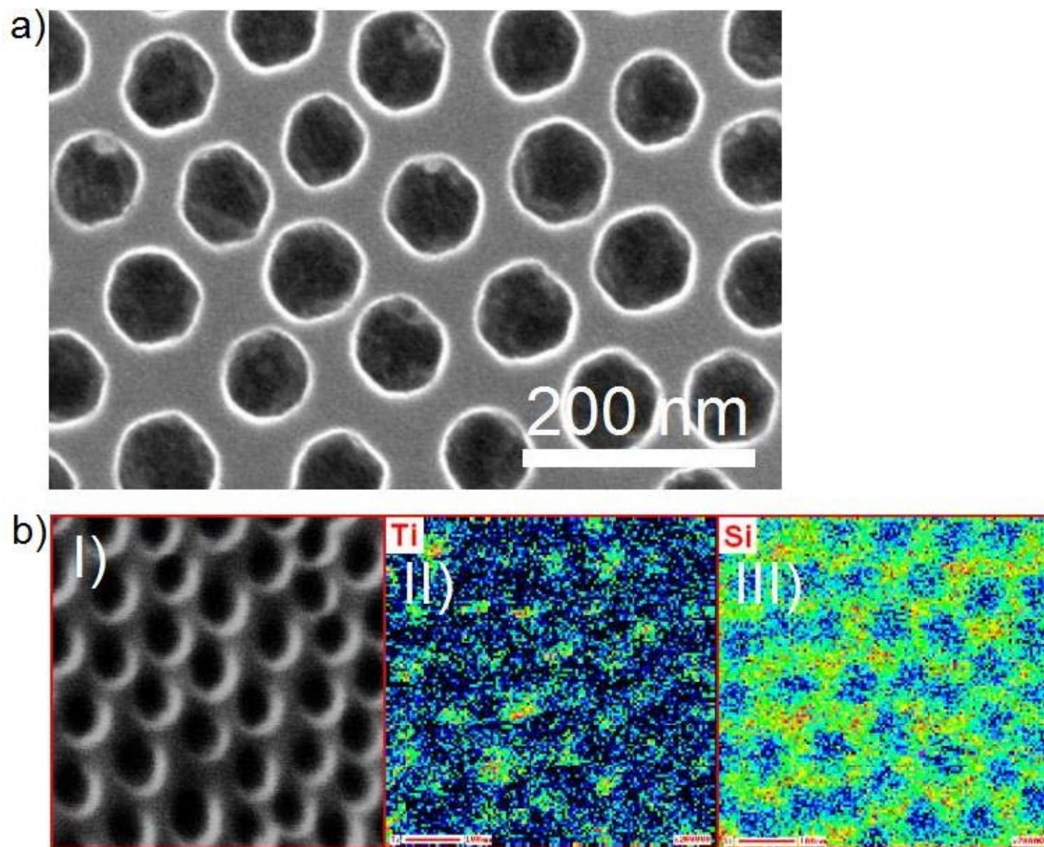

Figure 4.12. (a) SEM image of etched silicon surface after titania deposition in which the oxidation time was 20 minutes. (b) Scanning Auger microscopy (SAM) images of the sample: (I) SEM image, (II) Ti LMM SAM, and (III) Si KLL SAM.

Formation of Continuous Titania Films

Two control experiments, illustrated in Figures 4.13 and 4.14, were employed to further confirm that the self-assembled OTS monolayer was critical in the preferential deposition of titania on the hybrid hydrophilic/hydrophobic silicon surfaces. In one experiment, after exposure to $TiCl_4$(g), a continuous titania film was obtained on a freshly etched and fully oxidized [by 30% (w/w) hydrogen peroxide, overnight] silicon surface; no OTS treatment was carried out after HF(aq) etching. A film formed on the top surface instead of the nanobowl interiors following the hydrogen peroxide treatment and was due to the fact that the entire surface would be expected to be terminated by hydroxyl groups that have good affinity for the titania precursors. During gas-phase hydrolysis of $TiCl_4$ (g), a continuous thin film formed over the entire surface. Inspection of the cross-section SEM image in Figure 4.14 reveals that the titania thin film that covered the entire wafer had a thickness of ~20 nm.

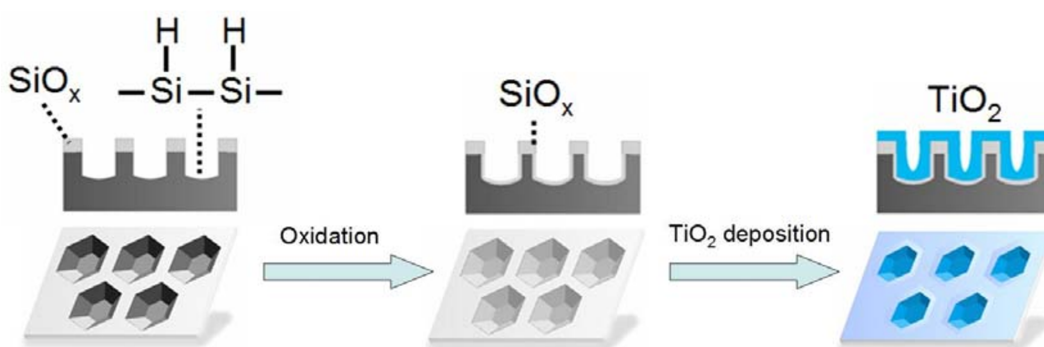

Figure 4.13. Formation of titania thin films on etched silicon surface. The freshly etched silicon surface was oxidized so that the entire surface was terminated by hydroxyl groups. A continuous film formed over the entire surface after titania deposition. Reprinted with permission from ref. 4. Copyright © 2011 American Chemical Society

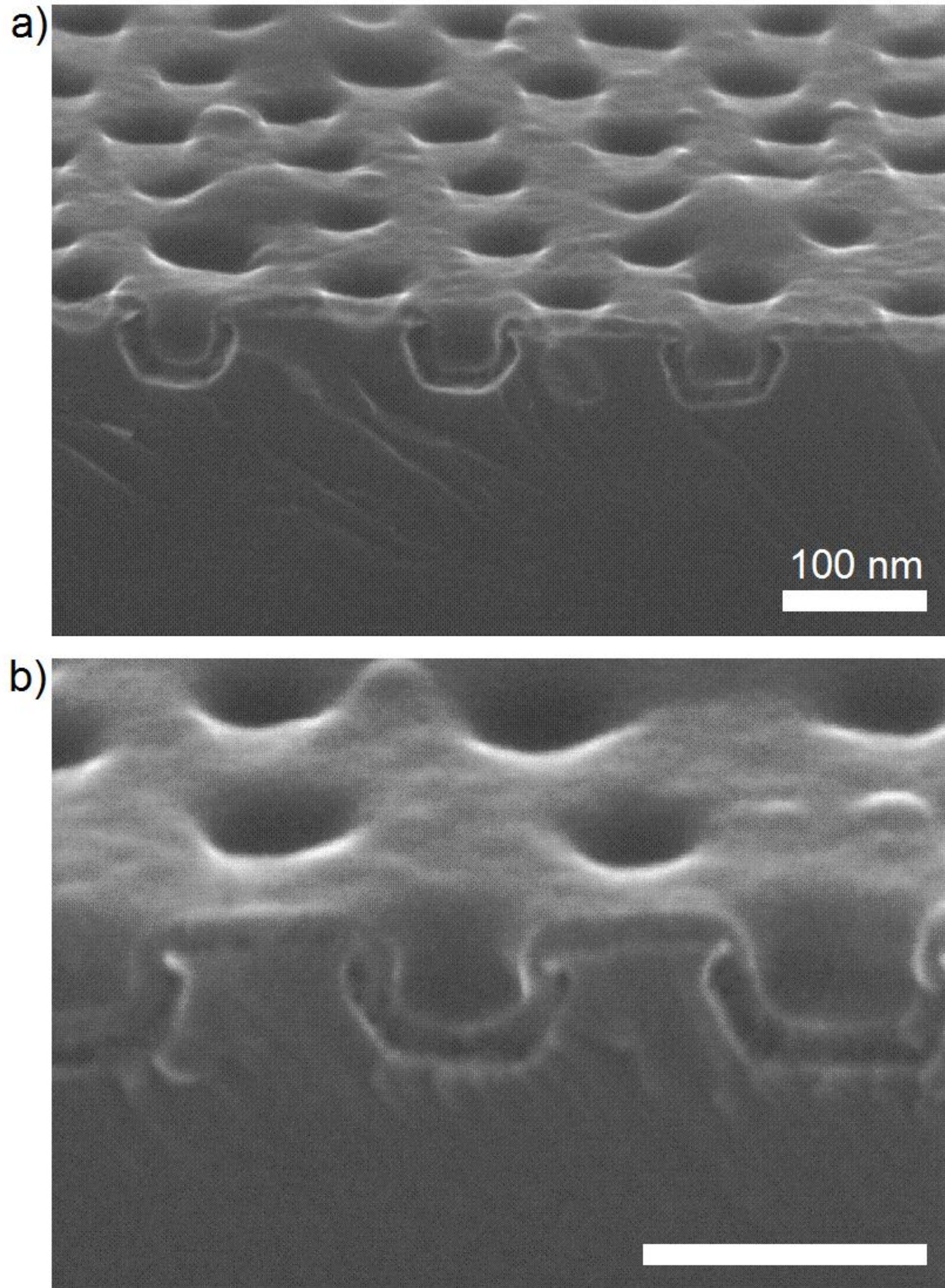

Figure 4.14. SEM images of titania films formed over the entire etched surface followed by full oxidation by 30% (w/w) hydrogen peroxide treatment after HF etching.

In the second control experiment, the freshly etched Si(111) substrate was used directly in the titania deposition, as shown in Figure 4.15. Since the etched

pit interiors on the substrate were H-terminated, the titania grew on the silicon native oxide and no titania was observed inside the etched pits (Figure 4.16).

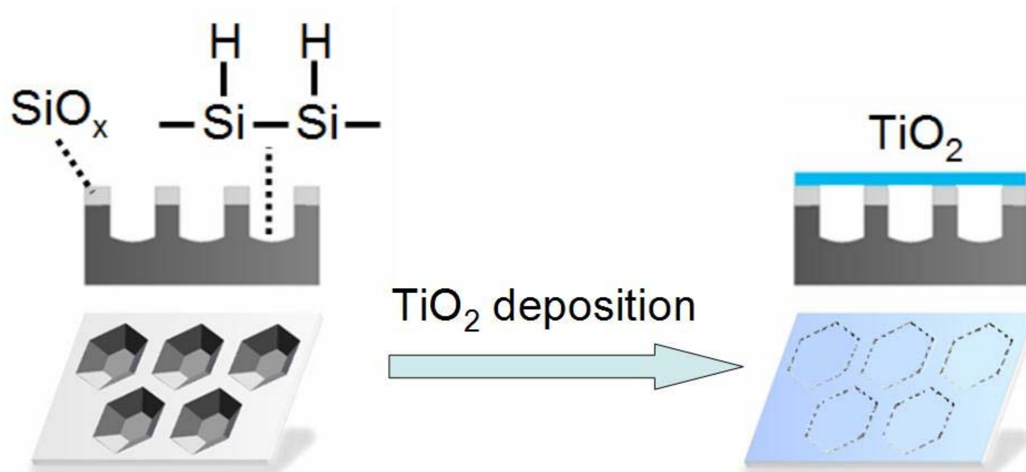

Figure 4.15. Outline of formation of titania thin films on an etched Si(111) surface. The as-etched silicon substrate was used directly in the titania deposition and titania film only covered on the native oxide surface. Reprinted with permission from ref. 4. Copyright © 2011 American Chemical Society.

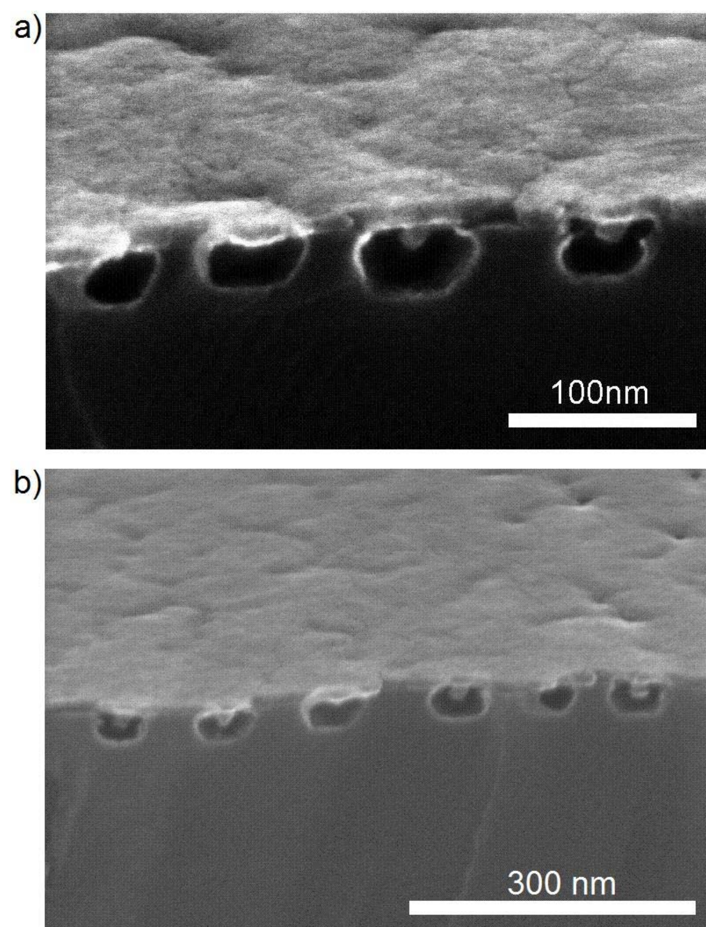

Figure 4.16. (a) and (b) Tilted SEM images of titania films formed exclusively on the silicon native oxide interface.

Release of the Titania Nanobowls

In order to better analyze the shape and morphology of the titania nanobowls. a dilute HF (aq) (0.02%, w/w) solution was used to release the titania nanobowls from the surface by etching the silicon substrate for 6 hours. The dilute solutions were necessary because titania can also be dissolved in HF (aq) or fluoride-containing solutions to form soluble $[TiF_6]^{2-}$ complexes.[70] With a brief exposure to a dilute HF solution, however, the titania nanostructures remain intact.[71] The etching was carefully carried out until the titania nanobowls were almost entirely

freed from the silicon surface. In this manner, the structures could be better reviewed by SEM in different configurations, including plan view, side view and bottom view. The SEM images in Figure 4.17 and 4.18 reveal that the titania that grew inside the etched silicon pits apparently has a continuous bowl structure, including the bottom. As shown in Figure 4.19, most of the nanobowls were removed in samples that were ultra-sonicated in water for 3 minutes.

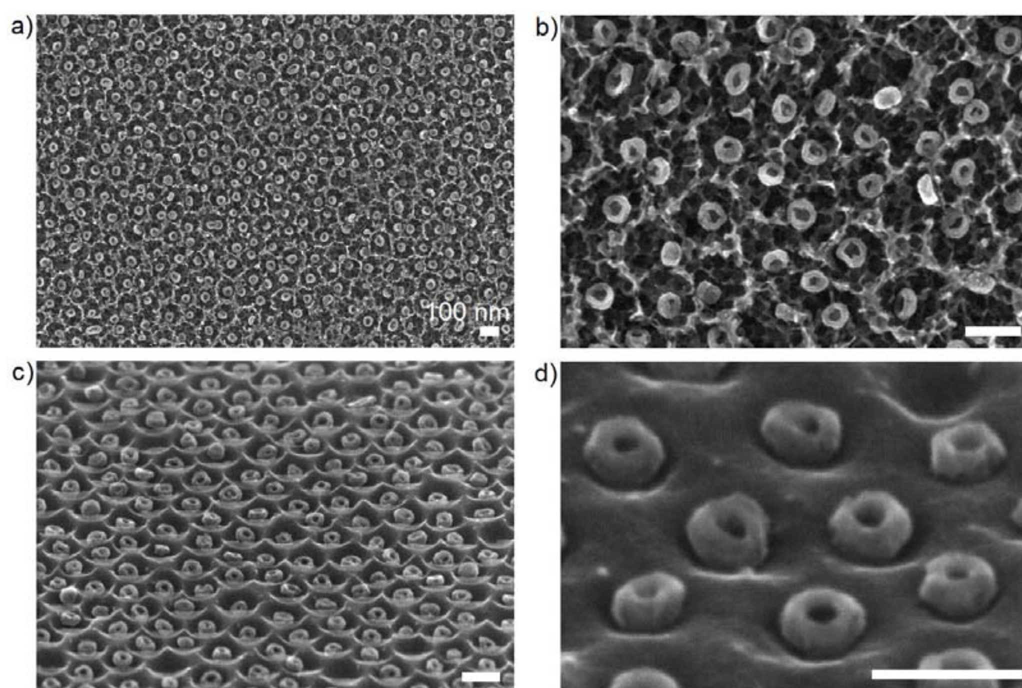

Figure 4.17. Plan view and tilted SEM images of titania nanobowls on etched Si(111) surfaces released through exposure to dilute HF (aq).

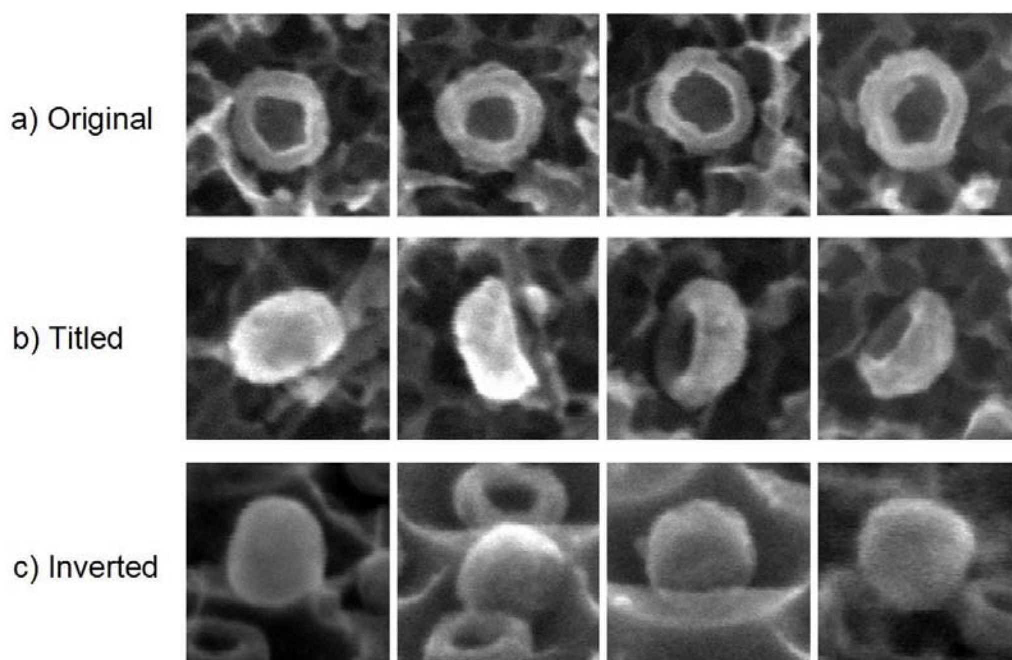

Figure 4.18. SEM images of released titania nanobowls in various orientations on etched Si(111) surfaces. Reprinted with permission from ref. 4. Copyright © 2011 American Chemical Society

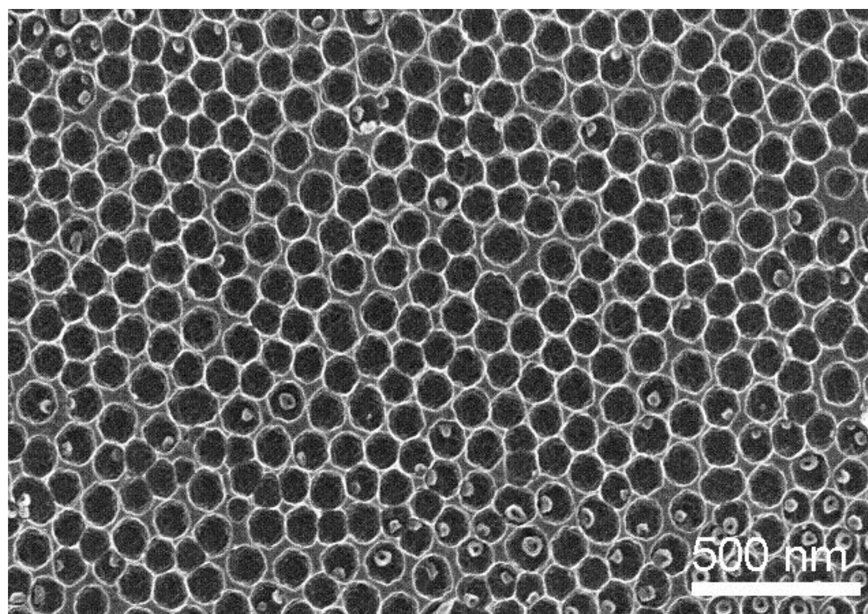

Figure 4.19. SEM image of released titania nanobowls on silicon surface after 3 min ultra-sonication in water.

In a study of the HF etching, a higher concentration of HF (aq) was compared with the low concentration. When 5% HF (aq)was used to etch the silicon substrate for a shorter time (10 min), obvious damage to the titania nanobowls was observed, as shown in Figure 4.20.

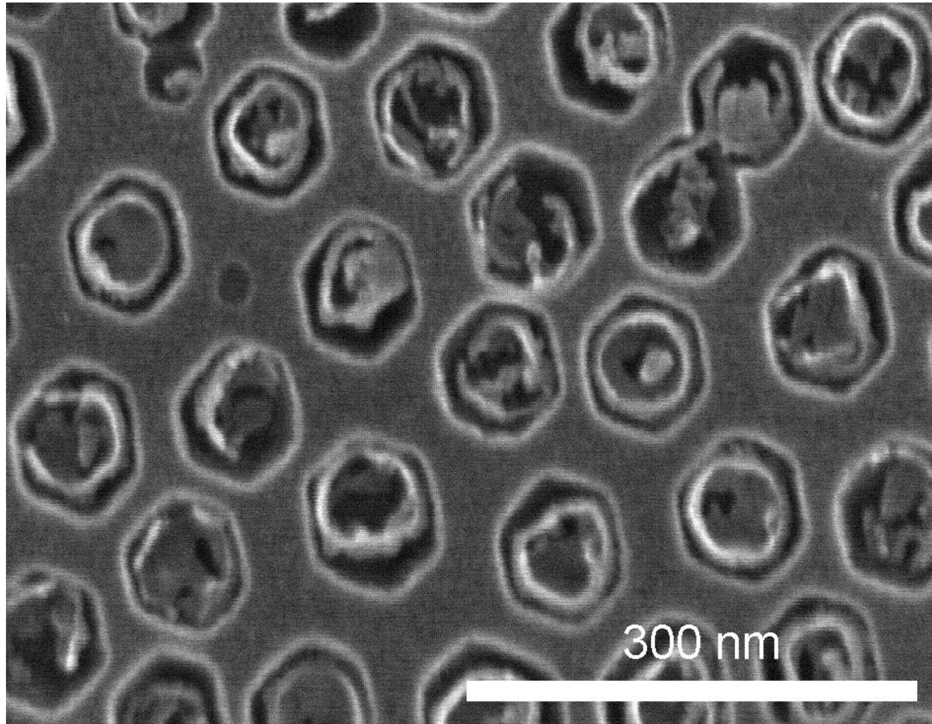

Figure 4.20. SEM images of damaged titania nanobowls on silicon surfaces after 10 minutes etching with a 5% HF (aq) solution.

Gold Deposition on Titania Nanobowls

A UV light-induced reduction of gold salts was carried out to enable gold photodeposition on titania nanobowls. Gold nanoparticles were deposited exclusively on titania by using an aqueous 5×10^{-5} M $HAuCl_4$ solution that had been neutralized to pH 7 with a 10^{-3} M KOH solution. The titania nanobowl

samples were directly immersed in the gold salt solution and after a 5 min application of 254 nm UV from a 5 W screen inspection UV lamp, gold nanoparticles with a diameter of less than 4 nm were observed on the titania nanobowls but not on silica surfaces. During the photodeposition process, the photogenerated electrons on titania surfaces reduce Au(3+) to Au(0); meanwhile the photogenerated holes oxidize water to oxygen and protons (Figure 4.21).[72–74] However, on the silica surface, because of the insulating SiO_2 layer, there was no electronic communication between gold and the silicon surface, so gold was selectively deposited on the titania nanobowls. The gold nanoparticle-decorated titania nanobowls are shown in the SEM images of Figure 4.22. We also used Auger electron spectroscopy to confirm the deposition of metallic gold on the titania. As shown in Figure 4.23, four different sites were chosen for analysis: sites 1~3 were inside the pit regions while site 4 was on the flat surfaces outside of the pits. For sites 1~3, we observed strong Au MNN signals indicating the existence of gold inside the etched pits. For site 4, only an extremely weak signal was observed. Based on these results, we conclude that the gold deposition primarily occurred on titania nanobowls.

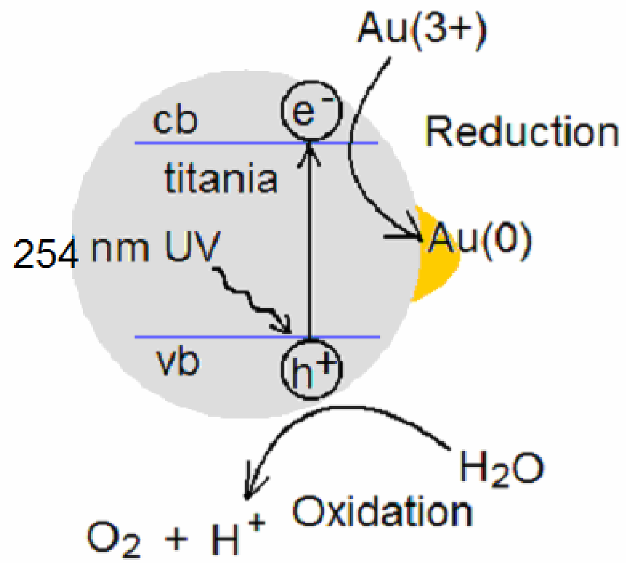

Figure 4.21. Mechanism of photodeposition of gold nanoparticles on titania surface under UV light.

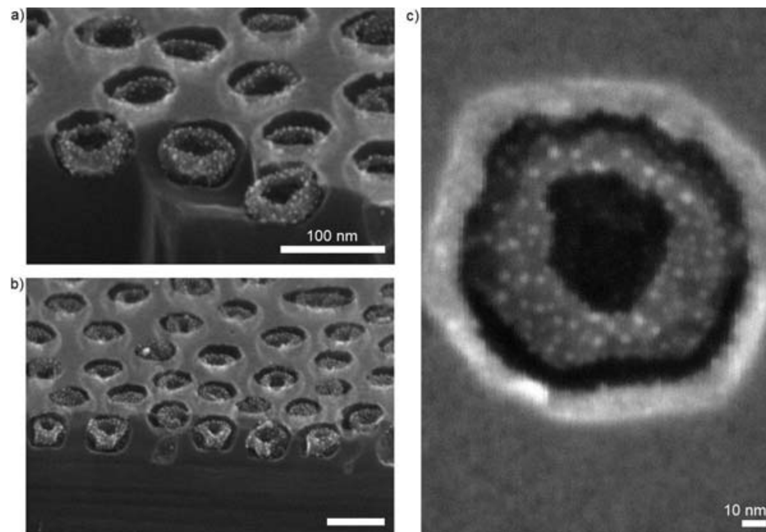

Figure 4.22. SEM images of gold nanoparticle-decorated titania nanobowls.

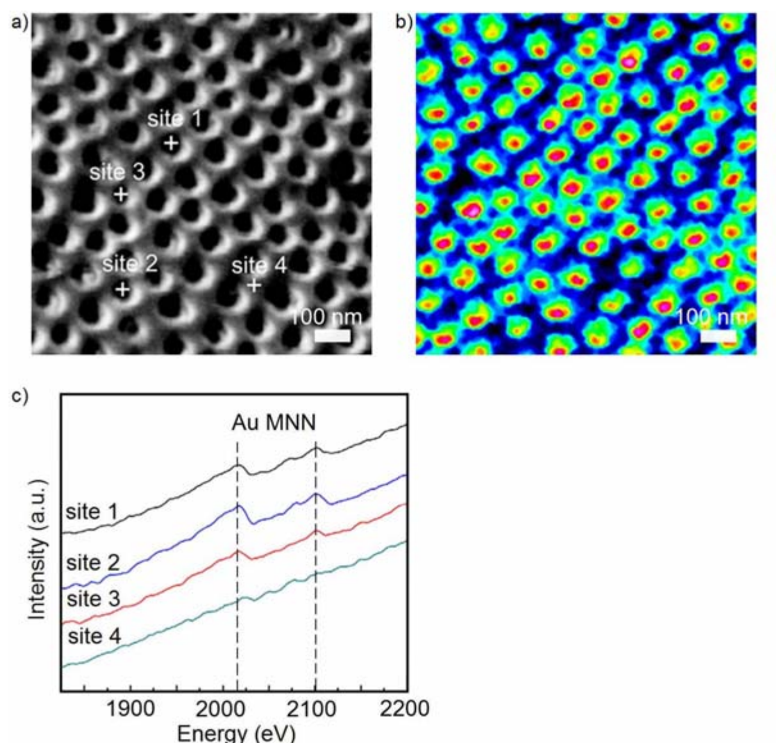

Figure 4.23. (a) SEM image of a titania/gold-coated silicon surface. (b) Ti LMM Auger signal mapping, and (c) gold Auger MNN signals of the four different sites chosen from (a). Reprinted with permission from ref. 4. Copyright © 2011 American Chemical Society.

4.3. Conclusion

This chapter demonstrated nanopatterning of titania nanobowls using an etched silicon substrate as a platform. Silicon surfaces that had been etched with HF (aq) using a PS-P4VP BCP mask comprised of pseudo-hexagonal arrays of etched pits that are Si-H_x terminated. The top flat face of the silicon substrate was protected by the PS matrix in the BCP thin films, thus remaining capped by the native oxide. By using a series of interfacial chemical reactions, including silanization of the unetched native oxide regions and oxidation of the Si-H_x

terminated pits region, titania nanobowls were produced on the surface by a simple hydrolysis of $TiCl_4$.

Combined with approaches to achieve different chemical functionalizations on the interfaces, the etched silicon substrates provided the means to tune both shape and location of the titania. When the hydrolysis of $TiCl_4$ was applied directly on the as-etched silicon substrates, titania only deposited on the native oxide covered regions; when the as-etched silicon substrates were fully oxidized, titania films covered the entire surface.

Further functionalization of titania with gold nanoparticles and release of the titania nanobowls have also been discussed in this chapter.

4.4. Experimental Methods

Generalities

Si(111) (p-type, B-doped, ρ = 1-10 $\Omega\cdot$cm, thickness = 600-650 cm) wafers were purchased from MEMC Electronic Material. PS-*b*-P4VP (109k-*b*-27k) was purchased from Polymer Source Inc. Hydrofluoric acid (HF) was purchased from J. T. Baker. Hydrogen tetrachloroaurate (III) trihydrate (Sigma Aldrich, 99.9%), titanium (IV) chloride (Alfa Aesar, 99.6%), octadecyltrichlorosilane (Sigma Aldrich, 90%), hydrogen peroxide (Fisher, 30%), sulfuric acid (J. T. Baker, 96.1%), ammonium hydroxide (J. T. Baker, 30%), hydrochloric acid (J. T. Baker, 36.5%), ethanol (Fisher, 99.8%), acetone (Fisher, 99.6%), hexane (Fisher, 99.8%) and toluene (Sigma Aldrich, 99.8%) were used in the preparations. Alkenes or alkynes (Aldrich) used for hydrosilylation were

purified by distillation and stored in a refrigerator in an argon filled glove box. All other chemicals and solvents were used as received without further purification. High purity Millipore water (18 MΩ•cm, Barnstead Nanopure water) was used throughout all the experiments.

Characterization

Titania and gold structures on silicon surfaces obtained in this study were characterized by SEM, and Auger Electron Spectroscopy (AES). The SEM images were taken with a Hitachi S-4800 FE-SEM in the National Institute for Nanotechnology (NINT) using an electron energy of 15 keV under high vacuum conditions ($<10^{-8}$ Torr). Auger Electron Spectroscopy (AES) was performed with a JAMP-9500F Field Emission Scanning Auger Microprobe (JEOL Ltd.).

Silicon Cleaning Procedures

1 cm by 1 cm pieces of Si (111) were first degreased in an ultrasonic bath of a common dish soap solution, rinsed in Millipore water, and then dried with a stream of nitrogen gas. Both standard piranha and RCA cleaning procedures were used for the wafer cleaning: Piranha cleaning was performed with a hot (80 ^{o}C) piranha solution (H_2SO_4: H_2O_2= 3:1, v/v). The silicon pieces were immersed in the hot piranha solution for 30 min. After removal from the solution the pieces were rinsed with excess water and dried in a nitrogen stream. In the RCA cleaning, the silicon pieces were immersed in a standard RCA I solution of NH_4OH, H_2O_2 and Millipore water in a ratio of 1:1:5 at 80 ^{o}C for 20 min. The

pieces were then rinsed with excess water and immersed in another standard RCA II solution of HCl, H_2O_2 and Millipore water in a ratio of 1:1:6 at 80 ^oC for 20 min. The pieces were then rinsed with water and dried in a nitrogen gas flow.

Polymer Template Preparation

PS-*b*-P4VP BCPs were weighed and dissolved in toluene at 80 ^oC by stirring overnight to make a ~1% w/w solution of polymer, then the solutions were cooled down to room temperature. 12 μL of the PS-*b*-P4VP solution was then dropped onto the cleaned Si(111) wafer and spin cast at 4200 rpm for 60 s under argon environment to fabricate BCP thin films on the substrate (spin coater model WS-400B-6NPP-Lite, Laurell Technologies, North Wales, PA).

Etch Pit Fabrication

To fabricate the etched pit arrays, PS-*b*-P4VP coated Si(111) wafers were immersed in a 0.02% HF(aq) solution for 40 minutes and then removed, rinsed with excess water, and dried with a stream of nitrogen gas. The polymer residue was then removed with toluene.

Deposition of Gold Nanoparticles inside Etched Pits

Galvanic displacement was used to achieve the selective deposition of gold nanoparticles on etched silicon. In this thesis work, to deposit gold nanoparticles exclusively into the interior of the pits, the residual PS-*b*-P4VP BCP on as-prepared etched silicon substrate was first removed with toluene, and the silicon

substrate was immersed into a gold growth solution directly (10^{-4} M $HAuCl_4$ ethanolic solution, V_{water}: $V_{ethanol}$=1:1) for 5 min. The silicon substrate was then removed from the gold growth solution and rinsed thoroughly with excess ethanol and water.

Silanization and Oxidation of the Silicon Surface

Freshly etched silicon substrates were placed in 20 mL of self-assembly solution, which contained 1.3 mM octadecyltrichlorosilane (CH_3-$(CH_2)_{17}SiCl_3$, OTS) (≥90%, Aldrich) in dry hexanes for 30 minutes at room temperature. To remove the unreacted OTS from the surface, the silicon substrates were then removed from the solution, transferred into 20 mL of neat hexane, and cleaned by ultrasonication for 3 min. After repeating the cleaning procedure three times, the silicon wafers were then rinsed with dry hexanes and dried with nitrogen gas. This silanization reaction was carried out in glass containers. To oxidize the interior of the etched pits, the samples were immersed in a 30% (w/w) hydrogen peroxide solution at room temperature for 12 h after the silanization reaction. The samples were then taken out from the oxidation solution and rinsed with excess water and transferred into a three-neck flask without further drying.

Deposition of Titania on Silicon Surfaces

To deposit titania exclusively inside the interior of the etched pits, the oxidized samples were rinsed with water and then transferred into a water bath heated (80 ^{o}C) three-neck flask in which a rough vacuum was applied for 30

seconds. $TiCl_4$ vapor was then introduced into the flask from a liquid $TiCl_4$ source at room temperature for 300 seconds. After the TiO_2 deposition, the samples were removed from the flask, rinsed with water and dried in a stream of nitrogen gas. In the control experiment, the etched silicon substrates were oxidized by hydrogen peroxide solution at room temperature for 12 h, and transferred into the reaction container for titania deposition. The titania nanobowl samples were thermally annealed at 550 ^oC in air for 3 h.

Release of Titania Nanobowls on Silicon Surfaces

HF etching was used to further release the titania nanobowls from the silicon surface. The titania nanobowl samples were immersed in a dilute HF solution (0.02%) for 6 h and then gently rinsed with water and dried in a stream of nitrogen gas.

Gold Deposition on Titania Nanobowls

To deposit gold nanoparticles exclusively on titania nanobowls, a gold solution prepared by neutralizing a 10^{-5} M $HAuCl_4$ solution to a pH of 7 using KOH(aq) was used as the growth solution. The titania nanobowl loaded silicon substrates were then immersed into the growth solution for 5 min under UV irradiation with a 5 W screen inspection UV lamp filtered to pass a narrow band around 254 nm.

4.5. References

(1) Park, M.; Harrison, C.; Chaikin, P. M.; Register, R. A.; Adamson, D. H. *Science* **1997**, *276*, 1401-1404.

(2) Milliron, D. J.; Caldwell, M. A.; Wong, H.-S. P. *Nano Lett.* **2007**, *7*, 3504-3507.

(3) Park, S.; Wang, J.-Y.; Kim, B.; Russell, T. P. *Nano Lett.* **2008**, *8*, 1667-1672.

(4) Zhang, X.; Qiao, Y.; Xu, L.; Buriak, J. M. *ACS Nano* **2011**, *5*, 5015-5024.

(5) Chen, X.; Mao, S. S. *Chem. Rev.* **2007**, *107*, 2891-2959.

(6) Li, H.; Li, J.; Yang, Z.; Xu, Q.; Hu, X. *Anal. Chem.* **2011**, *83*, 5290-5295.

(7) Hou, W.; Wang, Q. *Langmuir* **2009**, *25*, 6875-6879.

(8) Ortiz, G. F.; Hanzu, I.; Djenizian, T.; Lavela, P.; Tirado, J. L.; Knauth, P. *Chem. Mater.* **2009**, *21*, 63-67.

(9) Lee, S.-H. A.; Abrams, N. M.; Hoertz, P. G.; Barber, G. D.; Halaoui, L. I.; Mallouk, T. E. *J. Phys. Chem. B* **2008**, *112*, 14415-14421.

(10) Ma, T.; Akiyama, M.; Abe, E.; Imai, I. *Nano Lett.* **2005**, *5*, 2543-2547.

(11) Zheng, Q.; Kang, H.; Yun, J.; Lee, J.; Park, J. H.; Baik, S. *ACS Nano* **2011**, *5*, 5088-5093.

(12) Wijnhoven, J. E. G. J.; Bechger, L.; Vos, W. L. *Chem. Mater.* **2001**, *13*, 4486-4499.

(13) Chen, J. I. L.; von Freymann, G.; Kitaev, V.; Ozin, G. A. *J. Am. Chem. Soc.* **2007**, *129*, 1196-1202.

(14) Black, C. T. *ACS Nano* **2007**, *1*, 147-150.

(15) Zabetakis, D.; Dressick, W. J. *ACS Appl. Mater. Interfaces* **2009**, *1*, 4-25.

(16) Simeone, F. C.; Albonetti, C.; Cavallini, M. *J. Phys. Chem. C* **2009**, *113*, 18987-18994.

(17) Carter, K. R. *ACS Nano* **2010**, *4*, 595-598.

(18) Gao, Y.; Koumoto, K. *Cryst. Growth Des.* **2005**, *5*, 1983-2017.

(19) Chabinyc, M. L.; Salleo, A. *Chem. Mater.* **2004**, *16*, 4509-4521.

(20) Hayward, R. C.; Pochan, D. J. *Macromolecules* **2010**, *43*, 3577-3584.

(21) Giacomelli, C.; Schmidt, V.; Aissou, K.; Borsali, R. *Langmuir* **2010**, *26*, 15734-15744.

(22) Hamley, I. W. *Nanotechnology* **2003**, *14*, R39-R54.

(23) Guarini, K. W.; Black, C. T.; Milkove, K. R.; Sandstrom, R. L. *J. Vac. Sci. Technol. B* **2001**, *19*, 2784-2788.

(24) Wang, C.-W.; Moffitt, M. G. *Chem. Mater.* **2005**, *17*, 3871-3878.

(25) Leclère, P.; Parente, V.; Brédas, J. L.; François, B.; Lazzaroni, R. *Chem. of Mater.* **1998**, *10*, 4010-4014.

(26) Soler-Illia, G. J. de A. A.; Crepaldi, E. L.; Grosso, D.; Sanchez, C. *Curr. Opin. Coll. Interf. Sci.* **2003**, *8*, 109-126.

(27) Chen, D.; Huang, F.; Cheng, Y.; Caruso, R. A. *Adv. Mater.* **2009**, *21*, 2206-2210.

(28) Feng, X.; Shankar, K.; Varghese, O. K.; Paulose, M.; Latempa, T. J.; Grimes, C. A. *Nano Lett.* **2008**, *8*, 3781-3786.

(29) Chinthamanipeta, P. S.; Lou, Q.; Shipp, D. A. *ACS Nano* **2011**, *5*, 450-456.

(30) Alberius, P. C. A.; Frindell, K. L.; Hayward, R. C.; Kramer, E. J.; Stucky, G. D.; Chmelka, B. F. *Chem. Mater.* **2002**, *14*, 3284-3294.

(31) Smarsly, B.; Grosso, D.; Brezesinski, T.; Pinna, N.; Boissière, C.; Antonietti, M.; Sanchez, C. *Chem. Mater.* **2004**, *16*, 2948-2952.

(32) Park, S.-Y.; Sul, W.-H. *Polymer* **2008**, *49*, 3327-3334.

(33) Spatz, J. P.; Mössmer, S.; Hartmann, C.; Möller, M.; Herzog, T.; Krieger, M.; Boyen, H.-G.; Ziemann, P.; Kabius, B. *Langmuir* **2000**, *16*, 407-415.

(34) Glass, R.; M ller, M.; Spatz, J. P. *Nanotechnology* **2003**, *14*, 1153-1160.

(35) Glass, R.; Arnold, M.; Blümmel, J.; Küller, A.; Möller, M.; Spatz, J. P. *Adv. Funct. Mater.* **2003**, *13*, 569-575.

(36) Ranzinger, J.; Krippner-Heidenreich, A.; Haraszti, T.; Bock, E.; Tepperink, J.; Spatz, J. P.; Scheurich, P. *Nano Lett.* **2009**, *9*, 4240-4245.

(37) Qiao, Y.; Wang, D.; Buriak, J. M. *Nano Lett.* **2007**, *7*, 464-469.

(38) Kim, H.-C.; Park, S.-M.; Hinsberg, W. D. *Chem. Rev.* **2010**, *110*, 146-177.

(39) Simon, P. F. W.; Ulrich, R.; Spiess, H. W.; Wiesner, U. *Chem. Mater.* **2001**, *13*, 3464-3486.

(40) Jung, Y. S.; Ross, C. A. *Nano Lett.* **2007**, *7*, 2046-2050.

(41) Black, C. T. *Appl. Phys. Lett.* **2005**, *87*, 163116.

(42) Davis, R. J.; Liu, Z. *Chem. Mater.* **1997**, *9*, 2311-2324.

(43) Nijhuis, T. A.; Makkee, M.; Moulijn, J. A.; Weckhuysen, B. M. *Ind. Eng. Chem. Res.* **2006**, *45*, 3447-3459.

(44) Shankar, K.; Basham, J. I.; Allam, N. K.; Varghese, O. K.; Mor, G. K.; Feng, X.; Paulose, M.; Seabold, J. A.; Choi, K.-S.; Grimes, C. A. *J. Phys. Chem. C* **2009**, *113*, 6327-6359.

(45) Di Valentin, C.; Pacchioni, G.; Selloni, A. *J. Phys. Chem. C* **2009**, *113*, 20543-20552.

(46) Kanta, A.; Sedev, R.; Ralston, J. *Langmuir* **2005**, *21*, 5790-5794.

(47) Michel, R.; Reviakine, I.; Sutherland, D.; Fokas, C.; Csucs, G.; Danuser, G.; Spencer, N. D.; Textor, M. *Langmuir* **2002**, *18*, 8580-8586.

(48) Michel, R.; Lussi, J. W.; Csucs, G.; Reviakine, I.; Danuser, G.; Ketterer, B.; Hubbell, J. A.; Textor, M.; Spencer, N. D. *Langmuir* **2002**, *18*, 3281-3287.

(49) Lussi, J. W.; Michel, R.; Reviakine, I.; Falconnet, D.; Goessl, A.; Csucs, G.; Hubbell, J. A.; Textor, M. *Prog. Surf. Sci.* **2004**, *76*, 55-69.

(50) Chinthamanipeta, P. S.; Lou, Q.; Shipp, D. A. *ACS Nano ASAP Article*.

(51) Matsushita, S. I.; Miwa, T.; Tryk, D. A.; Fujishima, A. *Langmuir* **1998**, *14*, 6441-6447.

(52) Chen, Y.; Park, S.-M.; Kim, H.-C.; McVittie, J. P.; Ting, C.; Nish, Y. *J. Electrochem. Soc.* **2010**, *157*, E155-E161.

(53) Park, O.-H.; Cheng, J. Y.; Hart, M.; Topuria, T.; Rice, P. M.; Krupp, L. E.; Miller, R. D.; Ito, H.; Kim, H.-C. *Adv. Mater.* **2008**, *20*, 738-742.

(54) Crossland, E. J. W.; Nedelcu, M.; Ducati, C.; Ludwigs, S.; Hillmyer, M. A.; Steiner, U.; Snaith, H. J. *Nano Lett.* **2009**, *9*, 2813-2819.

(55) Wang, X. D.; Graugnard, E.; King, J. S.; Wang, Z. L.; Summers, C. J. *Nano Letters* **2004**, *4*, 2223-2226.

(56) Peters, R. D.; Nealey, P. F.; Crain, J. N.; Himpsel, F. J. *Langmuir* **2002**, *18*, 1250-1256.

(57) Wang, R.; Parikh, A. N.; Beers, J. D.; Shreve, A. P.; Swanson, B. *J. Phys. Chem. B* **1999**, *103*, 10149-10157.

(58) Li, D.; Moore, L. W.; Swanson, B. I. *Langmuir* **1994**, *10*, 1177-1185.

(59) Howland, M. C.; Sapuri-Butti, A. R.; Dixit, S. S.; Dattelbaum, A. M.; Shreve, A. P.; Parikh, A. N. *J. Am. Chem. Soc.* **2005**, *127*, 6752-6765.

(60) Morita, M.; Ohmi, T.; Hasegawa, E.; Teramoto, A. *Jpn. J. Appl. Phys.* **1990**, *29*, L2392-L2394.

(61) Moreno, J. D.; Guerrero-Lemus, R.; M.Martínez-Duart, J.; Marcos, M. L.; González-Velasco, J. *Adv. Mater.* **1998**, *10*, 38-42.

(62) Barrelet, C. J.; Robinson, D. B.; Cheng, J.; Hunt, T. P.; Quate, C. F.; Chidsey, C. E. D. *Langmuir* **2001**, *17*, 3460-3465.

(63) Cheng, J.; Robinson, D. B.; Cicero, R. L.; Eberspacher, T.; Barrelet, C. J.; Chidsey, C. E. D. *J. Phys. Chem. B* **2001**, *105*, 10900-10904.

(64) Gu, W.; Tripp, C. P. *Langmuir* **2005**, *21*, 211-216.

(65) Schrijnemakers, K.; Impens, N. R. E. N.; Vansant, E. F. *Langmuir* **1999**, *15*, 5807-5813.

(66) Wang, T.-H.; Navarrete-López, A. M.; Li, S.; Dixon, D. A.; Gole, J. L. *The Journal of Physical Chemistry A* **2010**, *114*, 7561-7570.

(67) Haukka, S.; Lakomaa, E.-L.; Suntola, T. *Thin Solid Films* **1993**, *225*, 280-283.

(68) Zhang, M.; Gao, G.; Zhao, D.; Li, Z.; Liu, F. *J. Phys. Chem. B* **2005**, *109*, 9411-9415.

(69) Yin, Y.; Lu, Y.; Gates, B.; Xia, Y. *Chem. Mater.* **2001**, *13*, 1146-1148.

(70) Ohno, T.; Sarukawa, K.; Matsumura, M. *J. Phys. Chem. B* **2001**, *105*, 2417-2420.

(71) Simon, P. F. W.; Ulrich, R.; Spiess, H. W.; Wiesner, U. *Chem. Mater.* **2001**, *13*, 3464-3486.

(72) Chan, S. C.; Barteau, M. A. *Langmuir* **2005**, *21*, 5588-5595.

(73) Hidalgo, M. C.; Maicu, M.; Navío, J. A.; Colón, G. *J. Phys. Chem. C* **2009**, *113*, 12840-12847.

(74) Kydd, R.; Scott, J.; Teoh, W. Y.; Chiang, K.; Amal, R. *Langmuir* **2010**, *26*, 2099-2106.

Chapter 5
Conclusion and Outlook

In this thesis, which discussed rapid BCP self-assembly by microwave irradiation, the precise control of spacing by the use of BCP blends, and the synthesis of titania nanobowls by using BCP as the patterning template, is concluded in this chapter with a summary of the highlights of the preceding chapters, followed by discussion of some potential research directions that stem from this work.

5.1 Chapter Summaries

Chapter 1

Chapter 1 discussed the background of this thesis work, beginning with four current lithography techniques that are commonly used in the semiconductor industry to fabricate nano- or micro- features: photolithography, electron beam lithography, nanoimprint lithography, and SA imprint lithography, as well as surveying some of their advantages and challenges. As a strong driving force for the digital age, less costly strategies with the ability to pattern even smaller objects may be needed to meet manufacturing standards. In the ITRS roadmap, BCPs are mentioned as innovative emerging materials that are versatile and cost-effective building blocks for bottom-up approaches capable of nanometer-scale patterning. Self-assembling BCPs have attracted a great deal of attention in the past decade. BCP lithography is now moving beyond research and into integration with some early-stage production. However, several major challenges

still remain, such as high level patterning perfection/registration and high patterning speed. Typical examples of reducing pattern defects, integrating BCP self-assembly into conventional lithographic process, and nanostructure templating are shown in this chapter.

Chapter 2

In Chapter 2, a new microwave-based annealing technique combining the two conventional annealing techniques, thermal annealing and solvent annealing, was presented as a means to decrease the pattern ordering time. In order to construct parallel linear features, thin films containing BCP micelles were first coated on doped silicon substrates, and then the samples were sealed inside a microwave reaction tube with a small amount of solvent. After microwave heating, the BCPs self-assembled to form dense arrays of nanowires. The time required for such organizations can be reduced from hours or even days for conventional annealing to minutes for this microwave annealing process. In addition, we demonstrated the compatibility of the microwave annealing technique with directed self-assembly by graphoepitaxy, in which well-aligned BCP nanostructures with long-range order were formed after 180-second microwave annealing on BCP spin-coated surfaces prepatterned by EBL with silica features,.

Chapter 3

In Chapter 3, a $100 household microwave oven was employed as the heating source to perform the fast self-assembly of BCPs. With the help of a custom-

made Teflon container, multiple samples could be run at the same time. The procedure was very similar to the one described in Chapter 2 except it did not include the pre-heating and cooling steps which were required in the scientific microwave system. Highly ordered structures of self-assembled BCPs were obtained in 60 seconds. We also demonstrated the use of PS-PVP binary blends to control linear feature spacing and to fabricate hybrid nanostructures. When BCPs are mixed with another polymer, loss of control over the phase-separation is commonly encountered as the amount of the other component is increased. We found, surprisingly, that when one PS-P2VP was blended with the other PS-P2VP, the mixture offered precise control over spacing without losing the structure in the phase-separation. By changing the ratio of the two components in the PS-P2VP/PS-P2VP blends, linear feature spacings ranging from 24.8 nm to 42.6 nm were achieved. To show the high level of control over spacing, we obtained 12 to 19 lines between a 500 nm wide topographic wall-like silica feature on silicon surfaces using two homologous BCP and four BCP blends. In addition, we demonstrated that when PS-P2VP/PS-P4VP binary blends were used, hybrid dot and line nanostructures could be achieved on the substrate surface. Although this study is still in an early stage, we hope the self-assembled PS-P2VP/PS-P4VP thin films could be used as templates to build hybrid metallic nanostructures (e.g. two different kinds of metals).

Chapter 4

To demonstrate the ability of templating nanostructures of BCP thin films, Chapter 3 dealt with nanopatterning of titania. PS-P4VP thin films were used as etching masks to fabricate ordered etched pit arrays on silicon surfaces.[1] We took a step towards utilizing these etched silicon substrates by fabricating titania nanobowls. The etched silicon surface was comprised of pseudo-hexagonal arrays of pits, whose interiors are terminated by Si-H_x functionalities. The top unetched face of the silicon substrate remained capped by the native oxide. Using a series of interfacial chemical reactions, including silanization of the native oxide covered regions, and oxidation of the Si-H_x terminated interface, titania nanobowls with an average diameter of ~55 nm were produced on the surface by a simple hydrolysis of $TiCl_4$. We also demonstrated further functionalization of gold nanoparticles on titania nanobowls and the release of these nanobowls by HF etching. SEM imaging, AES mapping, and XRD analysis were used to characterize the titania nanobowls.

5.2. Proposed Research Directions

Solvothermal Annealing of BCPs

From a fundamental point of view, the microwave heating mechanism in microwave annealing needs to be addressed. Chapters 2 and 3 discussed solvent-assisted microwave annealing in a Biotage microwave system and a conventional 9.35 GHz household microwave oven, respectively. In the Biotage microwave system, highly doped silicon substrates seemed to be good microwave absorbers

since more ordered self-assembled patterns were observed on substrates with high conductivities for this specific system. This thesis work also showed in a wax melting test that doped silicon substrates with relatively high conductivities could be heated faster in a conventional microwave oven (see Chapter 3). In the microwave absorption by silicon, it has been reported by Zohm *et al.* that silicon with low doping levels can be heated faster than highly doped silicon with a 28 GHz microwave source.[2] In the case of 9.35 GHz microwave sources, Sameshima *et al.* reported that highly doped silicon absorbed more microwaves than less doped silicon.[3] While the fast self-assembly of BCPs was shown in this thesis by using solvent-assisted microwave annealing, further studies need to be carried out in order to explain the microwave absorbing mechanism of silicon. If the fast annealing of BCPs can be carried out as a solvent-assisted heating without using microwaves, the process could be simplified. Such a solvothermal annealing process could be achieved by building fast heating equipments inside a solvent annealing chamber, thus the sample could be heated with the solvent simultaneously (Figure 5.1). Good control over the sample temperature and solvent vapor pressure should lead to long-range order self-assembly of BCPs within minutes. The BCP solvothermal annealing process could also increase the probability of BCP self-assembly being utilized in real-world applications, such as quick and mass production of ordered patterning.[4]

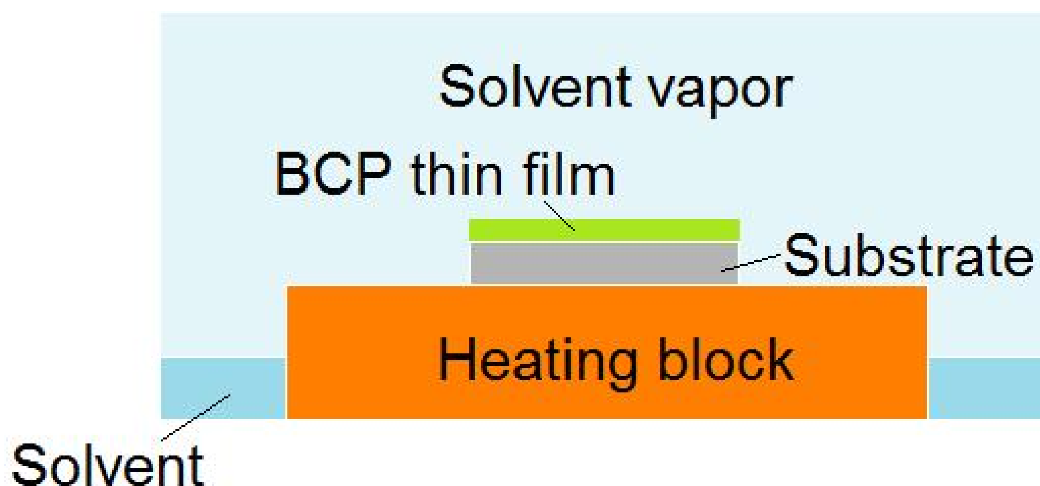

Figure 5.1. Solvothermal annealing of BCPs.

Localized BCP Self-Assembly in Microwaves

With respect to commercialization, one of the challenges of BCP self-assembly is to localize nanoscale patterning in very specific locations. As described in Chapter 1, long range ordering of BCP microdomains with desired orientations has been accomplished by directed self-assembly via chemical prepatterning and graphoepitaxy. For example, Nealey and coworkers demonstrated an approach using a chemically prepatterned surface to fabricate isolated BCP self-assembled structures which showed the possibility of using BCP self-assembly for broad application in advanced lithography, including device layouts.[5] As shown in Figure 5.2, sets of 10, 5, 3, 2, and 1 isolated PMMA segments were fabricated in the BCP film. This thesis work showed the potential of a microwave annealing technique to be used for mass production in terms of faster annealing and lower defect density. One possible application of this technique is localized BCP self-assembly using a combination of a microwave

absorber and a non-absorber. BCP self-assembly provides a simple way to produce ordered dense features on the surfaces, but it is also critical to make the self-assembly happen only in the desired regions, as required by the semiconductor industry.

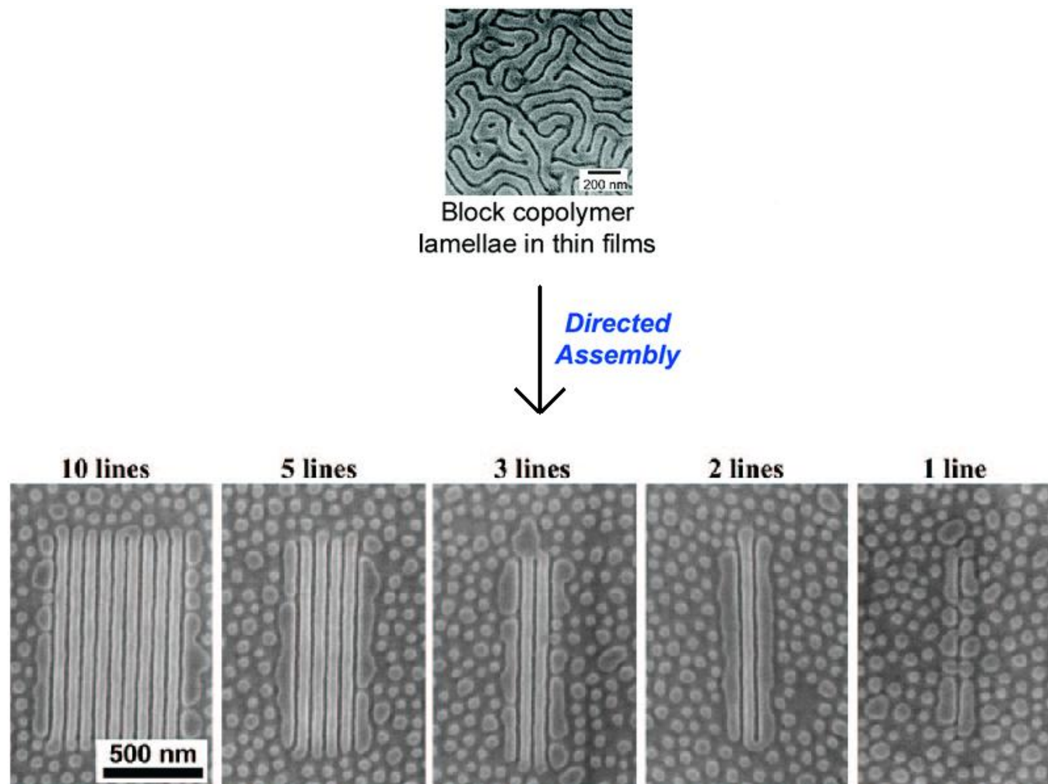

Figure 5.2. Isolated segment structures obtained by directed assembly of BCP. Reprinted with permission from ref. 5. Copyright © 2007 American Chemical Society.

To realize the control of BCP self-assembly on desired locations of a surface, one approach to be considered would be to combine a microwave absorber and a non-absorber in the annealing. Since the microwave annealing is a solvothermal process, as discussed in Chapters 2 and 3, the substrate resistivity is a key to the annealing. The concept of localized self-assembly is shown in Figure 5.3, in

which the substrate should be a poor microwave absorber but the prepatterned features on the surface should be good microwave absorbers in order to reduce the required temperature contrast during the microwave annealing.

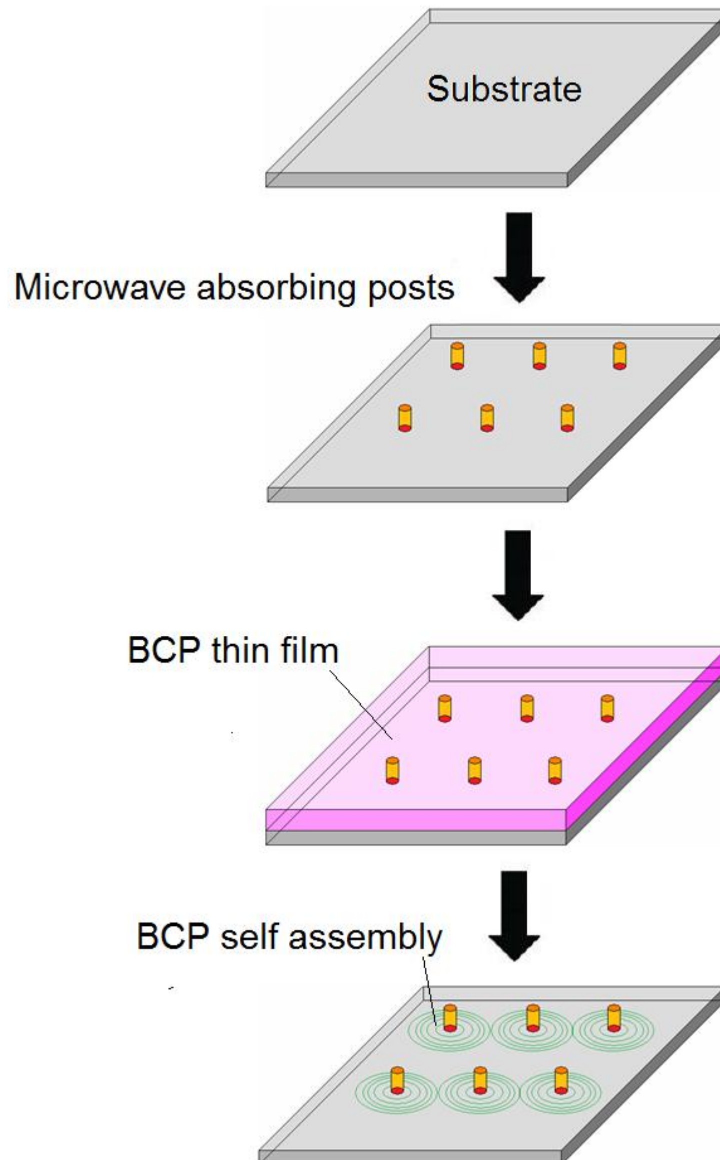

Figure 5.3. Proposed strategy of localized BCP self-assembly in microwaves.

To test the concept, we spin-coated PS-PMMA thin films on particle-covered silicon substrates and microwave-annealed the samples. All the samples were annealed under the same conditions for 120 seconds. After microwave annealing, the PS-PMMA samples were treated with a 20-second oxygen plasma to improve the visualization in SEM. As shown in Figure 5.4, better-organized structures were found around gold features but not found around silica nanoparticles. This suggested the possibility of using good microwave absorbing materials to get localized self-assembled structures, but the phenomenon we observed may just be because of the thickness gradient (Figure 5.5).[6]

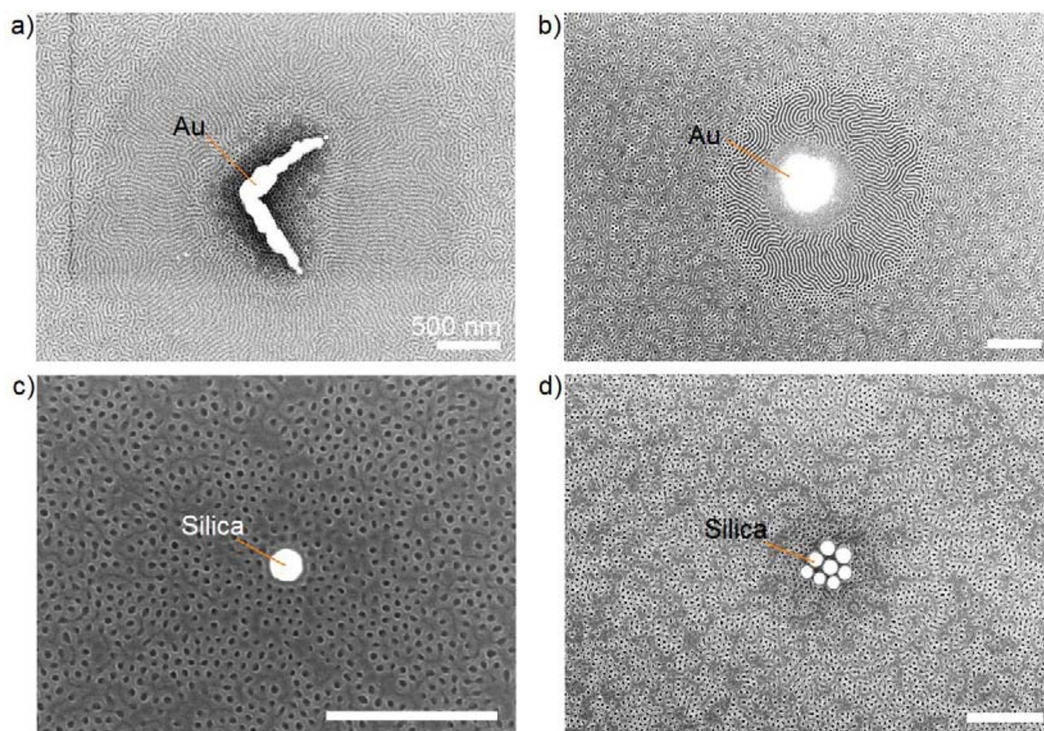

Figure 5.4. SEM images of localized BCP self-assembly in microwaves. (a) and (b) With Au nanostructures. (c) and (d) With silica nanoparticles.

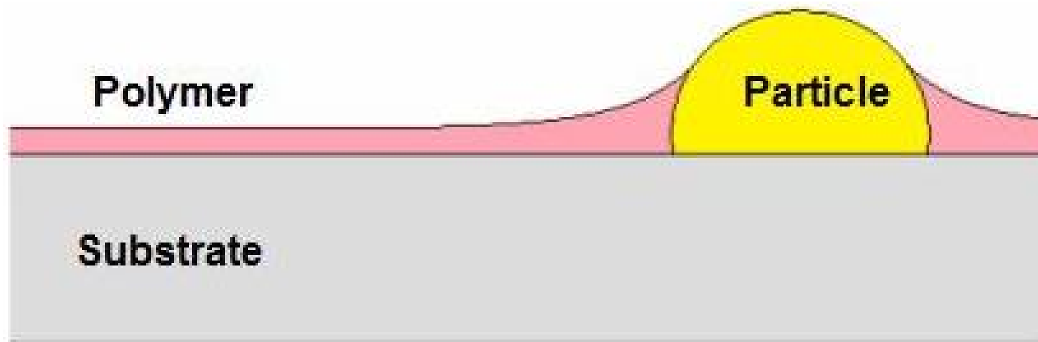

Figure 5.5. Schematic illustration of thickness gradient on a surface.

NIL with BCP Self-Assembly for Mass Production

NIL is fundamentally different from conventional lithography techniques and has attracted significant attention since its invention. As mentioned in Chapter 1, NIL, which prints features directly onto surfaces using a simple stamp process, is a cost-effective, high-throughput lithographic technology with high resolution down to 10 nm.[7] The molds of NIL are reusable and have graphoepitaxial features on them; thus NIL could offer a path toward high-throughput production of locally controlled fine pattering when combined with BCP self-assembly.[8–11]

Huck and coworkers showed that NIL can provide a driving force to order phase-separated PS-*b*-PMMA BCP films in lateral dimensions.[10] The general procedure is illustrated in Figure 5.6 (a). First, the native oxide-covered silicon surface was neutralized with PS/PMMA random copolymer. PS-*b*-PMMA polymer was then spin-coated onto the surface to a specific thickness, and the polymer film with guiding patterns on the top was annealed. Finally, by selectively removing PMMA blocks through UV exposure and acetic acid washing, fine patterns were obtained on the surface. The SEM images in Figure

5.6 (b) show an example of well-aligned PS structures after imprint annealing and removal of the PMMA block. As a comparison, Figure 5.6 (c) shows an SEM image of PS structures left over on a free-space surface.

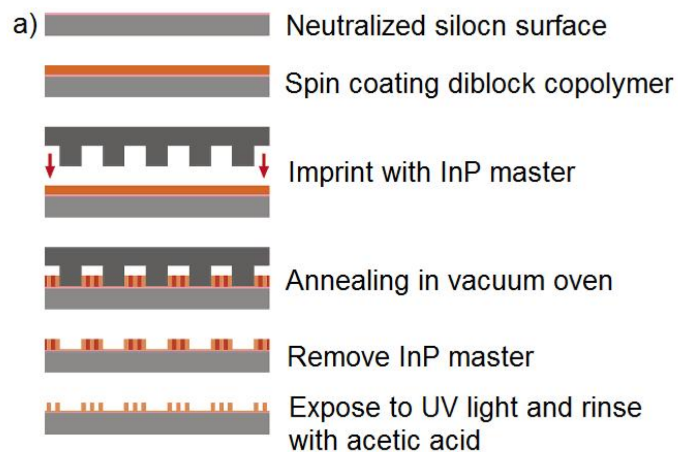

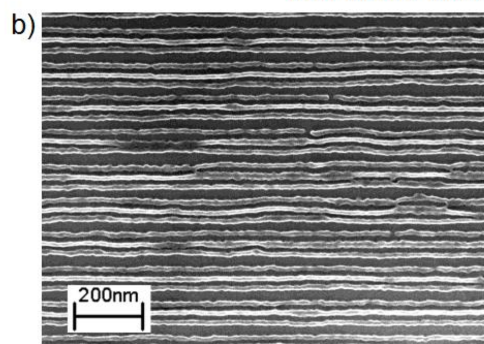

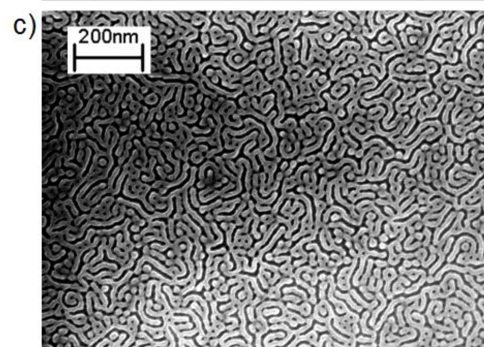

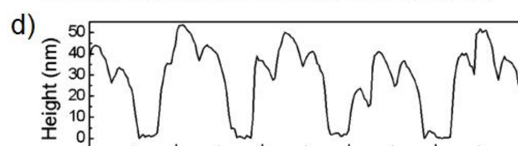

Figure 5.6. (a) Schematic presentation of procedures for controlled self-assembly of BCPs using NIL. (b) SEM image of lines structures obtained from controlled self-assembly of PS-*b*-PMMA. (c) SEM image of PS domain structures on free-space surface. (d) AFM cross-section profile of an imprint-annealing sample. Reprinted with permission from ref. 10. Copyright © 2004 American Chemical Society.

There is a major technical challenge in NIL with BCPs. Since the BCPs are heated above their glass transition temperatures, the molds have difficulty releasing the polymer because of the high degree of adhesion at the mold/polymer interface after the thermal imprinting process. Helms and coworkers recently reported using fluoroalkyl-modified PS (FA-PS) or PDMS (FA-PDMS) to decrease the adhesion (Figure 5.7).[8] Low interfacial energy contacts were achieved by coating the mold with fluoroalkyl additives and blending the BCPs with FA-polymer. Mold release with relative ease was achieved as a result. By comparison, significant adhesion of the BCP to the mold was observed in the absence of the FA-homopolymer additives, as shown in Figure 5.7 (e). From a practical manufacturing viewpoint, a major limitation of this process is the long processing time. The BCP self-assembly is efficiently directed within the mold in one hour of the nanoimprint process.

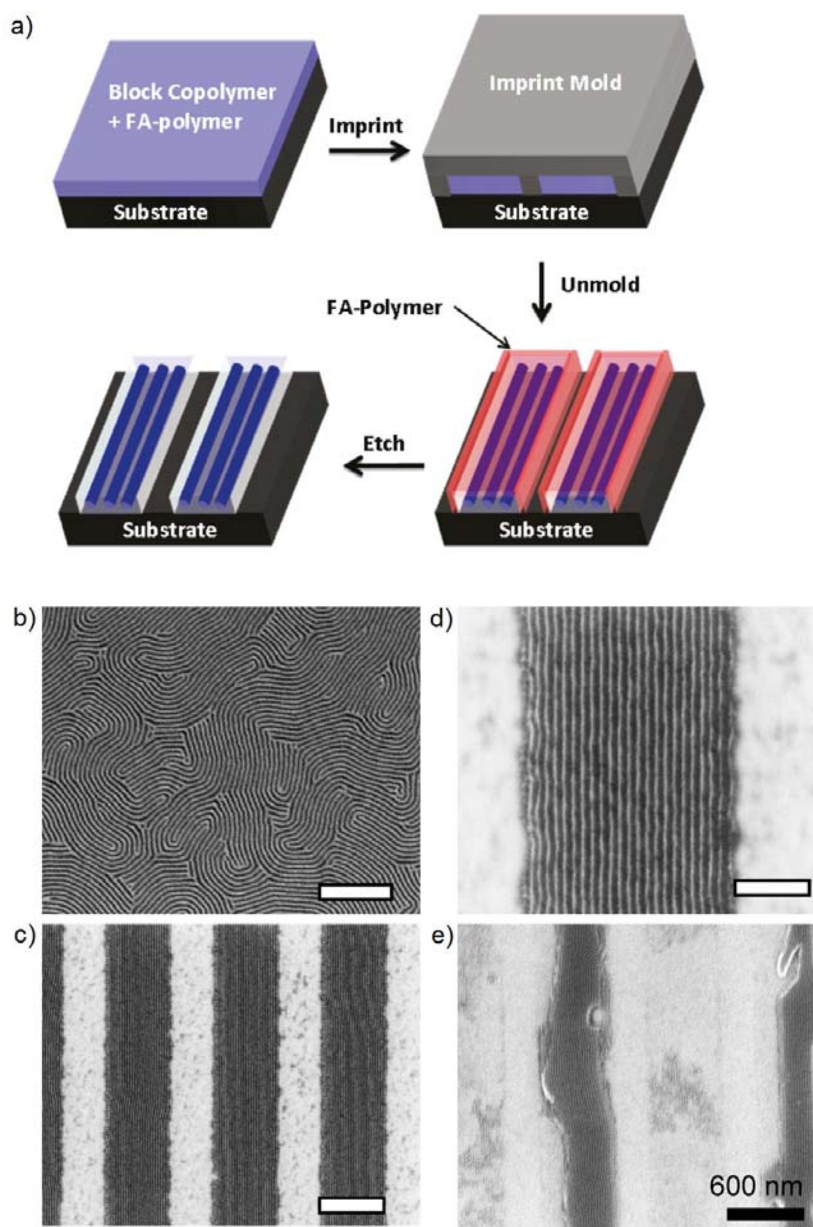

Figure 5.7. (a) Schematic presentation of BCP self-assembly using a thermal nanoimprint process. Fluoroalkyl (FA)-modified homopolymer was used to promote mold release. (b) SEM image of self-assembled PS-*b*-PDMS thin films on PS-coated silicon substrates in the presence of FA-PS (scale bar = 300 nm). (c) SEM image of directed self-assembled PS-*b*-PDMS in the presence of FA-PS (scale bar = 600 nm). (d) Magnified image of (c) (scale bar =200 nm). (e) SEM image of PS-*b*-PDMS nanostructures self-assembled in the absence of FA-PS additives during thermal

imprinting process. Significant adhesion of the BCP to the imprint mold was observed. Reprinted with permission from ref. 8. Copyright © 2011 American Chemical Society.

Since minimizing the processing time is desired in manufacturing, it is important to optimize the processing conditions for BCP self-assembly. However, very long annealing time may be required for NIL with BCPs in some cases. By combining NIL and BCP self-assembly, a highly regular dewetting process of a symmetric BCP (PS-*b*-PMMA) was reported.[11] The process is outlined in Figure 5.8. Silsesquioxane (SSQ) prepatterns, which provide chemical and physical properties at the same time, were used as substrates to control BCP film dewetting processes. The annealing time of PS-*b*-PMMA BCPs was 24 hours.

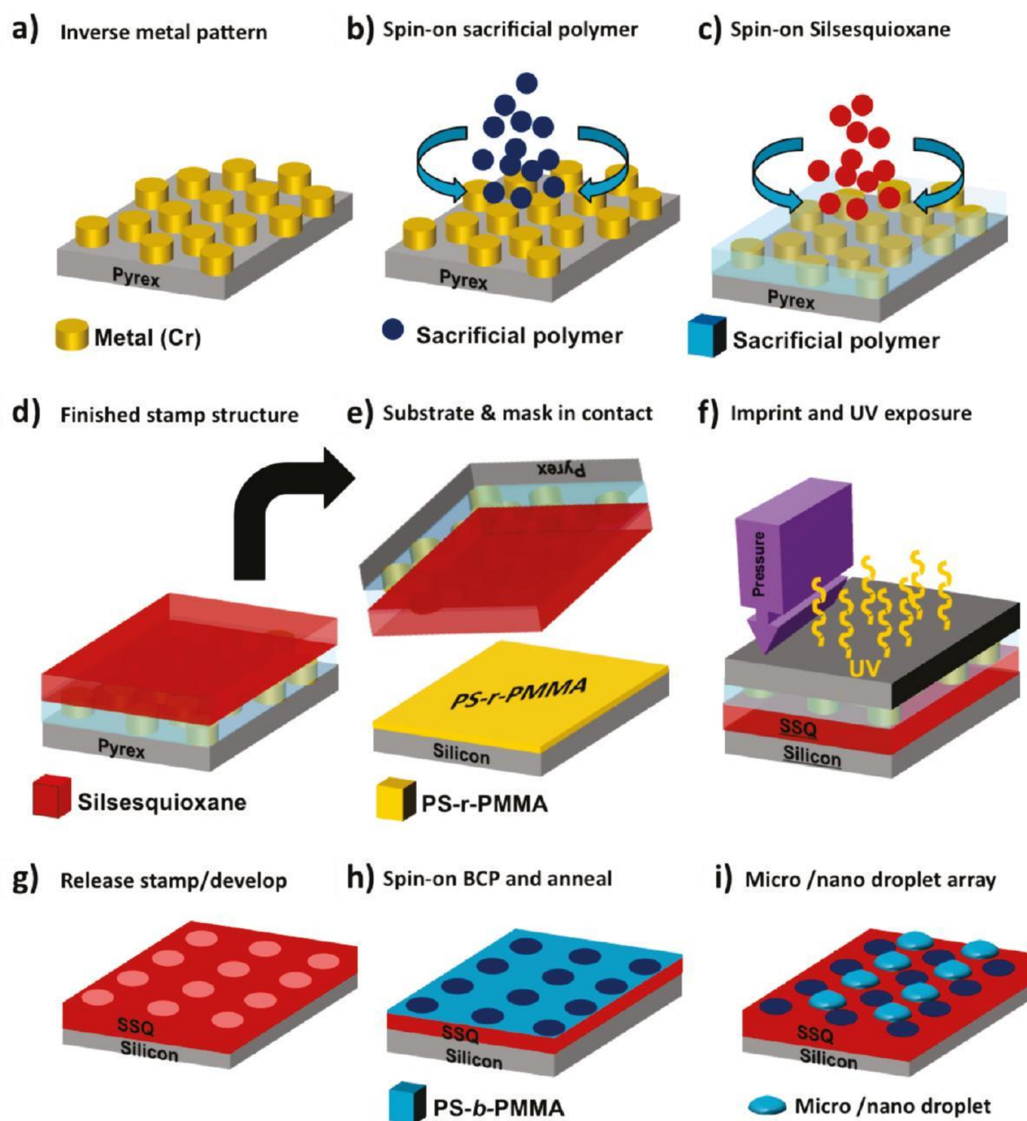

Figure 5.8. Schematic presentation of fabrication of patterned SSQ films using NIL technique. Reprinted with permission from ref. 11. Copyright © 2011 American Chemical Society.

The microwave-mediated approach demonstrated in Chapter 2 and 3 offers a convenient annealing of BCPs in minutes and may be combined with NIL to dramatically reduce the processing time. Since the microwave annealing is a solvothermal process, BCP thin films are soaked and soften in solvent vapor before the stamp/mold is applied; and it is reasonable to expect that the mold can be readily applied to the pre-soaked polymer films. Moreover, to achieve BCP self-assembly on microwave transparent substrates, a microwave transparent mold with imprint features that are excellent microwave absorbers could be used (Figure 5.9). The combination of microwave annealing and NIL may offer a convenient and flexible way to produce fine nanopatterns on large areas.

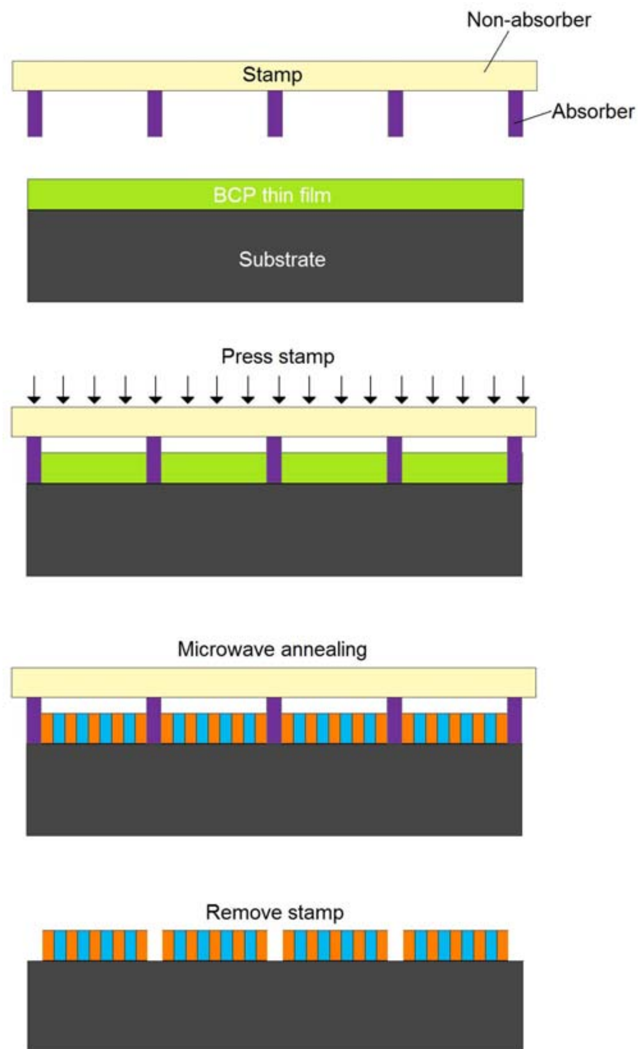

Figure 5.9. Fast microwave annealing of BCPs with NIL on microwave transparent substrate.

5.3. References

(1) Qiao, Y.; Wang, D.; Buriak, J. M. *Nano Lett.* **2007**, *7*, 464-469.

(2) Zohm, H.; Kasper, E.; Mehringer, P.; Müller, G. A. *Microelectron. Eng.* **2000**, *54*, 247-253.

(3) Sameshima, T.; Hayasaka, H.; Haba, T. *Jpn. J. Appl. Phys.* **2009**, *48*, 021204.

(4) *http://www-03.ibm.com/press/us/en/pressrelease/21473.wss*.

(5) Stoykovich, M. P.; Kang, H.; Daoulas, K. C.; Liu, G.; Liu, C.-C.; de Pablo, J. J.; Müller, M.; Nealey, P. F. *ACS Nano* **2007**, *1*, 168-175.

(6) Kim, B. H.; Lee, H. M.; Lee, J.; Son, S.; Jeong, S.; Lee, S.; Lee, D. I.; Kwak, S. U.; Jeong, H.; Shin, H.; Yoon, J.; Lavrentovich, O. D.; Kim, S. O. *Adv. Funct. Mater.* **2009**, *19*, 2584-2591.

(7) Chou, S. Y. *J. Vac. Sci. Technol. B* **1997**, *15*, 2897.

(8) Voet, V. S. D.; Pick, T. E.; Park, S.-M.; Moritz, M.; Hammack, A. T.; Urban, J. J.; Ogletree, D. F.; Olynick, D. L.; Helms, B. A. *J. Am. Chem. Soc.* **2011**, *133*, 2812-2815.

(9) Park, H. J.; Kang, M.-G.; Guo, L. J. *ACS Nano* **2009**, *3*, 2601-2608.

(10) Li, H.-W.; Huck, W. T. S. *Nano Lett.* **2004**, *4*, 1633-1636.

(11) Farrell, R. A.; Kehagias, N.; Shaw, M. T.; Reboud, V.; Zelsmann, M.; Holmes, J. D.; Sotomayor Torres, C. M.; Morris, M. A. *ACS Nano* **2011**, *5*, 1073-1085.